Di-Hadron Angular Correlation Dependence on Leading Hadron Identity in Relativistic Heavy Ion Collisions

BY

KOLJA KAUDER
B.S., Heinrich Heine Universität, Düsseldorf (Germany), 2007
M.S., University of Illinois at Chicago, 2009

THESIS

Submitted in partial fulfillment of the requirements
for the degree of Doctor of Philosophy in Physics
in the Graduate College of the
University of Illinois at Chicago, 2015

Chicago, Illinois

Defense Committee:

Olga Evdokimov, Chair and Advisor
David J. Hofman
Wai-Yee Keung
Zhenyu Ye
Jörn Putschke, Wayne State University

For my father, who provided answers a child could understand yet remain intrigued by when I asked so many years ago "What's inside an atom?"', "what's inside a proton?" I wish he could read this.

ACKNOWLEDGMENTS

I owe a great deal of gratitude to my advisor Olga Evdokimov for taking a chance on me when I had freshly arrived in Chicago, and for her patience, guidance, and mentorship. I also want to thank the members of my committees, David Hofman, Zhenyu Ye, Jörn Putschke, Wai-Yee Keung, Russel Betts, and Misha Stephanov, for their support and motivation. And I am extremely grateful for all the help and advice I received from my good friends and fellow grad students Cristina Suarez, Jeremy Callner, and Vasundhara Chetluru, when I joined the group. And finally, thanks to my parents Christel and Wolfgang and my wife Liz, who gave me the means and the strength to take up this path and follow through.

TABLE OF CONTENTS

CHAPTER **PAGE**

LIST OF TABLES

LIST OF FIGURES

FIGURE **PAGE**

FIGURE **PAGE**

FIGURE **PAGE**

LIST OF ABBREVIATIONS

DCA	Distance of Closest Approach
NFit	Number of Fit points
ZYAM	Zero Yield at Minimum
PID	Particle Identification
HEP	High Energy Physics
(s)QGP	(strongly interacting) Quark Gluon Plasma
QCD	Quantum ChromoDynamics
EOS	Equation Of State
RHIC	Relativistic Heavy Ion Collider
AGS	Alternating Gradient Synchrotron
SPS	Super Proton Synchrotron
LINAC	LINear ACcelerator
STAR	Solenoidal Tracker at RHIC
BRAHMS	Broad RAnge Hadron Magnetic Spectrometer
PHENIX	Pioneering High Energy Nuclear Interaction eXperiment

LIST OF ABBREVIATIONS (Continued)

TPC	Time Projection Chamber
ZDC	Zero Degree Calorimeter
CTB	Central Trigger Barrel
BEMC	Barrel ElectroMagnetic Calorimeter
EEMC	Endcap ElectroMagnetic Calorimeter
TOF	Time Of Flight
FTPC	Forward Time Projection Chamber
SVT	Silicon Vertex Tracker
MWPC	Multi-Wire Proportional Chambers
ADC	Analog-to-Digital Converter
GEANT	GEometry ANd Tracking

CHAPTER 1

INTRODUCTION

In relativistic heavy ion collisions, for a very brief moment a medium is created that has not been present outside of a laboratory since microseconds after the Big Bang. This hot, dense plasma displays the properties of a liquid with almost vanishing low viscosity, and allows the study of quantum chromodynamics (QCD) under extreme conditions, a many-body system of interacting quarks and gluons.

The most prominent observable associated with hydrodynamic behavior is elliptic flow v_2, the second Fourier harmonic of the azimuthal distribution of measured final-state hadrons. Its presence and magnitude, especially in off-center collisions, is attributed to the initial anisotropy being translated into a final-state momentum anisotropy by pressure gradients in a near-perfect liquid. It was found to scale with the number of valence quarks n_{q}, i.e. $v_2(\mathrm{baryon})/v_2(\mathrm{meson}) = 3/2$, indicative of how this anisotropy is acquired by partonic degrees of freedom that recombine into the final measured particles.

Another observation strongly hinting at recombination of partons is the measured baryon/meson ratio. In the intermediate energy range (transverse momentum p_T between about 2 and 5 GeV/c), this ratio is enhanced by up to a factor of three compared to systems without a QGP, found for example in proton-proton collisions.

While the bulk of this quark matter is not tractable with perturbative methods, strongly interacting high-energy parton pairs are created in hard collisions, at sufficiently high rates to be used as probes. The measurement of characteristic particle showers, jets, shows strong energy loss in this medium, consistent with QCD predictions of gluon bremsstrahlung.

Di-hadron correlations are a statistical method to differentially study this energy loss and to use jets as tomographical tools. Jets are identified by selecting high-energy hadrons, so-called triggers, as a proxy to the jet axis. The angular correlation of other particles in the event with respect to this trigger is than recorded and the data of many collisions combined.

A surprising discovery in such correlation measurements is a long-range structure close to the leading jet in azimuth (on the near-side), narrow in azimuth but flat over a broad polar angle. This structure, the ridge, is commonly ascribed to a flowing medium with initial conditions that are less homogeneous than previously often assumed.

In this work di-hadron correlations are separated by the particle identity of the leading hadron. This separation allows the study of all the phenomena above simultaneously.

The trigger hadron identity is expected to be linked to the identity of the original jet. The coupling strength of gluon radiation, expected to be the dominant energy loss mechanism in the medium, is more than a factor of two smaller for quarks than for gluons. This difference could potentially be detected as enhancement of particle yield close to, or back-to-back with, leading pions compared to non-pions.

On the other hand, the ratio of protons to pions in the trigger p_T range is enhanced by about 50% compared to proton-proton collisions, indicating under the recombination scenario that a relatively larger fraction of proton than pion triggers may come in fact from recombined partons and as such do not contribute jet-like yields. This relative yield decrease provides a new handle to test and quantify recombination.

Lastly, if the ridge is properly described by flow, then its flow harmonics too should display the characteristic n_{q} scaling behavior. This scaling is tested both qualitatively and quantitatively by the ridge dependence on the trigger identity. An alternative model will be considered as well.

In the next chapter, I will review the evidence for the creation and properties of the QGP in heavy ion collisions in more detail, focussing on the concepts mentioned above. The third chapter describes the experimental setup, and the fourth details the analysis method. In the final chapter, results and systematic uncertainties are presented and discussed.

CHAPTER 2

CREATION AND PROPERTIES OF QUARK GLUON PLASMA

Relativistic heavy ion collisions provide a glimpse beyond the confinement of the strong force into the world of asymptotically free, interacting quarks and gluons (partons). In the two decades since the start of a fixed target lead beam program at CERN's Super Proton Synchrotron (SPS), ample evidence has been collected that a new state of matter of collective partons governed by quantum chromodynamics (QCD) is indeed created in such collisions. But this matter is markedly different from expectations of a gas of weakly interacting partons, it rather displays the properties of an opaque liquid with almost vanishing viscosity, often called quark soup, or perfect liquid [26].

In the year 2000, weeks before the first gold-gold collisions at RHIC, the experiments at SPS announced for the first time strong evidence for such a new state of matter [27, 28]. Among the evidence is the first, almost casual mention of what would become one of the pillars in the case for a QGP: momentum anisotropy, which would soon be associated with hydrodynamic flow.

After four years of data analysis, the four RHIC experiments collaborated to each compose a community whitepaper to summarize all their findings and carefully assess the evidence gathered [29, 30, 31, 32].

Three lines of evidence stand out, two of which were suggested to be necessary and sufficient for the discovery of a strongly interacting QGP [33]:

- At low transverse momentum ($p_T \lesssim 2$ GeV/c), momentum anisotropies in the measured hadrons, quantified by the *elliptic flow* observable v_2 and acquired very early in the collision, point to the collective behavior of a perfect liquid.
- At intermediate transverse momentum ($2 \lesssim p_T \lesssim 5$ GeV/c), this elliptic flow is best described when re-parameterized in terms of the number of valence quarks in the measured hadrons, with a clear split into baryons and mesons and universal behavior when considered per quark. Additionally, the ratio of baryons to mesons measured for many different hadrons displays strong enhancement compared to vacuum fragmentation in proton-proton (pp) collisions. Both features can be understood as stemming from *recombination of quarks*, acquiring flow properties at a partonic level.
- At high transverse momentum ($p_T \geq$3-4 GeV/c), partons created in hard collisions experience massive energy loss, the *jet-quenching* effect, attributed to gluon radiation of a colored probe traversing a dense QCD medium.

In [33], the measurements at low and high p_T are combined with a third requirement, control experiments to separate properties of a true QGP from those of cold nuclear matter, to form a positive proof in the form of a symbolic equation:

$$\text{QGP} = P_{\text{QCD}} + \text{pQCD} + \text{dA}. \tag{2.1}$$

P$_{\mathbf{QCD}}$ takes its name from the equation of state (EOS), $P_{\mathrm{QCD}}(T)$, and covers the low-p_T bulk observables in the non-perturbative regime. **pQCD** comprises the high-p_T evidence that can be described with perturbative QCD (pQCD) approaches. Control experiments such as deuteron-ion (d+A) collisions comprise the third term, **dA**. The term sQGP was coined in [33] to separate this strongly-interacting liquid-like QGP from a weakly interacting gas of partons, labeled wQGP, that was expected by many [34, 35, 36].

In the decade since, much more supporting evidence has been gathered by the RHIC and recently the LHC, and theoretical descriptions and understanding of all stages of a collision have steadily improved. Theoretical descriptions of many properties of the medium have reached a point where the differentiation between "QGP" and "system displaying the properties of a QGP" is becoming moot. Authors now speak of a "Standard Model of of Heavy Ion Collisions" [37, 38], albeit often still in quotation marks, but it can be said that the search for the Quark Gluon Plasma has ended and the quantitative exploration of its properties has begun.

The three evidence lines summarized here will be reviewed in more detail after the introduction of the basic concepts and terminology needed.

2.1 Characterization of a Heavy Ion Collision

2.1.1 Terminology and Kinematic variables

The primary observables in High Energy Physics (HEP) are origin, momentum, and charge of particles with a sufficiently long path length in a detector volume, on the order of

a meter, i. e. long-lived hadrons (neutrons, protons, pions, kaons, potentially Ξ, Σ, Λ^0) and leptons (electrons, muons, photons; neutrinos live long enough but are very hard to detect). Particles originate from *vertices*, typically described in cartesian coordinates V_x, V_y, V_z in the lab frame, where by convention (in a collider) the z-axis points along the beam pipe. x and y are arbitrary choices. The collision point is called the *primary* vertex. Other vertices, such as from decays, are *secondary* vertices. Note that the spatial extent of the primary vertex in a heavy ion collision is on the order of tens of fermis, many orders of magnitudes smaller than the resolution of even the most advanced pixel detectors (typically > 1 μm). A particle's momentum always refers to the moment of its creation at a specific vertex; the primary vertex is assumed unless otherwise noted.

Cartesian coordinates for the momentum $\vec{p}$ are not well suited to represent the properties of the system. In a collider, the two incoming beams have equal and opposite momentum and the primary vertex coincides with the center of momentum. However, the p_z dimension, or a polar angle θ, are not boost-invariant, and thus physics-relevant effects are conflated with irrelevant z-boosts that average out if treated relativistically, such as the energy spread of the incoming beams ($\mathrm{RMS}\,(\delta E_{\mathrm{beam}}/E_{\mathrm{beam}}) \approx 0.6 \times 10^{-3}$ at 200 GeV at RHIC [39]), and the individual momenta of interacting partons. Therefore, the polar component of momentum is instead described using *transverse momentum*

$$p_T \equiv \sqrt{p_x^2 + p_y^2}, \tag{2.2}$$

and *rapidity* y, in high energy physics always meaning rapidity with respect to the beam axis, i.e.:

$$y \equiv \frac{1}{2} \ln \frac{E + p_z c}{E - p_z c}. \tag{2.3}$$

Rapidity is additive under z-boosts, so the above-mentioned variations average out over a large enough sample size.

The azimuthal component is properly captured by the angle

$$\phi \equiv \tan^{-1} \frac{p_y}{p_x}. \tag{2.4}$$

To express *invariant yield* $\frac{\mathrm{d}^3 N}{\mathrm{d}^3 \vec{p}}$ in these variables, it is convenient to introduce the transverse mass $m_T^2 = m^2 + p_T^2$, leading to

$$E = m_T \cosh y, \qquad p_z = m_T \sinh y, \tag{2.5}$$

and

$$\frac{\mathrm{d}^3 N}{\mathrm{d}^3 \vec{p}} = \frac{\mathrm{d}^3 N}{p_T \, \mathrm{d}p_T \, \mathrm{d}\phi \, \mathrm{d}(m_T \sinh y)} = \frac{1}{E} \frac{\mathrm{d}^3 N}{p_T \, \mathrm{d}p_T \, \mathrm{d}\phi \, \mathrm{d}y}. \tag{2.6}$$

In many cases, a measured particle's rest mass and therefore energy is not known. In such a case, rapidity is replaced by *pseudorapidity* η.

$$\eta \equiv \frac{1}{2} \ln \frac{|\mathbf{p}| + p_z}{|\mathbf{p}| - p_z}. \tag{2.7}$$

From $(E/c)^2 = |\vec{p}|^2 + m_0^2 c^2$, it follows that the difference between y and η becomes small in the ultra-relativistic regime; it is exactly zero for massless particles as well as for $y = \eta = 0$. Figure 1 illustrates the relationship between pseudorapidity and polar angle. For a differential quantity such as number density $\mathrm{d}N/\mathrm{d}\eta$, the difference between rapidity and pseudorapidity is less relevant than the Jacobian needed to compute $\mathrm{d}N/\mathrm{d}y$, also shown in Figure 1. The variables p_T, ϕ, η are illustrated in Figure 2.

2.1.1.1 Units

Units in high energy physics are for the most part natural units, based on $\hbar = c = k_\mathrm{B} = 1$, and using electron volts (eV) as the base unit of energy:

Energy: $1\ \mathrm{eV} = 1.602 \times 10^{-19}\ \mathrm{J}$

Mass: $1\ \mathrm{eV} \equiv 1\ \mathrm{eV}/c^2 = 1.782 \times 10^{-36}\ \mathrm{kg}$

Momentum: $1\ \mathrm{eV} \equiv 1\ \mathrm{eV}/c = 5.344 \times 10^{-28}\ \mathrm{Ns}$

Temperature: $1\ \mathrm{eV} \equiv 1\ \mathrm{eV}/k_B = 11604\ \mathrm{K}$

However, length ($1\ \mathrm{eV}^{-1} \equiv 1\ \hbar c/\mathrm{eV} = 1.973 \times 10^{-7}\ \mathrm{m}$) and time ($1\ \mathrm{eV}^{-1} \equiv 1\ \hbar/\mathrm{eV} = 6.582 \times 10^{-16}\ \mathrm{s}$) are most commonly quoted in the more characteristic scale of fermis ($\equiv$

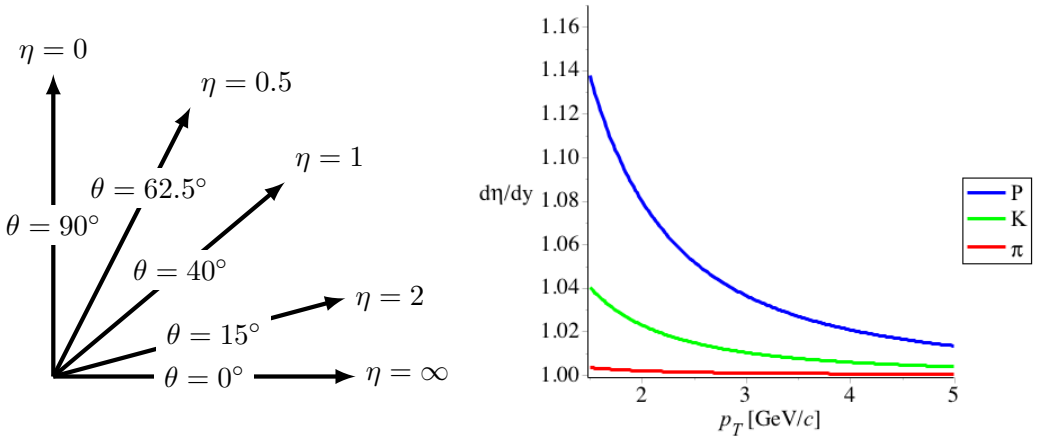

Figure 1. Left: Illustration of the relationship between polar angle and pseudorapidity $y = \ln\left(\tan\frac{\theta}{2}\right)$. Right: p_T dependence of the Jacobian $\mathrm{d}\eta/\mathrm{d}y$ for charged protons, kaons and pions averaged in $|\eta| < 1$.

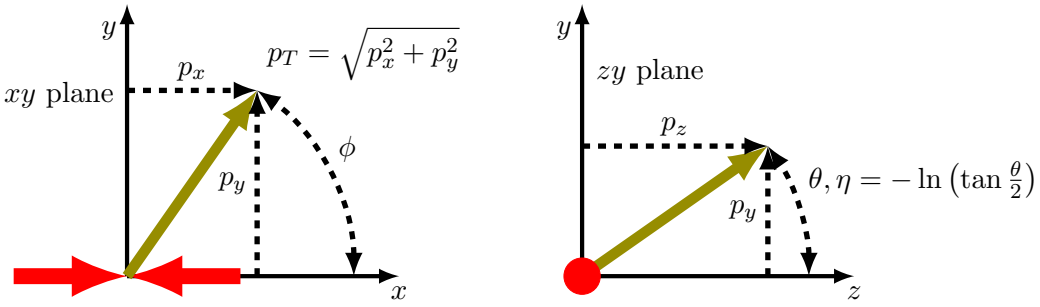

Figure 2. Kinematic variables p_T, ϕ, η. Left: Side view of the collision, with incoming beams shown as red arrows. Right: Frontal view, down the beam line.

femtometers), and fermi/c (1 fm/$c = 3.336 \times 10^{-24}$ s), respectively. Factors of c and other constants are usually restored when quoting or plotting values, except for temperatures where the Boltzmann constant often remains omitted.

2.1.2 Initial Conditions

2.1.2.1 Centrality

Nuclei have a finite physical extension, so they collide with an impact parameter b, see Figure 3. Since a head-on, so-called *central*, collision corresponding to $b = 0$ leads to a qualitatively different system than a glancing or *peripheral* collision with a large impact parameter, collision events are characterized into centrality classes, encompassing fractions of the total cross section instead of impact parameter. The terminology is similar to inverted percentiles: The "$0 - 10\%$ most central" events, corresponding to the 90th percentile, is comprised of those events whose impact parameter is smaller than 90% of all collisions.

The impact parameter cannot be measured experimentally, so centrality determination is done using measurables that have a strong monotonic correlation with b instead. The most common one is the multiplicity of charged particles N_{ch}, used by all four RHIC experiments in different kinematic regions [40, 41, 42, 13, 43], summarized in Figure 4. Other options are in use as well; notably, ATLAS and CMS employ transverse energy E_T measured in forward calorimeters for their primary centrality definition [44, 45].

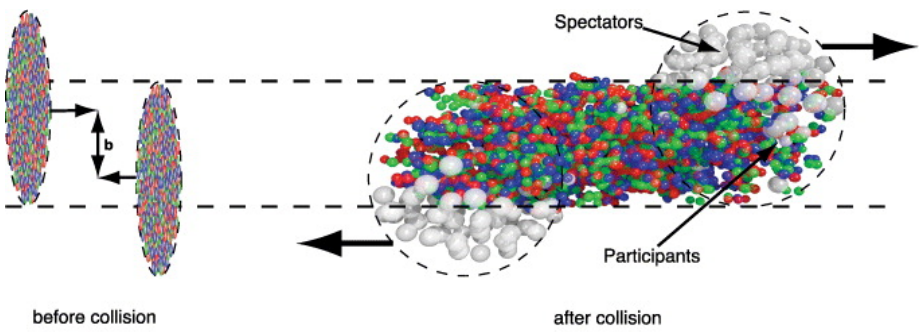

Figure 3. Illustration of two colliding nuclei with impact parameter b [1, 2]. The medium develops in the overlapping zone while the spectators remain unaffected.

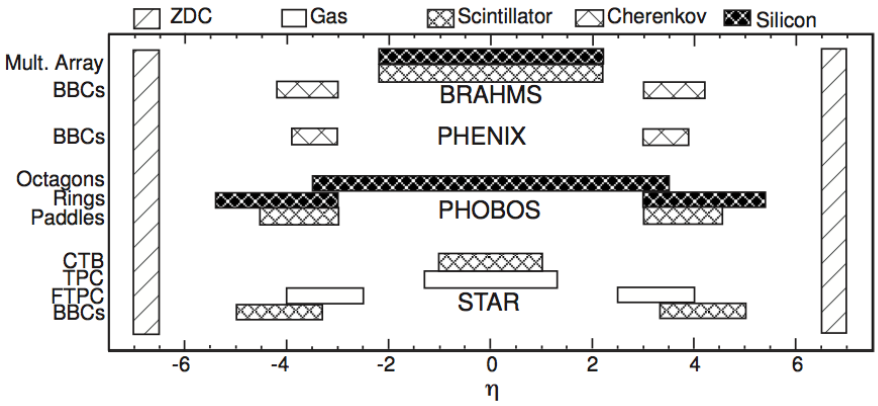

Figure 4. Overview of the pseudorapidity coverage of primary N_{ch} detectors for centrality determination at RHIC [40].

2.1.2.2 Temperature and Energy Density

The exact temperature at which hadronic matter may experience deconfinement into partonic matter, and the nature of this transition, is an active field of research (see for example STAR's recent white paper [46] and references therein). Due to the complexity of the system and the size of the strong coupling "constant" below very large energies, this question cannot be answered perturbatively from Quantum Chromodynamics (QCD). However, numerical computations are possible on a finite lattice, with lattice sites corresponding to quark fields and links to gluon fields (Lattice QCD). At vanishing baryon chemical potential μ_B, a prominent early prediction for the critical temperature is $T_c = 173 \pm 8$ MeV [47], or about 2×10^{12} K. The energy density is proportional to T^4 and the number of degrees of freedom (ndf), and Figure 5 shows how in this computation the degrees of freedom rise rapidly from nucleon to partonic degrees of freedom, until the critical temperature is reached and energy goes solely into heating the system [48, 49].

Values for T_c vary with numerical techniques and treatment of quarks. Recent results from prominent lattice QCD groups seem to converge on a lower value around 150 MeV [50, 51, 52, 53].

The relation between critical energy density and critical temperature in [49] is found to be $\epsilon_c = (6 \pm 2)T_c^4$, or about 0.7 GeV/fm^3. Due to the T^4 dependence, the uncertainty on this value is larger, but a widely accepted estimate is $\epsilon_c \lesssim 1$ GeV. By comparison, nucleon density in normal nuclear matter is usually assumed to be about 0.16 fm^{-3}, corresponding

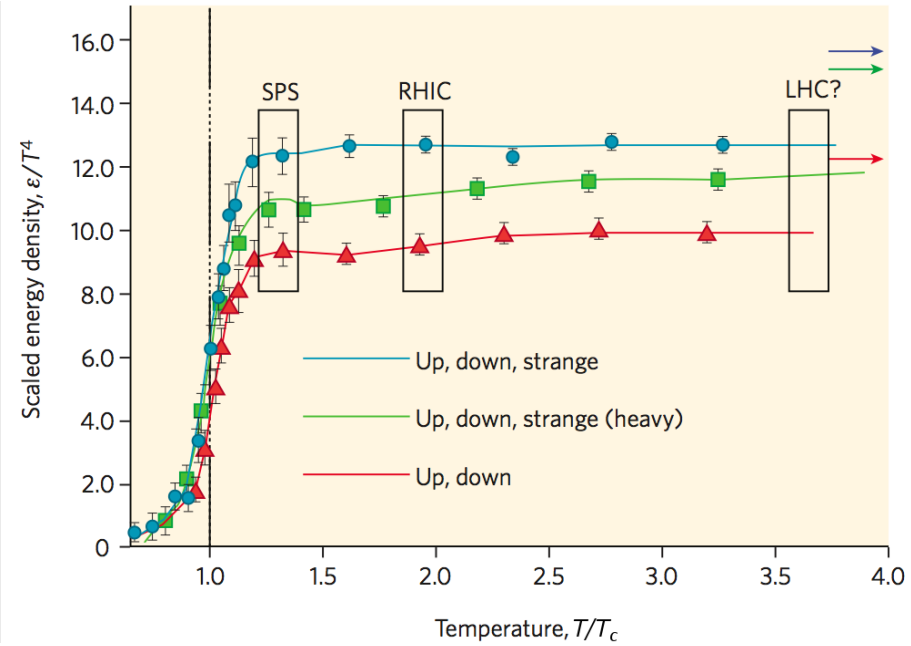

Figure 5. Energy density as a function of temperature calculated for three different treatments of quarks. Arrows indicate the high temperature limit for a gas of gluons and n_f quarks [49], $\epsilon_{SB}/T^4 = (16 + \frac{21}{2}n_f)\frac{\pi^2}{30}$. Boxes indicate maximal initial temperatures reached by SPS, RHIC, and LHC (as projected in 2007). Figure from ref. [48] with the abscissa title corrected to T/T_c; reproduced from [49, 47].

to an energy density of (0.94 GeV)(0.16 fm^{-3}) = 0.15 GeV/fm^3, about five times lower than ϵ_c. This density estimates assumes a nuclear radius of $R = r_0 A^{1/3}$ for mass number A [54, p. 12–15], with an empirical value of r_0 between 1.1 and 1.5 fm, typically 1.2 for the charge radius and 1.4 for "full matter" radius.

Can this be achieved? Naïvely, in a $\sqrt{s_{\text{NN}}}$ = 200 GeV collision an upper bound of the increased energy density could be calculated by multiplying the relativistic length contraction ($\gamma \approx 100$) by two (two overlapping nuclei) and by 100 again (because each nucleon carries about 100 times the energy of a nucleon at rest), for a resulting energy density up to 20000 times higher than in normal matter! Following this logic, the energy density for a QGP could actually be easily reached at $\sqrt{s_{\text{NN}}} = 2$ GeV, well within the reach of Bevatron in the 1950's ($\sqrt{s} = \sqrt{2 \times 6.2 \times 0.938}$ GeV = 3.4 GeV), albeit for protons, not heavy ions.

However, this approach fails to consider that such a maximal overlap would last for only an infinitesimally small amount of time, and that the time of the two relativistic "pancakes" even touching would be on the order of $2Rc/\gamma \sim 0.1$ fm/c. Bjorken proposed to consider the energy removed from the beam, i.e. of particles created in the collision, and to relate it to the thin but finite volume defined by the overlap region of the colliding nuclei and a length determined by the formation time of a medium [55]:

$$\epsilon_{\text{Bj}} \equiv \frac{1}{2\tau_0 c\, A} \frac{\mathrm{d}E_T^{\text{final}}}{\mathrm{d}y} \tag{2.8}$$

The system should be somewhat close to equilibrium, meaning the considered particles should have comparable longitudinal and transverse momentum, a condition roughly equivalent to $|\eta| < 1$ [30]. At $\sqrt{s_{\mathrm{NN}}} = 200$ GeV and with almost perfectly overlapping incoming nuclei (0-5% centrality) the density of charged particles at mid-rapidity is about $\frac{\mathrm{d}N_{ch}}{\mathrm{d}\eta}\big|_{|\eta|<1} \approx 625-655$, and the transverse energy carried per particle is about 570 MeV [30, 56]. Accounting for neutral particles with a factor of 3/2, letting $A = \pi(7\text{ fm})^2$, and assuming a very conservative formation time of 1 fm/c, this leads to an estimated energy density of at least

$$\epsilon_{\mathrm{Bj}}^{\mathrm{RHIC},|\eta|<1} = \frac{3}{2}\frac{1}{2\pi\, 7^2\text{ fm}^3}(2)(650)(0.57\text{ GeV}) \approx 3.6\frac{\mathrm{GeV}}{\mathrm{fm}^3}. \tag{2.9}$$

In fact, the formation time τ_0 may be as low as 0.35 fm/c, leading to estimates up to 15 GeV/fm^3 [32]. In short, energy densities at top RHIC energies exceed the critical value by a factor of four to fifteen, and correspond to temperatures in the range of 250–370 MeV, well beyond where a description as hadronic degrees of freedom is appropriate. One measurement using direct photons in central Au+Au collisions is consistent with models assuming a fast formation time, 0.15-0.6 fm/c, and an initial temperature of 300-600 MeV [57], assuming such photons are of thermal origin.

2.1.2.3 The Glauber Model

The Glauber model provides more fine-grained insight into the initial energy distribution. It also provides a means to bridge centrality as a function of impact parameter

to observable quantities. The premise is illustrated in figure Figure 6: The very early stages of a heavy ion collision are modeled as a superposition of binary collisions of the individual nucleons, and the goal is to determine how many nucleons participate, and how many binary collisions occur. Roy Glauber pioneered the description of nucleons incident on multi-nucleon systems [58, 59]. The main assumption is that at high energies, individual nucleons are undeflected and pass through each other, so that each projectile collides with all target nucleons in its path. Each such nucleon that is part of a collision is called a "wounded" nucleon [60], or a *participant*. Given a nucleon density distribution in the target nucleus, and the cross section for binary collisions, the number of participants N_{part} and the number of collisions N_{coll} (obviously $N_{\mathrm{part}} = N_{\mathrm{coll}} + 1$ in this case), can then be computed analytically [60] or computationally with Monte Carlo simulations (see for example [40]). In a nucleus-nucleus collision, the relationship of N_{coll} and N_{part} is no longer trivial; analytically N_{coll} and N_{part} are calculated using binomial factors [40]; in a Monte Carlo simulation the generalization to nucleus-nucleus collisions is straightforward. Monte Carlo simulations offer the added bonus of generating binary collision positions for further analysis, and since the advent of cheap processing power, Glauber model calculations are most often done this way. It should be noted that the concept of wounded nucleons can be generalized to "used" nucleons, with a finite probability that the nucleon in question is no longer available for further collisions [61, 62]; however, the model as detailed above has proven very successful. In the context of relativistic heavy ion collisions, the Glauber

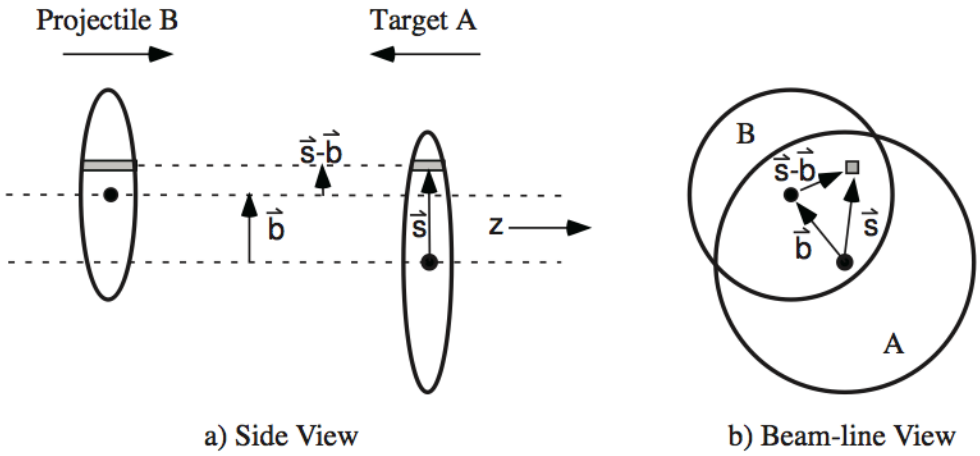

Figure 6. Sketch of a nucleus-nucleus collision with impact parameter b in the Glauber model [40]. One nucleon at $\vec{s}$ in the projectile and its "path" through the target nucleon are highlighted.

model is almost exclusively understood to use Monte Carlo simulations and the simpler wounded nucleons.

As mentioned, two key ingredients are required [40, 63]:

Inelastic Nucleon-Nucleon Cross Section

In high energy nuclear collisions, interactions with no (elastic) or small (diffractive) energy transfer are usually ignored, and the inelastic cross section $\sigma_{\mathrm{NN}}^{\mathrm{inel}}$ is used. At 200 GeV, the used values is $\sigma_{\mathrm{NN}}^{\mathrm{inel}} = 41 - 42$ mb [64, 65, 66, 67], consistent with fits to measured cross sections at various collision energies [68].

Nucleon Density Distribution

Nucleon density is modeled from charge density. For most nuclei, the deviation from a spherical shape is small, and the radial charge density is described well with a three-parameter Fermi distribution:

$$\rho(r) = \rho_0 \frac{1 + w\,(r/R)^2}{1 + \exp\left(\frac{r-R}{a}\right)}, \tag{2.10}$$

where r is the distance from the center, ρ_0 is the nucleon density at $r = 0$, R is the nuclear radius, and a is the skin depth, i.e. the length scale over which the density rapidly drops from almost uniform to zero. The w parameter characterizes deviations from a spherical shape; for ^{197}Au it is zero, and the distribution simplifies to a Woods-Saxon form. Parameters are obtained from elastic electron scattering [69].

For deuterons, most commonly the Hulthén formula for the proton-neutron distance r_{pn} is used:

$$\rho(r_{\mathrm{pn}}) \propto \frac{e^{-\alpha\, r_{\mathrm{pn}}} - e^{-\beta\, r_{\mathrm{pn}}}}{r_{\mathrm{pn}}} \quad \Leftrightarrow \tag{2.11}$$

$$\rho(r) \propto \frac{e^{-2\,\alpha\, r} - e^{-2\,\beta\, r}}{2\, r}, \tag{2.12}$$

with parameters $\alpha = 0.228$ fm^{-1} and $\beta = 1.18$ fm^{-1} [64].

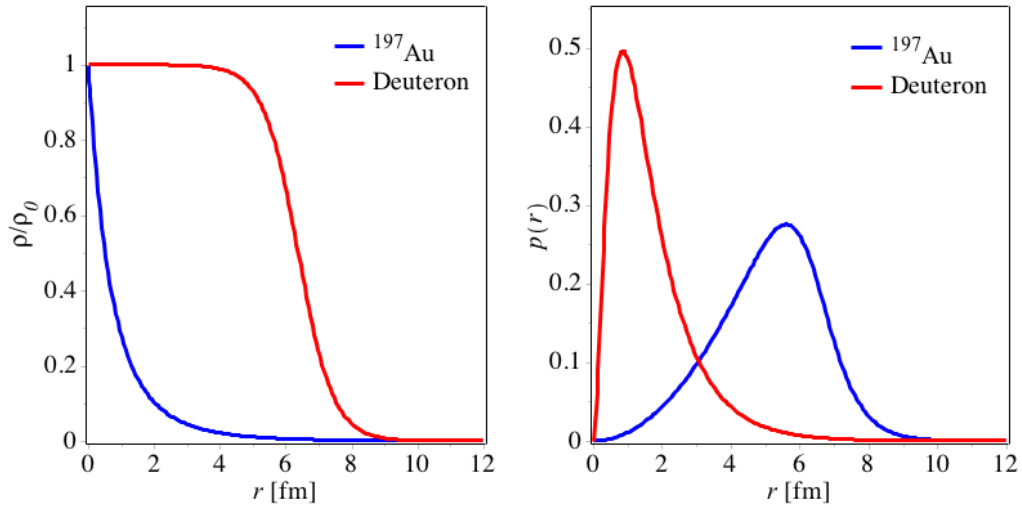

Figure 7. Normalized radial nucleon density (left) and probability distribution (right) for ^{2}H and ^{197}Au (using $R = 6.38$ fm, $a = 0.535$ fm, $w = 0$ [69]).

The probability of finding a nucleon in a thin shell at a distance r from the center is then $p(r) \propto 4\pi r^2 \rho(r)$ for most nucleons, or $p(r) \propto 4\pi r^2 \rho^2(r)$ for deuterons due to forcing $r_{\mathrm{p}} = r_{\mathrm{n}}$. Radial density and probability distribution are shown in Figure 7.

2.2 Bulk Observables

2.2.1 Elliptic Flow

Hydrodynamic descriptions of the QGP date back to 1974 [70, 71]. Measurements of anisotropy in transverse flow as a signature of the QGP was pioneered by Ollitrault [72]. In an off-center collision, a *reaction plane* is defined by the beam direction z and the impact parameter b, see Figure 8. Without collective effects, the momenta of particles produced

in the overlap region would be random and their azimuthal distribution isotropic. If a liquid quickly develops in this almond-shaped region however, then pressure gradients will add to the momenta, preferably in the direction of the reaction plane, see Figure 9. This anisotropic flow is an especially attractive observable because the spatial asymmetry decreases very quickly, thus anisotropic flow probes very early times, within a fm/c of the collision [73].

The azimuthal distribution of particles with respect to the reaction plane can be expressed in a Fourier series [73, 1]:

$$E\frac{\mathrm{d}^3N}{\mathrm{d}^3\vec{p}} = \frac{1}{2\pi}\frac{\mathrm{d}^2N}{p_T\mathrm{d}p_T\mathrm{d}y}\left(1+\sum_{n=1}^{\infty}2v_n\cos\left[n\left(\phi-\Psi_R\right)\right]\right), \tag{2.13}$$

where Ψ_R is the azimuthal angle with the reaction plane. The system is symmetrical with respect to the reaction plane, so there are no sine terms in this expansion. The Fourier components are

$$v_n(p_T,y) = \left\langle\cos\left[n\left(\phi-\Psi_R\right)\right]\right\rangle, \tag{2.14}$$

averaged over all particles in the considered p_T, y window. v_1 is commonly referred to as directed flow, v_2 as elliptic flow.

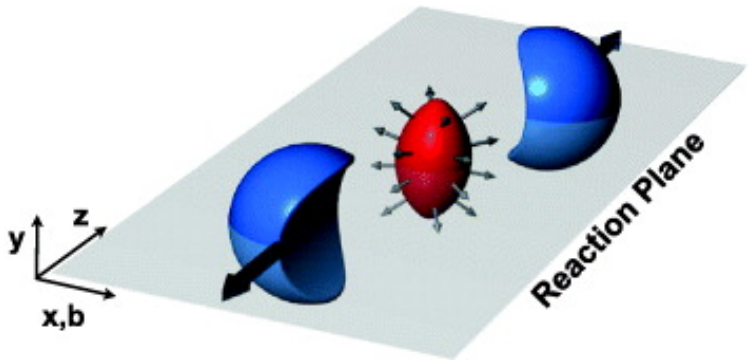

Figure 8. Illustration of the interaction region and reaction plane in a non-central heavy ion collision [1]. Spectators in blue are rapidly speeding away as the almond-shaped fireball expands. The reaction plane is spanned by the beam direction and the impact parameter. Relativistic length contraction is neglected in this sketch.

.

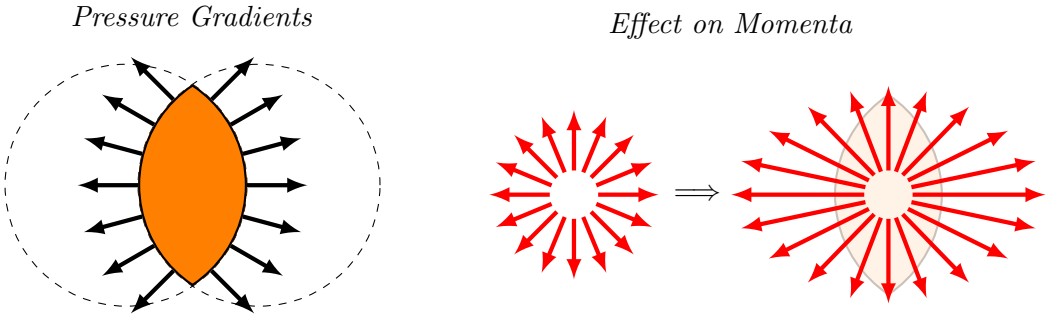

Figure 9. Illustration of momentum anisotropy in a mid-central collision. Left: Pressure gradients between the QGP medium and the surrounding vacuum are normal to the medium surface. Right: The anisotropy of the pressure gradients leads to larger momenta along the shorter axis of the almond-shaped medium.

2.2.1.1 Measuring Flow

The reaction plane is not a direct observable, and multiple approaches exist to measure flow, and flow measurements usually contain an explicit qualifier to name the method by which they were obtained. A number of factors complicate the ideal picture described above and introduce components not due to "true" anisotropic flow, usually called non-flow. The picture in Figure 8 and Figure 9 is suggestive of a homogenous medium formed in the interaction region, identical for all collisions at the same energy and impact parameter. A more realistic scenario is shown in Figure 10. In this sketch, the medium is created in a Glauber MC-type way, from individual, randomly distributed collision points in the in-

teraction zone, leading to significant flow fluctuations in the same centrality class. In fact, higher-order flow harmonics, neglected for a long time, are hypothesized to result from these per-event fluctuations and play a significant role especially in very central collisions where the dominant elliptic flow becomes small while fluctuations are essentially unaffected and v_3 ("triangular flow") becomes comparable or larger than v_2 [5]. In addition, short-range correlations stemming from jets, resonance decays, Hansbury-Brown-Twiss effect, momentum conservation lead to non-flow contributions to measured quantities. The experimental flow measurement methods described below [73, 1] differ in how sensitive they are to these influences and how they address non-flow.

2.2.1.1.1 Event Plane Method

For each flow harmonic an individual approximation Ψ_n to the reaction plane is calculated directly from the anisotropic flow itself, called the *event plane* [74]. This is done via a two-dimensional event flow vector Q_n:

$$Q_{n,x} = \sum_i w_i \cos(n\phi_i) = \vec{Q}_n \cos(n\Psi_n), \tag{2.15}$$

$$Q_{n,y} = \sum_i w_i \sin(n\phi_i) = \vec{Q}_n \sin(n\Psi_n). \tag{2.16}$$

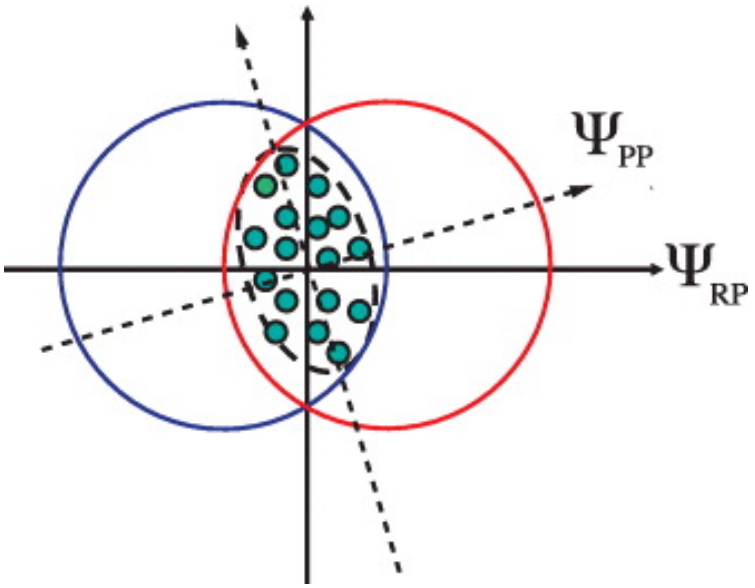

Figure 10. Randomly distributed collisions define the participant plane, offset from the true reaction plane [1].

.

The sum is over all particles, and the weights w_i are chosen to approximate the p_T behavior of v_n. Then the flow harmonic is calculated as

$$v_n\{\mathrm{EP}\}(p_T, y) = \langle \cos\left[n\left(\phi_i - \Psi_n\right)\right]\rangle \,. \tag{2.17}$$

Additional corrections for event plane resolution, detector acceptance etc. can be found in [73, 1]. To reduce non-flow influences, often different subsets of an event are used for finding the event plane and the actual flow value. Enforcing large η gaps between particles reduces short-range correlations.

2.2.1.1.2 Flow from Di-hadron Correlations

In azimuthal di-hadron correlations of flowing particle pairs $\frac{\mathrm{d}N^{\mathrm{pair}}}{\mathrm{d}\Delta\phi}$, v_n is widely assumed to factorize [75]. This can be seen as follows. Assuming the azimuthal distribution with respect to the reaction plane Ψ follows

$$\frac{\mathrm{d}N}{\mathrm{d}\phi} = \left[1 + 2\,v_2 \cos 2(\phi - \Psi)\right], \tag{2.18}$$

then the distribution of the pairs with the difference $\Delta\phi = \phi^A - \phi^B$ can be calculated:

$$\frac{\mathrm{d}N}{\mathrm{d}\Delta\phi} = \int_0^{2\pi} \mathrm{d}\Psi \int_0^{2\pi} \mathrm{d}\phi^A \left(1 + 2v_2^A \cos 2(\phi^A - \Psi)\right)\left(1 + 2v_2^B \cos 2(\phi^A - \Delta\phi - \Psi)\right) \tag{2.19}$$

Because $\int_0^{2\pi} \mathrm{d}x \cos(x + c) = 0$, the product simplifies to

$$\begin{aligned}
\frac{\mathrm{d}N}{\mathrm{d}\Delta\phi} &= \int_0^{2\pi} \mathrm{d}\Psi \int_0^{2\pi} \mathrm{d}\phi^A \left(1 + 4v_2^A v_2^B \cos 2(\phi^A - \Psi) \cos 2(\phi^A - \Delta\phi - \Psi)\right) \\
&= \int_0^{2\pi} \mathrm{d}\Psi \int_0^{2\pi} \mathrm{d}\phi^A \left(1 + 2v_2^A v_2^B \left[\cos(2\Delta\phi) + \cos 2(2\phi^A - 2\Psi - \Delta\phi)\right]\right) \\
&= \int_0^{2\pi} \mathrm{d}\Psi \int_0^{2\pi} \mathrm{d}\phi^A \left(1 + 2v_2^A v_2^B \cos(2\Delta\phi)\right) \\
&= 4\pi^2 \left(1 + 2v_2^A v_2^B \cos(2\Delta\phi)\right)
\end{aligned} \tag{2.20}$$

This derivation does not take short-range correlations from e.g. jets into account, which is why the jet-like component is excluded when this assumption is applied in Section 5.2. Also, the v_1 component does not commonly factorize this way due to momentum conservation. But in many cases, the jet component can be neglected, and one can then extract a measure of v_n from fits to the distribution of pairs of particles in the same given p_T region [76],

$$\frac{\mathrm{d}N^{\mathrm{pair}}}{\mathrm{d}\Delta\phi} \propto \left(1 + \sum_n 2\, v_n^2 \cos(n\Delta\phi)\right), \quad p_T^A \approx p_T^B \tag{2.21}$$

2.2.1.1.3 Cumulant Method

The two-particle cumulant method is essentially identical to extracting v_n from equation 2.21, only skipping the construction of the di-hadron correlation and fitting in favor of calculating the Fourier component directly [73, 77]:

$$v_n\{2\}^2 \equiv \langle \cos(n(\phi^A - \phi^B)) \rangle = \langle u_{n,1} u^*_{n,2} \rangle, \tag{2.22}$$

with unit flow vectors $u_n = e^{in\phi}$.

To reduce non-flow effects, *higher-order* cumulant methods instead construct multi-particle correlations and subtract lower order cumulants in such a way as to eliminate the contribution of two-particle correlations. An example is the fourth-order cumulant method:

$$-v_n\{4\}^4 = \langle u_{n,1} u_{n,2} u^*_{n,3} u^*_{n,4} \rangle - 2\langle u_{n,1} u^*_{n,2} \rangle^2. \tag{2.23}$$

2.2.1.1.4 Other Methods

More methods are described in [73]. The Lee-Yang Zeros method for example corresponds to calculating the large-order expansion in cumulants [78].

2.2.1.2 Method Comparison

A comparison of the various methods is shown in Figure 11. As can be seen, they generally fall into two classes, the two-particle methods are all similar and give a higher value than the multi-particle methods, which are also all very similar to $v_2\{4\}$. In di-

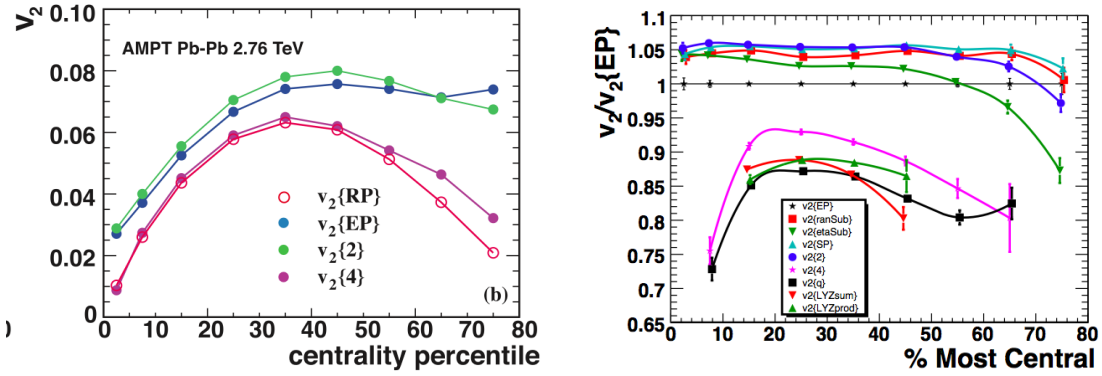

Figure 11. Method comparison for p_T-integrated elliptic flow. Left: Applied to an AMPT simulation [79], based on Glauber-type initial conditions [1]. Right: Various methods used on 200 GeV Au+Au data at mid-rapidity [73].

hadron correlation analyses in STAR that subtract elliptic flow contributions, usually the average of $v_2\{\text{EP}\}$ and $v_2\{4\}$. The corresponding large uncertainty is not present in this analysis since Fourier components V_n are extracted directly and the focus is on their scaling behavior; no attempt is made to factorize them explicitly into v_n.

2.2.1.3 Elliptic Flow Measurements—An Almost Perfect Quark Soup

Elliptic flow was among the earliest and most surprising measurements at RHIC, with an amplitude more than 50% larger than previously observed at SPS [80, 81]. These findings excluded systems such as an ideal parton gas or a hadron resonance gas, and could be

successfully captured within hydrodynamic descriptions assuming very fast thermalization time on the order of 0.5–1 fm/c [82].

Further calculations and measurements with identified particles are shown in Figure 12, taken from [33]. Below about 1 Gev/c, the measured data display mass ordering, a finger print of hydrodynamic evolution that is excellently captured by the ideal hydrodynamic curves. This elliptic flow result has led to the QGP at RHIC often being described as a "perfect liquid". As computational methods advanced, some viscosity was required to capture the data, but the characteristic quantity, shear viscosity divided by entropy density η/s, is found to be close to the ideal limit $\eta/s = 1/4\pi$ in natural units [83, 84]. This lower bound is calculated using duality between perfect fluids and black hole horizons in the context of a strongly coupled $\mathcal{N} = 4$ supersymmetric Yang-Mills theory in the limit of a large number of colors [85].

Above 1-2 GeV/c, Figure 12 shows deviation from this ideal description, but even more striking is the trend reversal between baryons and mesons. The behavior can be reconciled with an assumption that makes this perfect liquid a true quark soup: Flow is acquired at the *partonic level* and the final measured value is the result of *recombination or coalescence* of flowing valence quarks into baryons and mesons [86, 87], i.e.:

$$v_2^{\text{hadron}}(p_T) \approx n_q v_2(p_T/n_q), \tag{2.24}$$

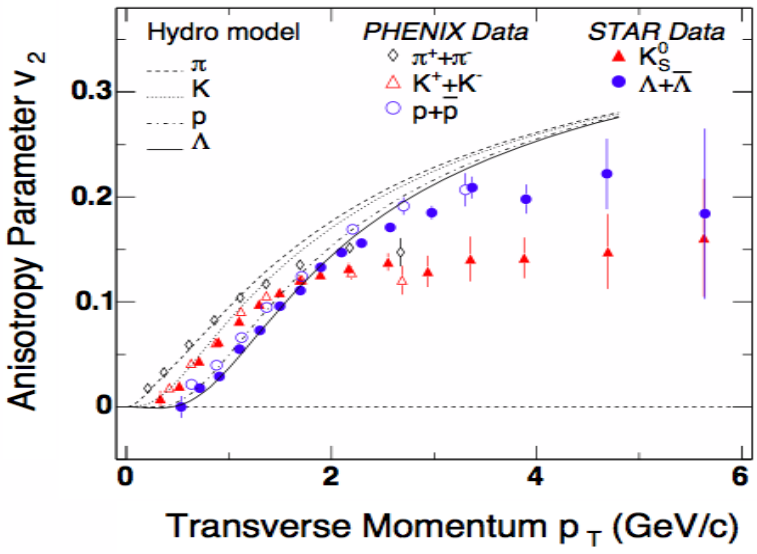

Figure 12. Collection of identified particle v_2 measurements compared to hydrodynamical calculations [33].

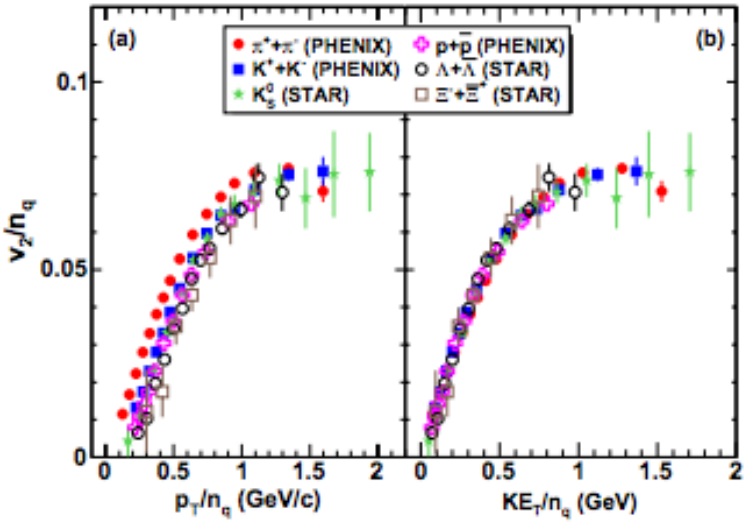

Figure 13. Quark scaling behavior of elliptic flow: v_2/n_q vs. p_T/n_q and KE_T/n_q for many species demonstrates universal scaling behavior [87].

where n_q is the number of constituent quarks. As seen in Figure 13, this scaling holds remarkably true, and when using the transverse kinetic energy $KE_T = m_T - m_0$ instead of p_T [88], all species collapse onto one universal curve.

2.2.1.4 Higher Order Flow Harmonics

Figure 14 shows an example of the azimuthal shape described by $1 + 2\,v_n \cos n\phi$ for n=2,. . . , 5. Comparison with Figure 9 shows that the assumption of a homogenous almond shape would lead to vanishing odd harmonics and dominance of v_2 among even harmonics. Until recently, higher-order, and especially odd, flow components were therefore largely

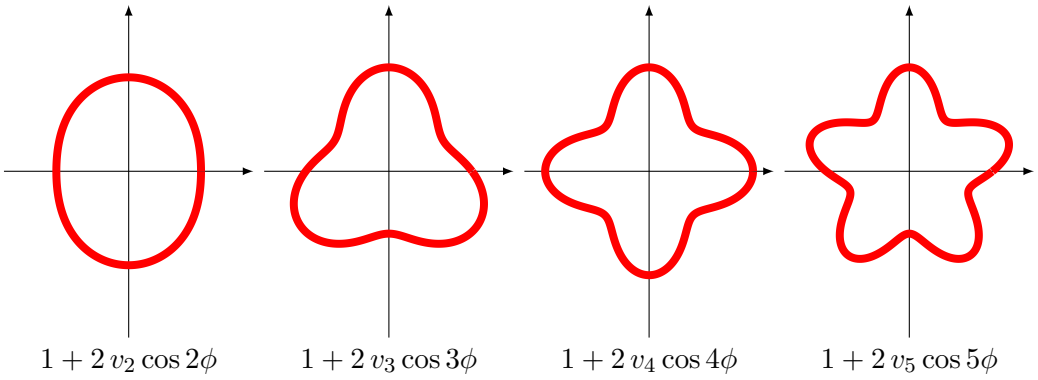

Figure 14. Visualization of azimuthal harmonics v_2, v_3, v_4, v_5.

ignored. Sparked in large part by efforts to explain features in di-hadron correlations, see Section 2.3 below, the role of initial conditions and the need to model flow on an event-by-event basis have been investigated [5].

A Glauber simulation of a mid-central collisions is shown in Figure 15. Apart from shapes consistent with an almond shape, initial state fluctuations can also frequently lead to shapes with significant odd harmonic components. Third and higher harmonics have now been measured by the RHIC and LHC experiments [89, 90, 91, 92, 93].

Theoretically, initial conditions are described mainly in three ways [6]: The Monte Carlo Glauber approach is described in Section 2.1.2.3. The MC Kharzeev-Levin-Nardi (MC-KLN) [94] describe high-energy nuclei as a *Color Glass Condensate* [9, 95], a formalism where the growth of gluon distributions with energy slows down and saturates at very high energies. The IP-Glasma description presents a refinement of the KLN approach, leading

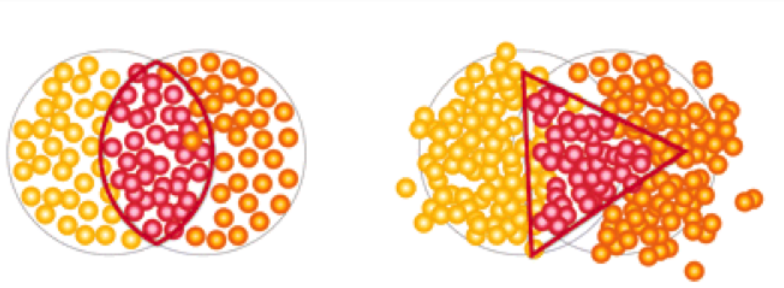

Figure 15. Glauber simulation of a mid-central collisions [3, 4, 5]. Wounded nucleons in the overlap region are shown in red. Elliptic (left) and so called triangular (right) flow patterns arise from different configurations in individual events.

to finer structures in the initial state energy distribution. A comparison of energy density described by the three models is shown in Figure 16, left. The IP-Glasma model, coupled with a relativistic hydrodynamic description of the system, is able to describe RHIC data very well, and again suggests a viscosity η/s close to or at the ideal limit [7].

An outstanding question is whether these higher harmonics follow the same quark number scaling as elliptic flow. There are indications that this may not be the case [96], and part of this study will address this question in a higher p_T range.

2.2.1.5 Baryon/Meson Puzzle—Recombination

A baryon/meson anomaly was first discovered in ultra-relativistic heavy ion collisions at RHIC[97, 8, 98]: in the intermediate transverse momentum region the relative yield of (anti-)protons with respect to pions was found significantly enhanced in central Au+Au

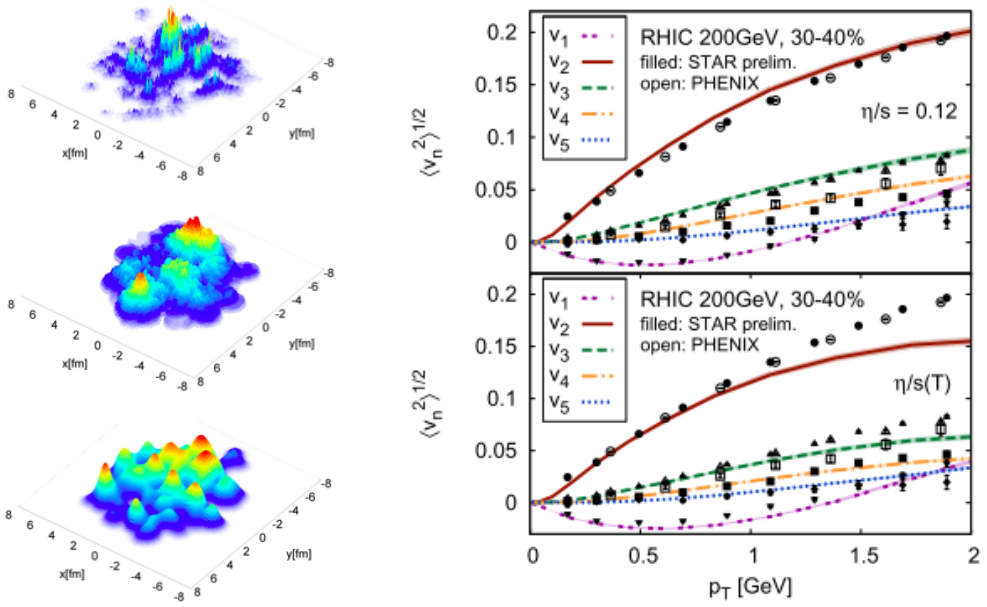

Figure 16. Left: Initial energy distribution calculated in the IP-Glasma (top), MC-KLN(middle), and MC-Glauber (bottom) models [6]. Right: Comparison of mid-central data measured at RHIC to model calculations using IP-Glasma with different assumptions about the medium viscosity [7]

.

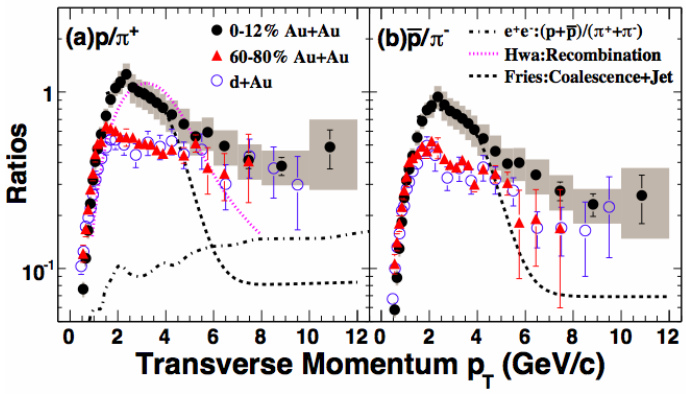

Figure 17. The Proton/pion ratio (for particles and anti-particles) in central Au+Au collisions at 200 GeV is strongly enhanced compared to d+Au and peripheral Au+Au in the intermediate pT range. Two models of the recombination assumption are shown as well [8]

.

collisions compared to peripheral, d+Au, or *pp* collisions, see Figure 17. Similar behavior was found for strange hadrons [99]. Recombination models incorporating coalescence of two or three thermal quarks to form a meson or a baryon, are able to reproduce the observed enhancement [100, 101, 102, 103]. If recombination is a dominant production mechanism compared to fragmentation in the low to intermediate region, then the steep spectrum can explain the observed enhancement: To produce a final state hadron with a given energy, it is energetically favorable to create a baryon with three comparatively low-energy valence quarks rather than a meson with two quarks, see the illustration in Figure 18.

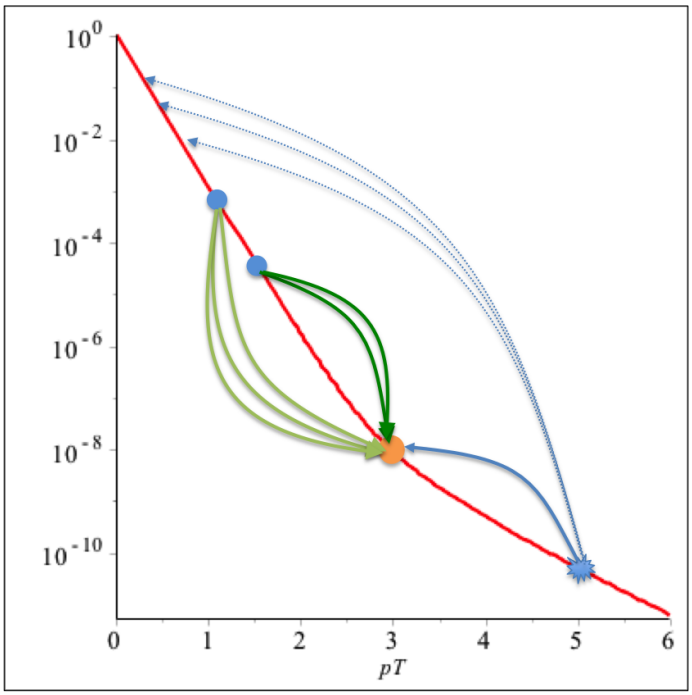

Figure 18. Illustration of baryon enhancement through recombination. A 3 GeV hadron is created either from fragmentation of a higher p_T parton, or recombination of two 1.5 GeV partons (to a meson) or three 1 GeV partons (to a baryon).

2.3 Jet Quenching

2.3.1 Nuclear Modification Factor

High-energy partons are created in highly inelastic collisions of incoming beam partons as back-to-back quark–anti-quark or gluon–gluon pairs (rare processes involving five or more partons are neglected). Colored partons cannot exist in the final state due to the confinement nature of the strong force, instead the growing energy between them creates gluons and additional quark–anti-quark pairs nearly collinear with the original parton, eventually resulting in narrow collimated hadron showers. As the involved partons lose energy in the process, perturbative calculations lose applicability, and this hadronization is described phenomenologically instead. In the Lund string model [104] used in the PYTHIA event generator [105], this is captured by a narrow color flux tube or string and subsequent string breaking.

While the high-energy color-charged quarks or gluons traverse the QGP, they suffer multiple interactions and lose energy in the form of collisions (elastic) and induced gluon bremsstrahlung (inelastic). Collisional energy loss in a QGP of temperature T for a light quark or gluon of energy E can be estimated to [9]

$$-\frac{\mathrm{d}E_{\mathrm{coll}}}{\mathrm{d}l} = \frac{1}{4} C_R \alpha_s(ET) m_D^2 \ln \frac{ET}{m_D^2}, \tag{2.25}$$

where l is the path length in the medium, $m_D \sim \sqrt{\alpha_s}T$ is the Debye mass, α_s is the strong coupling "constant", and $C_R = 4/3$ (quark), $C_R = 3$ (gluon) the color charge. A similar formula for heavy quarks is found in [9].

Radiative energy loss to hard gluon radiation $\omega_c = \frac{1}{\hat{q}}L^2$ in the Landau-Pomeranchuk-Migdal regime where the mean free path λ is much smaller than the medium thickness L, is

$$\Delta E_{\text{rad}}^{\text{LPM}} \approx C_R \alpha_s \hat{q} L^2, \tag{2.26}$$

with the Jet Quenching Parameter $\hat{q} = m_D^2/\lambda$, the average squared transverse momentum transferred per unit path length to a high-energy particle. From this formula, bremsstrahlung can be estimated to be the dominant energy loss mechanism in a QGP at RHIC, a more detailed calculation is shown in Figure 19. An interesting observation from (2.26) is that the radiative energy loss of a high-energy gluon is expected to be larger than that of a light quark by a factor of 9/4.

Large energy loss to the QGP was first observed by comparing the number of high-p_T hadrons found in nucleus-nucleus collisions N^{AA} at a certain centrality to the number that "should" be found if no energy loss occurred. This reference number is the product of the number N^{pp} of particles produced in a binary collision in the vacuum of a p+p collision, and the number of inelastic binary collisions T_{AA}. T_{AA} is determined by Glauber modeling. In the convention used in Section 2.1.2.3, the inelastic cross section $\sigma_{\text{NN}}^{\text{inel}}$ is used

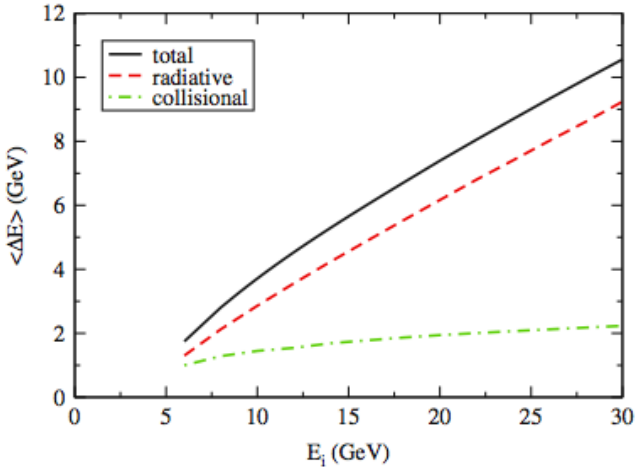

Figure 19. Comparison of radiative and collisional energy loss calculations for light quarks [9].

in the Glauber model and $T_{AA} = \langle N_{\text{coll}} \rangle$ where the average is taken over the considered centrality bin. If the full cross section was used in the model instead, leading to a measure of binary collisions N_{bin} that also includes diffractive and elastic scattering, this number has to be adjusted accordingly, $T_{AA} = \langle N_{\text{bin}} \rangle / \sigma_{\text{NN}}^{\text{inel}}$.

The resulting observable is called the *nuclear modification factor* R_{AA}, in its simplest form for a given rapidity and centrality selection defined as:

$$R_{AA}(p_T) \equiv \frac{\mathrm{d}N/\mathrm{d}p_T}{T_{AA}\mathrm{d}N^{pp}/\mathrm{d}p_T}. \tag{2.27}$$

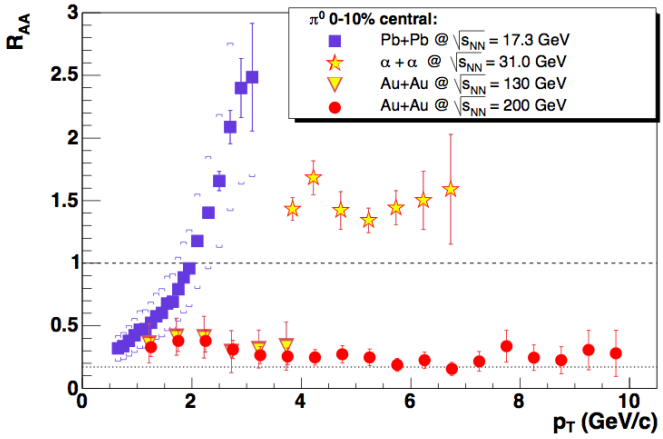

Figure 20. Nuclear modification factor at SPS and RHIC [108].

At RHIC energies, the nuclear modification factor showed that high-p_T particle production is suppressed by a factor of 4–5[65, 66, 64, 106], consistent with strong radiative energy loss [107, 33]. This finding is in stark contrast to the situation at SPS, as shown in Figure 20, indication that a qualitatively new state of opaque, strongly interacting matter had been created.

Two important control studies are shown in Figure 21. In the left panel, R_{AA} measured for direct photons (photons that are created initially in a binary collision, not in a decay) is shown to be consistent with unity, as is expected for particles that do not interact strongly if the normalization factor T_{AA} is correct. The figure also demonstrates that R_{AA} is the same for neutral pions and η-mesons, and well described by radiative energy loss calculations [109]. In the right panel, the nuclear modification factor in central Au+Au

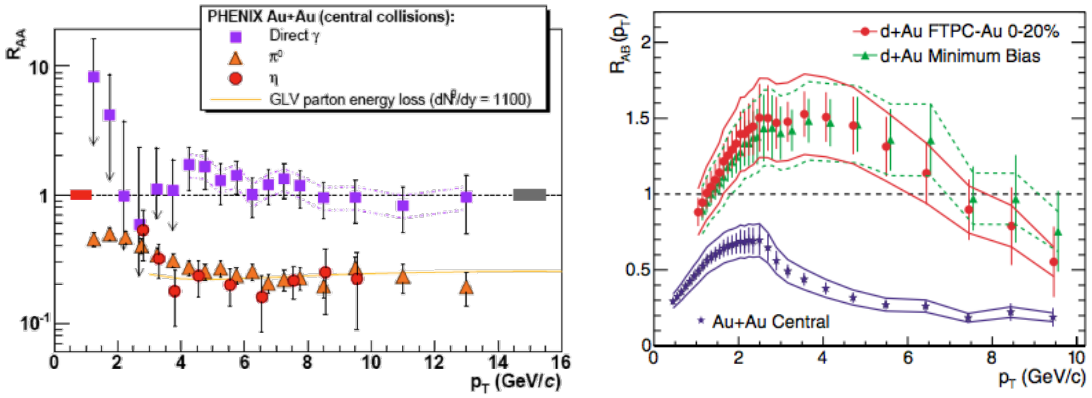

Figure 21. Control measurements of the nuclear modification factor. Left: R_{AA} measured for direct photons are consistent with one [109]. The plot also illustrates the similarity between pions and η-mesons, and good agreement with a radiative energy loss calculation. Right: The large nuclear modification factor in central Au+Au collisions not seen in d+Au, ruling out that cold nuclear matter effects are responsible for the strong suppression [110].

collisions is compared to d+Au, ruling out that cold nuclear matter effects are responsible for the strong suppression [110].

The idealized formula (2.26) assumes a static, uniform, ideal gas of quarks and gluon. To model jet quenching in a realistic expanding QGP, four major frameworks have been developed, all with one characteristic model parameter. The Gyulassy-Levai-Vitev (GLV) approach is characterized by the initial gluon density $\mathrm{d}N^g/\mathrm{d}y$, the BDMPS approach developed by Baier, Dokshitzer, Müller, Schiffer uses $\hat{q}$, AMY uses the temperature T, and the Higher-Twist approach uses energy loss ϵ_0. All approaches however have been successfully matched to data, a GLV calculation is shown in Figure 21.

2.3.2 Jet Tomograpy

A more differential view of energy loss is possible if the axis and momentum of the traversing jet are known or can be approximated. One method to do just that is to consider di-hadron correlations with respect to a *leading hadron* or trigger. The leading hadron in a jet, defined as the final state particle with the highest p_T, is a good approximation of the initial jet axis. After selecting the highest-p_T hadron in a given event, called the *trigger*, the relative azimuth $\Delta\phi \equiv (\phi^{\mathrm{assc}} - \phi^{\mathrm{trig}})$ and/or pseudorapidity $\Delta\eta \equiv (\eta^{\mathrm{assc}} - \eta^{\mathrm{trig}})$ of all associated particles that fulfill additional kinematic restrictions can be computed. A histogram of relative angles for many events gives the di-hadron correlation $\frac{1}{N_{\mathrm{trig}}}\frac{\mathrm{d}N}{\mathrm{d}\Delta\phi}$. visualized in Figure 22. Normalized per trigger, as was done here, this function represents the differential measure of conditional yield (number of particles) in an event where a trigger was found. Cuts on ϕ, η, p_T, centrality, etc. allow fine-grained exploration of different kinematic regions.

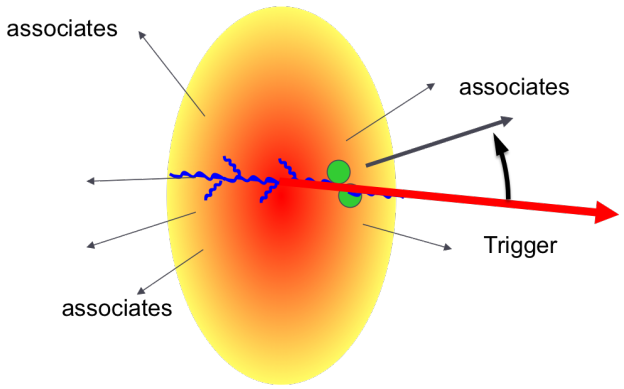

Figure 22. Illustration of a triggered di-hadron correlation. The highest-p_T particle in the event is assigned as trigger, and the angular distribution relative the trigger is recorded.

The result of such a measurement, shown in Figure 23 is compelling [110, 111]. Di-hadron correlations at mid-rapidity with $4 < p_T^{\text{trig}} < 6$ were performed in Au+Au, pp, and d+Au. In pp and d+Au collisions, without modifications in a medium, the jet shower leads to characteristic enhancements close to the trigger (on the near-side) and in the direction opposite the trigger (away-side), i.e. around $\Delta\phi = 0$ and $\Delta\phi = \pi$. In central Au+Au, the same, unmodified, jet-like peak is visible. On the away-side however, particles above 2 GeV/c are completely suppressed. This suppression is consistent with the idea that the trigger comes from a jet created near the surface on the fireball. The corresponding recoil jet then traverses the medium and radiates away energy to where high-p_T particles are no longer measurable. The left panel demonstrates what happens to this energy. The number

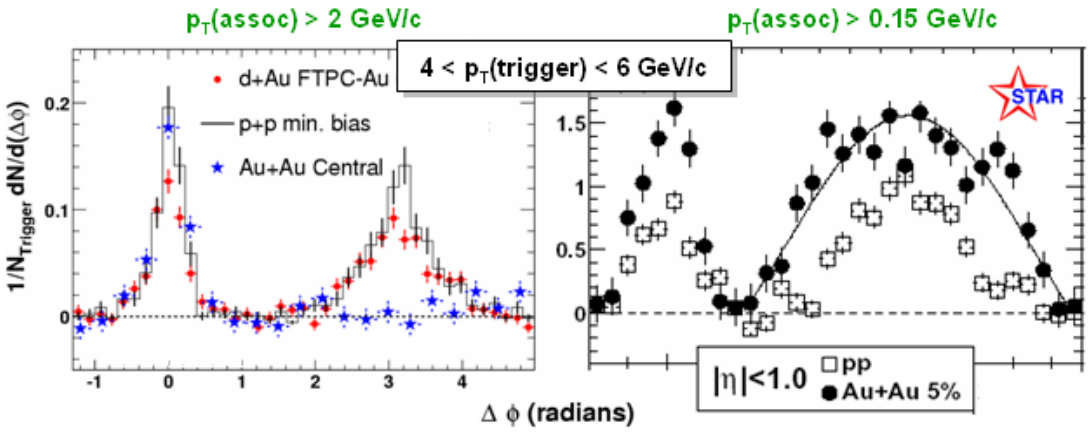

Figure 23. Triggered azimuthal di-hadron correlations with $4 < p_T^{\rm trig} < 6$ GeV/c at 200 GeV in Au+Au, d+Au (left only), and pp. Left: $p_T^{\rm assc} > 2$ GeV/c [110] leads to strong away-side suppression in Au+Au not seen in pp and d+Au. Right: For $p_T^{\rm assc} > 2$ GeV/c [111] away-side enhancement is seen in Au+Au.

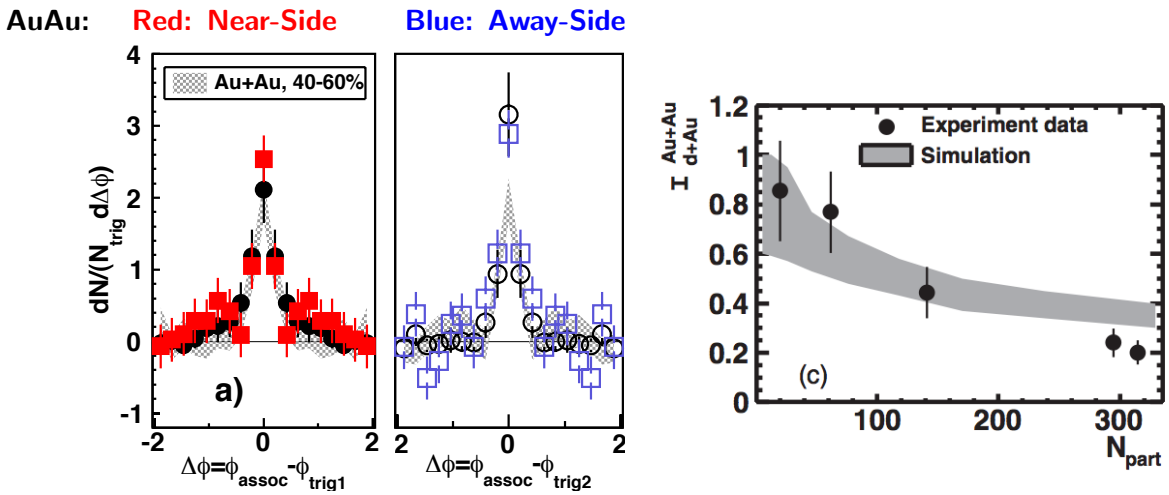

Figure 24. Left: Dijet-triggered $\Delta\phi$-correlations in central and mid-central Au+Au on near-and away-side show no modification compared to d+Au. $5 < p_T^{\mathrm{T1}} < 10$ GeV/c, 4 GeV/$c < p_T^{\mathrm{T2}} < p_T^{\mathrm{T1}}$, $1.5 < p_T^{\mathrm{assc}} < 4$ GeV/c [112]. Right: Conditional di-jet survival probability in Au+Au data compared to expectations from a Glauber-based core-corona model.

of low-p_T particles is actually enhanced and spread out over a broader away-side, consistent with expectations from radiated gluons.

A refinement on this measurement supports the notion of jets only surviving to produce high-p_T leading hadrons if they originate from the surface of the fireball. The so-called 2+1 correlations selects only events that have two similarly high-p_T triggers back-to-back

with each other [112, 113]. The individual jet-like components with respect to the two triggers then show no modification, see Figure 24, suggesting that what few dijets are found were actually created near the surface and tangentially to the fireball. The probability of their survival is consistent with a simple Glauber-based estimate assuming a transparent, vacuum-like corona and an opaque core in which a high-p_T immediately loses enough energy to no longer produce a high enough trigger.

The away-side energy redistribution is illustrated in in jet-hadron correlations, constructed identically to di-hadron correlations but using jet axes and energies obtained from jet reconstruction algorithms [114]. The away-side widths in the top panel of Figure 25 are suggestive of medium-induced broadening. The bottom panel demonstrates the energy redistribution from high to low p_T, characterized by D_{AA}, the difference in the total integrated transverse momentum of away-side jet-like associated particles between Au+Au and pp. This significant softening is consistent with radiative/collisional energy loss models for parton interactions within the Quark-Gluon Plasma.

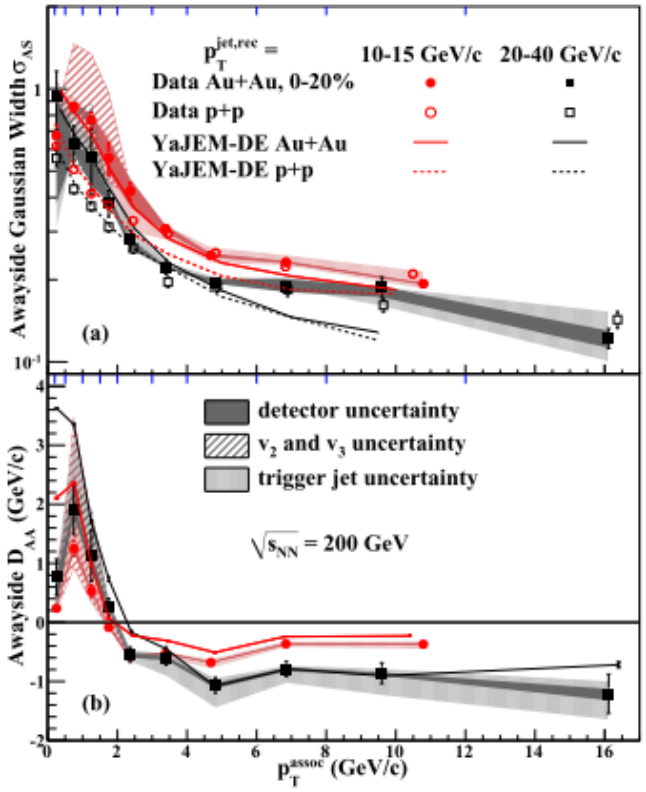

Figure 25. Away-side properties as a function of p_T^{assc} found in jet-hadron correlations at 200 GeV [114]. Top: Gaussian widths of the away-side in central Au+Au compared to pp. Bottom: D_{AA}, the difference in the total integrated transverse momentum of away-side jet-like associated particles between Au+Au and pp. Model calculations from [115] capture the data well.

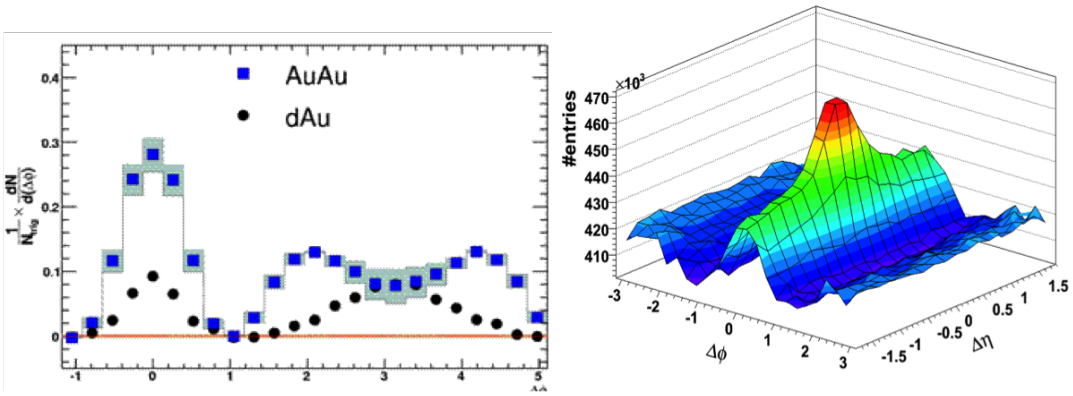

Figure 26. Left: Azimuthal di-hadron correlation with $3 < p_T^{\mathrm{trig}} < 4$ GeV/c and $1.3 < p_T^{\mathrm{assc}} < 1.8$ GeV/c at 200 GeV in Au+Au and d+Au [116]. A prominent double hump structure as visible on the away-side. Right: Two-dimensional correlations di-hadron correlation with $3 < p_T^{\mathrm{trig}} < 4$ GeV/c and $p_T^{\mathrm{assc}} > 2$ GeV/c reveal a narrow long-range rapidity structure at small relative azimuth in Au+Au[117].

2.3.3 The Ridge and the Double Hump

Two striking, seemingly unrelated, features discovered in di-hadron correlations at STAR are shown in Figure 26. The left panel shows di-hadron correlations constructed in the same way as in Figure 23, but with a different p_T selection. The away-side is no longer suppressed but instead severely distorted into a double-hump structure, suggestive of Cherenkov or Mach-cone like emission as a parton at supersonic or superluminal speed.

Such a pattern would allow a direct measurement of either the speed of sound or the refractive index of the QGP.

At the same time, two-dimensional di-hadron correlations $\frac{1}{N_{\rm trig}}\frac{{\rm d}^2N}{{\rm d}\Delta\phi{\rm d}\Delta\eta}$. revealed an unexpected narrow long-range rapidity structure at small relative azimuth in Au+Au [117, 25], shown in the right panel of Figure 26. Further investigation indicate that the ridge has bulk-like spectra and particle ratios, and that its magnitude is approximately constant as a function of $p_T^{\rm trig}$.

The ridge has been referred to as a "theoretical free for all". Many models with very different assumptions have been proposed, such as momentum kicks [118], shock waves [119], glasma flux tubes [120, 121], turbulent color fields [122], radial flow [123], recombination [124, 125], or interrelation of jet quenching and transverse flow[126]. A review and comparison to data of many of these assumptions and models is found in [127].

One model stands out as the most prevalently accepted one today. It explains both the conical emission structure on the away-side and the near-side ridge as resulting from inhomogeneous fluctuating initial conditions, which are then translated into final state higher order flow harmonics[5]. Specifically, the third harmonic or triangular flow would lead to the characteristic enhancements at $\Delta\phi \approx 0$ and $\Delta\phi \approx \pi \pm \pi/3$, illustrated in Figure 27. The cone structure would be especially prominent in Figure 26 because the elliptic flow contribution was subtracted using the so-called zero-yield-at-minimum assumption (ZYAM), as was common practice in di-hadron correlations [75]. Without this subtraction, the triangular flow term leads to significant away-side broadening. As discussed in Section 2.2.1.4,

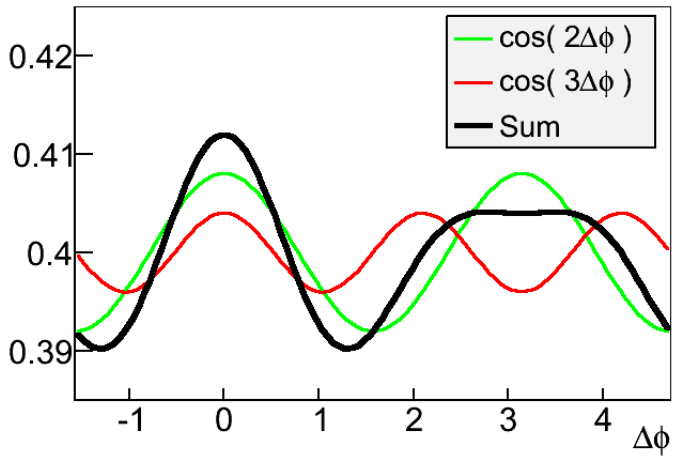

Figure 27. Illustration of elliptic and triangular flow

these higher order flow harmonics have since been measured, and hydrodynamical models describe them well.

But questions remain. Is the ridge fully described by these flow harmonics? Do the harmonics scale with quark content as expected if the mechanism that translates them into final state hadrons is the same as for elliptic flow? And recently, ridge-like correlations have been found in high-multiplicity p+p and p+Pb collisions at the LHC [128, 129, 130], providing further challenges for the theoretical explanations of the ridge.

2.4 This Analysis

In this work, I study two-dimensional $\Delta\phi$-$\Delta\eta$ correlations in 0-10% most-central Au+Au measured with the STAR detector. Trigger hadrons are required to obey $4 < p_T^{\rm trig} <$

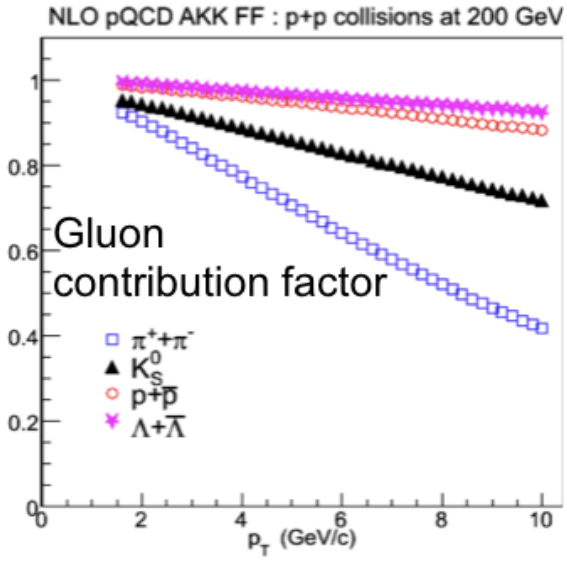

Figure 28. Expected gluon jet contribution to final state hadrons, obtained from next-to-leading-order calculations [10, 11].

5 GeV/c. The correlations are separated between pion and non-pion triggers. Non-pions in this case are a combination of protons and kaons, with known proportions. While it would be desirable to separate them further, such a separation is currently prohibited by experimental and statistical limitations. The p_T of associated particles are required to be between 1.5 and 4 GeV/c, and associated particles are unidentified, i.e. identical between trigger sets. Long range and short range correlation features are considered separately.

The jet-like component at small angles can be isolated by subtracting the long range correlation features, since in this selection they are flat in $\Delta\eta$. The comparison of jet-like yield between leading pions and non-pions gives access to two possibly competing effects:

On the one hand, the ratio of protons to pions in the trigger p_T range is enhanced by about 50% in central Au+Au, indicating under the recombination scenario that a relatively larger fraction of proton than pion triggers originate in fact from recombined partons and do not contribute jet-like yields, thus diluting the trigger pool. Jet-like yields are calculated per trigger, so the effect of recombination should be observable, and constrainable, by relatively *lowered* yields for proton compared to pion triggers.

On the other hand, in this p_T range and above, leading pions are expected to start biasing more and more toward quark–anti-quark jet pairs, see Figure 28. The factor of 9/4 in expected radiative energy loss gluon radiation, could lead to yield enhancements for the proton-rich trigger set.

To exclude the influence of cold nuclear matter effects, measurements of jet-like correlated yield will be compared to data from minimum-bias d+Au collisions at $\sqrt{s_{NN}} = 200$ GeV

Furthermore, the kinematic selection was chosen such that at long range the double-hump is present (if elliptic flow were subtracted), the ridge is a prominent feature, and elliptic flow is expected to exhibit quark number scaling. Two-dimensional fits excluding or accounting for the short-range jet component, allow the extraction of products $V_n = v_n(p_T^{\rm trig})v_n(p_T^{\rm assc})$ of the Fourier components describing hydrodynamic behavior. The contribution $v_n(p_T^{\rm assc})$ from associated particles is the same for all triggers and factors out, so the scaling behavior of the V_n gives new information into the validity of assumptions in the predominant ridge model. Alternative models can capture the 2D data equally well, using only a gaussian for the ridge, and the first and second harmonic, associated with momentum conservation and elliptic flow of an essentially smooth medium. The implications of the coefficients obtained from such a model applied to the correlations separated by trigger identity will be considered as well.

CHAPTER 3

STAR AND RHIC

3.1 The Relativistic Heavy Ion Collider

RHIC is a multi-purpose accelerator facility located at the Brookhaven National Lab (BNL) on Long Island, NY. Its main purpose is to accelerate and collide heavy ions, but it also has proton-proton (pp) capabilities and is in fact the largest polarized pp collider in the world. The top collision energy per nucleon pair in the rest frame is $\sqrt{s_{\mathrm{NN}}} = 200$ GeV for ions and just over 500 GeV for pp. Collision systems to this date are pp, $^{63}\mathrm{Cu} + {}^{63}\mathrm{Cu}$, $^{197}\mathrm{Au} + {}^{197}\mathrm{Au}$, $^{238}\mathrm{U} + {}^{238}\mathrm{U}$, as well as the asymmetric systems $^{197}\mathrm{Au} + {}^{63}\mathrm{Cu}$ and $^{2}\mathrm{H} + {}^{197}\mathrm{Au} \equiv \mathrm{d} + {}^{197}\mathrm{Au}$.

A variety of lower collision energies can be achieved. The Beam Energy Scan program explores the onset of deconfinement and a possible critical point in the QCD phase diagram, so far with collision energies of 7.7, 11.5, 14.5, 19.6, 27, 39, and 62 GeV, adding to early runs at 130 GeV.

The facility is shown in Figure 29. The main ring has a circumference of about 3.8 km. Ions originate in the Tandem Van de Graaff accelerators. There are two available Tandem Van de Graaff accelerators allowing for different ion species. Ions are boosted to 100 MeV per nucleon in the Booster Synchrotron. They are then injected into the Alternate Gradient Synchrotron and accelerated to 8.86 GeV (Au ions). At this point they are fully ionized.

Finally they are injected into the main storage ring and accelerated to their final energy. Particles circulate in opposite directions in two bean pipes, arbitrarily called "blue" and "yellow". Two rings of helium-cooled superconducting magnets operating at 3.5 T are used to bend and focus the beams [39].

At top energy, ion "fills" usually last for up to ten hours. In the 2010 Au+Au run period at $\sqrt{s_{\rm NN}} = 200$ GeV, each beam consisted of 103 out of 111 possible bunches and 1.1×10^9 ions per bunch, resulting in an average luminosity of $20 \times 10^{26}{\rm cm}^{-2}{\rm sec}^{-1}$, 10 times the original design goal [39, 131]. In the 2008 d+Au period at the same energy, up to 95 bunches consisting of 1.2×10^{11} deuterons and 1.0×10^9 gold ions each allowed peak luminosities of up to $38 \times 10^{28}{\rm cm}^{-2}{\rm sec}^{-1}$ [132]. Under normal circumstances, the beam is dropped and replaced with a fresh fill around the time when the instantaneous luminosity has fallen to a point where a fresh beam provides more collisions per time unit than are lost due to the down time. In *pp* runs, protons originate in the Linear Accelerator (LINAC) and exit at 200 MeV, otherwise the process remains essentially the same.

The particles are eventually brought to collision in up to four interaction points. Currently, two experiments are active: The STAR detector at point 2 in Figure 29, and the PHENIX detector at 3. The PHOBOS and BRAHMS experiments were located at 4 and 6 respectively; they ceased operations after completing their scientific programs in 2006. Two smaller programs explore exclusively polarized *pp* phenomena: The pp2pp was originally close to point 6 and is now part of the STAR collaboration and located in the same interaction point; A_NDY is a feasibility study in the former BRAHMS interaction point.

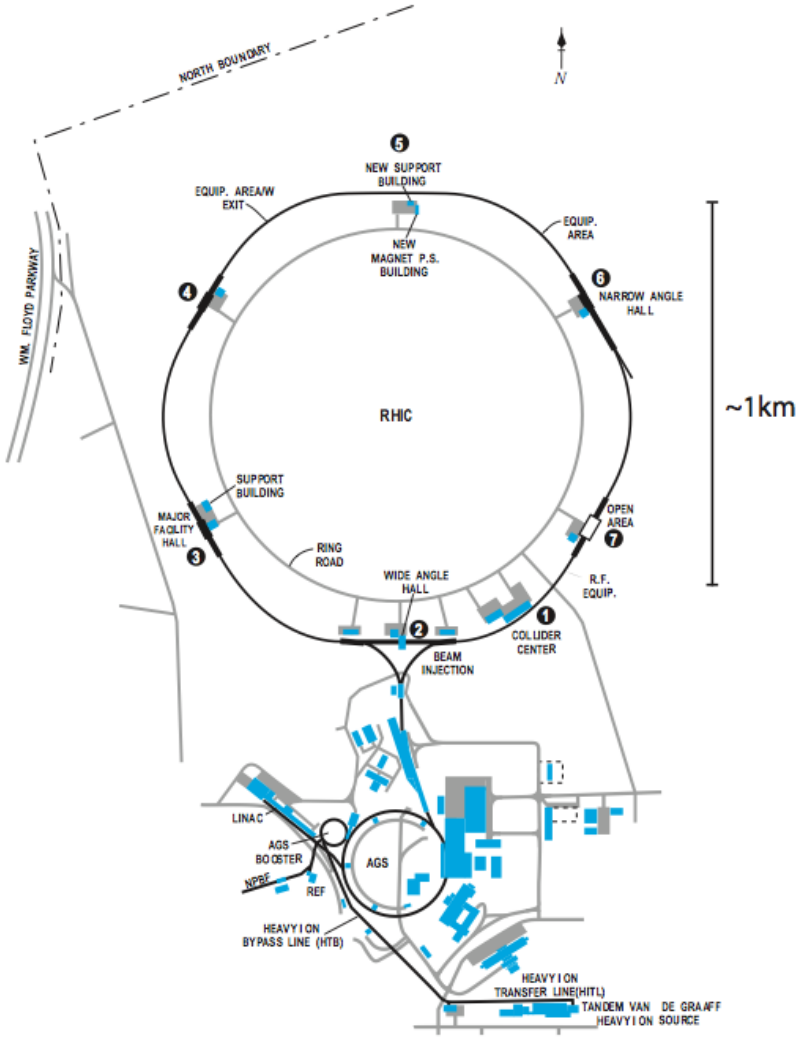

Figure 29. Schematic view of the RHIC facilities at Brookhaven, from [12].

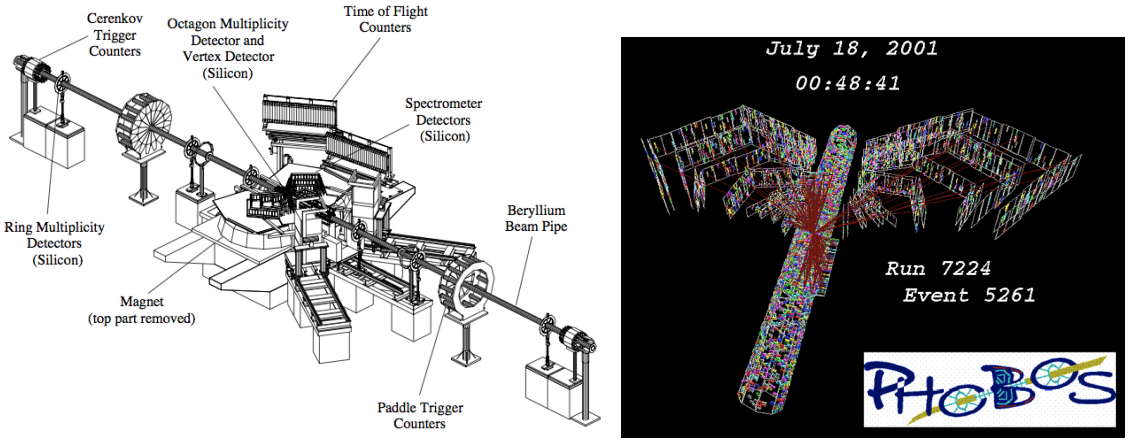

Figure 30. Left: Schematic view of the PHOBOS detector [13]. Right: Event display, from [14].

3.1.1 PHOBOS

The original concept for this experiment was the Modular Array for RHIC Spectra (MARS). The final design was a slightly scaled down, less expensive version and acquired the name PHOBOS [133]. A schematic layout and event display are shown in Figure 30.

The key design goals behind PHOBOS, based on the philosophy that a priori very little is known about the created matter, were large acceptance, reach to slow particles at very low p_T, and high trigger rate in order to not miss rare events [133, 13]. To achieve this, the detector had a multiplicity array covering eleven units of pseudorapidity and almost complete azimuth, a vertex detector with high accuracy better than 0.2 mm [134], and a two-arm, back-to-back magnetic spectrometer including a time-of-flight wall for particle

identification, as well as trigger and centrality detectors. The spectrometer covered 0.2 rad in azimuth and about 0.7 units of pseudorapidity between $0 < \eta < 2$. Using a a 2.2 T dipole magnet, momentum measurements and particle identification of charged tracks were possible down to 30 MeV [135].

A signature measurement, including the first RHIC publication published only six weeks after the end of the first run, was the pseudorapidity and centrality dependence of charged particle multiplicity, showing signs for much higher particle and energy densities than what would be expected from simple *pp* superposition [136, 137]. An overview of major results as of 2005 can be found in the PHOBOS white paper[30].

3.1.2 BRAHMS

BRAHMS was conceived mainly to explore the forward region at large rapidity with high precision momentum resolution and good particle identification; the acronym stands for Broad RAnge Hadron Magnetic Spectrometers [138, 16]. The layout is shown in Figure 31.

The main components of BRAHMS were two movable magnetic spectrometers, the Forward Spectrometer (FS) between 2.3° and 15°, and the mid-rapidity Spectrometer (MRS) between 30° and 90° relative to the beam line. More details about coverage is shown in Figure 31. Both spectrometers had small solid angles. The FS consisted of four magnets to bend charged tracks, two time projection chambers (TPCs) and three drift changers for tracking, two time-of-flight (TOF) hodoscopes, and two Cherenkov detectors for particle

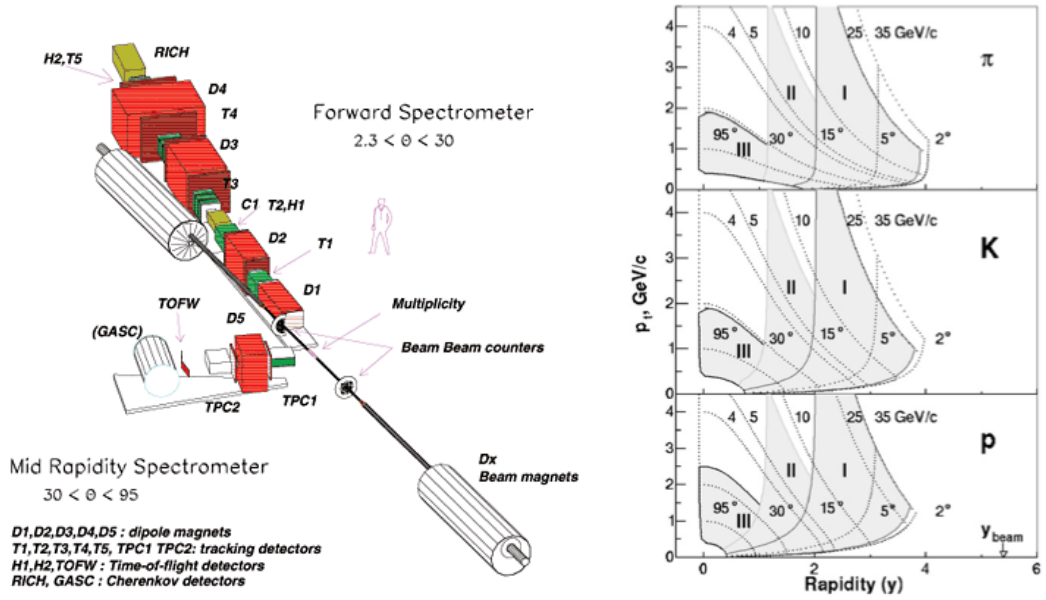

Figure 31. Left: Schematic view of the BRAHMS detector [15]. Right: Acceptance for various species and kinematic regions [16]. Region I and II show the acceptance of the forward spectrometer with two different configurations. Region III shows the acceptance for the mid-rapidity spectrometer.

identification. The MRS had another magnet, two time projection chambers, and a TOF for particle identification [16].

A signature result was the centrality and η dependence of the nuclear modification factor in d+Au collisions [29], providing evidence and constraints for a possible precursor state to the QGP, the so-called color glass condensate (CGC). An overview of BRAHMS evidence for CGC and QGP formation as of 2005 can be found in the BRAHMS white paper [56].

3.1.3 A_NDY and pp2pp

The pp2pp program studies elastic and inelastic polarized *pp* collisions at very small scattering angles. It uses specialized movable "Roman Pots" containing a detector package of four micro-strip detector planes, two each for x and y dimension [139, 17]. Originally located in the BRAHMS interaction point, the experiment is now part of the STAR collaboration and the Roman Pots are at 55.5 m and 58.5 m from the STAR IP, see Figure 32. A recent result is a precision measurement of the single spin asymmetry [17].

The A_NDY experiment in the former BRAHMS location at the 2 o'clock position is a feasibility study to measure the single spin asymmetry A_N for Drell-Yan (DY) production [18]. The schematics are shown in Figure 32. Apart from beam-beam counters (BBC) and zero-degree calorimeters (ZDC), it consists mainly of two left-right symmetric hadronic (HCal) and electromagnetic calorimeters (ECal) each arranged to measure predominantly in the forward region $2.5 < \eta < 4.0$. The collaboration recently published first measurements of forward jet production from transverse-polarized *pp* collisions [140].

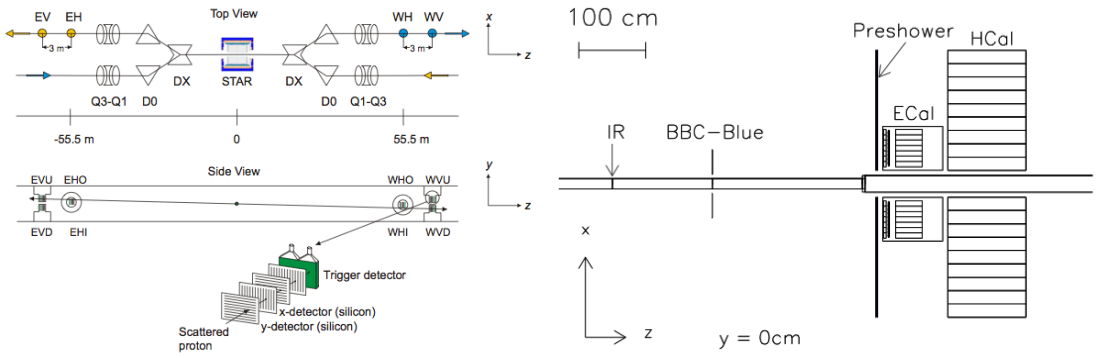

Figure 32. Schematic view of the pp2pp experiment [17](left), and the A_NDY experiment in 2011 [18] (right).

3.1.4 PHENIX

PHENIX, the Pioneering Hadron Electron Nuclear Interaction eXperiment, emerged from the combination of three originally independent proposals. All three shared the general goal of studying rare probes of the QGP [141]. Within the budget constraints, PHENIX therefore emphasized good particle identification and high data-taking rate. It is a complex detector system; its main components are four arms, two covering mid-rapidity and two in forward and backward direction, supplemented by global detectors [42], see Figure 33. In 2011, a silicon vertex tracker (VTX) was added. The original documentation can be found in References [142, 143, 144, 145, 146, 147, 148, 149, 150]. For an overview of recent and planned upgrades, please refer to recent dissertations, such as [151, 152, 153].

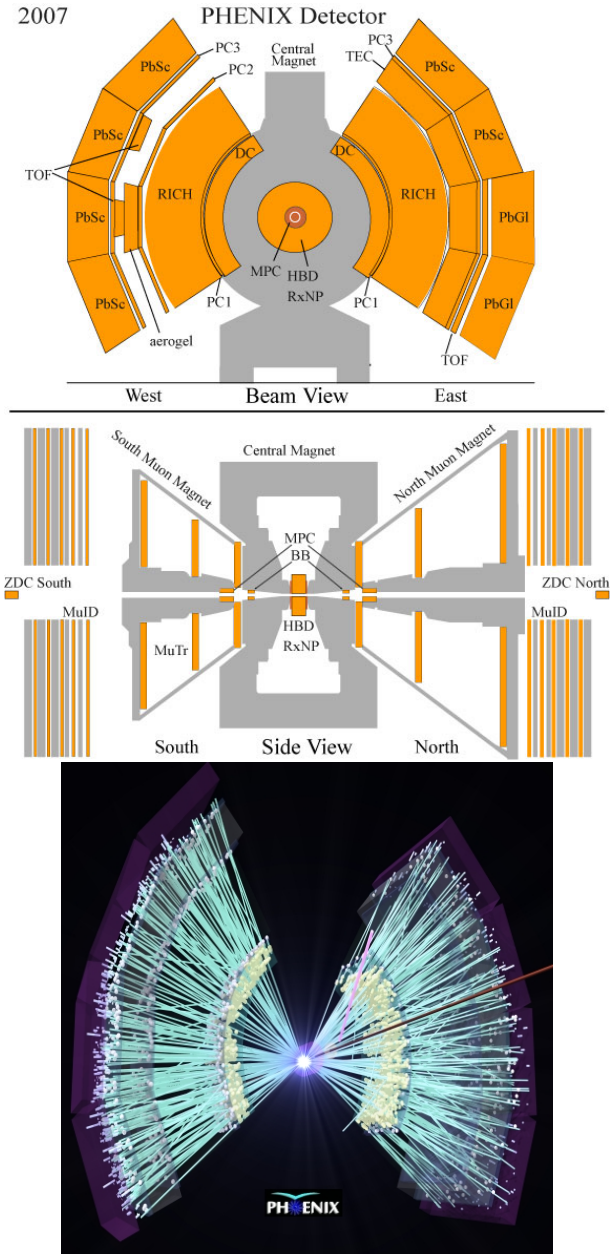

Figure 33. Left: Schematic view of the PHENIX detector before the VTX upgrade [19].

Right: Event display, from [20].

A signature measurement of PHENIX is suppression of high-p_T neutral pions [154], and direct photon production [57]. A comprehensive overview of PHENIX findings by 2005 is found in the white paper[32].

3.2 The STAR Detector

STAR, the Solenoidal Tracker At RHIC, takes its name from its central tracking device, the Time Projection Chamber (TPC), and the solenoidal magnet encasing it, see Figure 34. STAR covers by far the largest solid angle of the RHIC detectors, and has complemented this strength over the years with a host of additional detectors providing excellent particle identification, di-electron and heavy flavor measurement capabilities, forward coverage, calorimetry, and flexible triggering.

A strong magnetic field is needed to bend relativistic charged particles sufficiently to allow precision momentum measurements. In normal operation, the STAR magnet field is at ± 0.5 T (called Full Field (FF) and Reversed Full Field, respectively). In this setting, transverse momentum measurements between about 0.2 and 10 GeV/c are possible with good resolution. Lower energy particles are bent into "loopers", too high momenta result in an almost straight line and momentum (or, indeed, charge) can no longer be reliably measured.

The magnet operates at room temperature (water-cooled) and consumes about 3.5 MW. Apart from the main coils, there are space trim and poletip trim coils to ensure field uniformity. The absolute field is reproducible to within 0.5 Gauss and varies less than 0.1 Gauss/12 hrs. Radial deviations are better than 50 Gauss, azimuthal variations better than 3 Gauss [155]. These requirements were designed to meet estimates of position re-

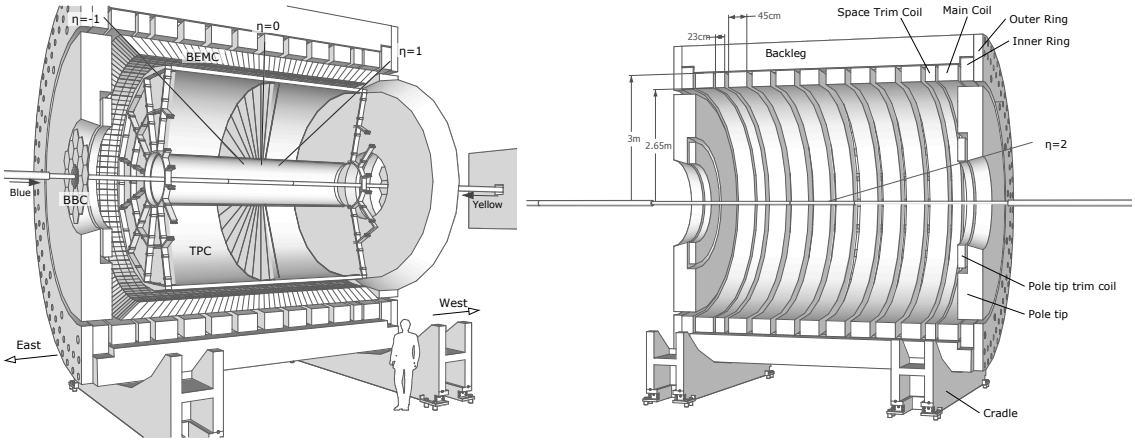

Figure 34. Left: Schematic view of major components of the STAR detector. Right: Detailed cutout of the main magnet system. Both pictures courtesy of Tai Sakuma [21].

construction accuracy and to ensure tracking accuracy for high-energy electrons within 200 μm

The magnet backlegs in Figure 34 are 6.85 m long; the inner diameter of the magnet is 5.27 m, the outer 6.28 m. The whole magnet including the cradles weighs almost 1200 tons and rests on rollers and pistons; it can be moved on rails between the assembly building and the experimental hall. The poletips have their own support structure and can be removed independently.

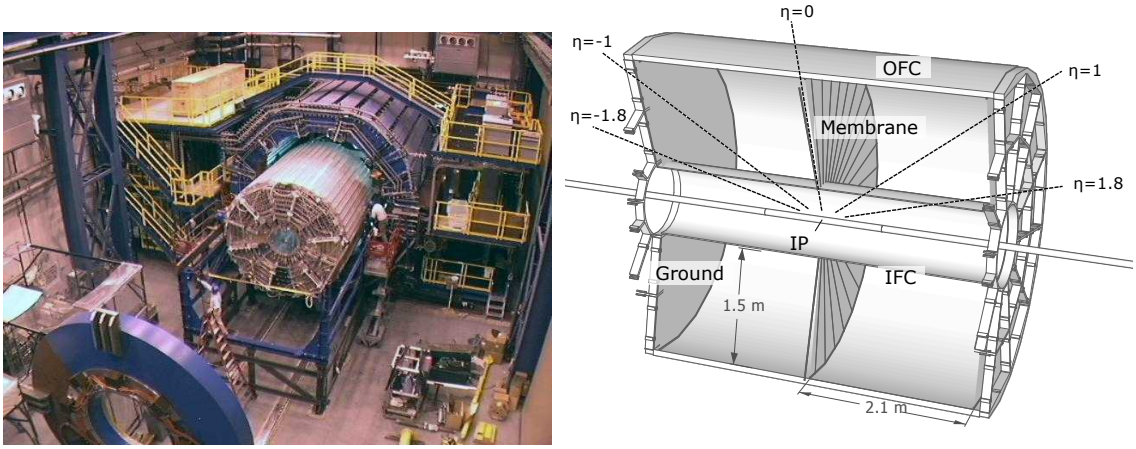

Figure 35. Left: Insertion of the TPC into the detector. The blue structures are the main magnet and the removed poletip [22]. Right: Detailed sketch of the TPC. [21]. Abbreviations: IP - Interaction Point, IFC/OFC - Inner/Outer Field Cage.

3.2.1 The Time Projection Chamber

The TPC is the central element and primary tracking device of the STAR detector [156]. It consists of an 4.2 m long, 4 m high chamber filled with P10 gas (10% methane, 90% argon). The central membrane is held at about 28 kV and separates the chamber into two halves with uniform opposite electric field toward the anodes in the endcaps. Held at 2 mbar, P10 has a high, stable drift velocity of 5.45 cm/μs.

Charged particles traveling through the chamber ionize the detector gas and leave behind a track of electrons. These electrons drift in the electric field toward nearest endcap where they are recorded by readout planes. High stability and uniformity of the electric

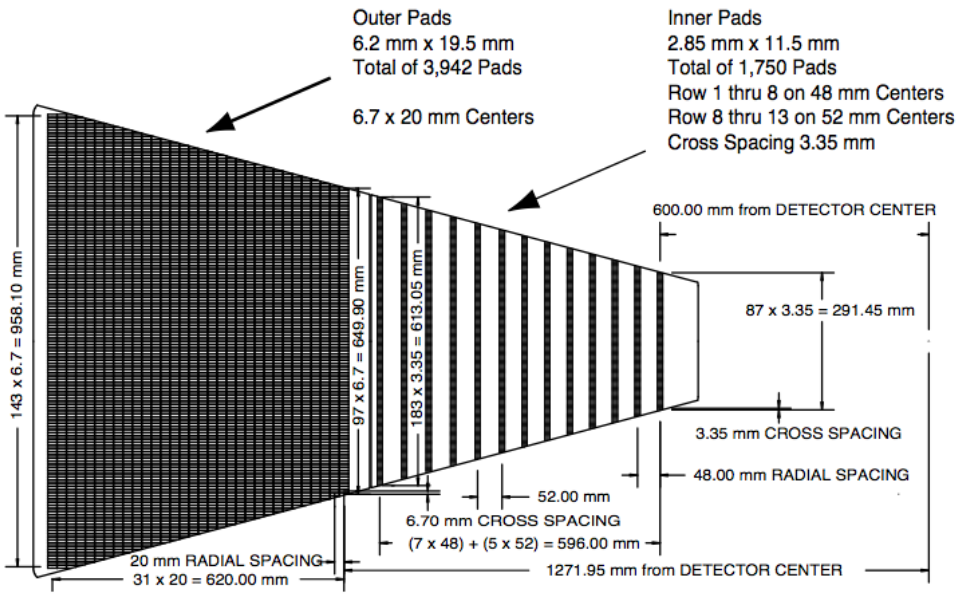

Figure 36. One of the TPC's 24 readout pad planes.

field was a critical design criterion to ensure electron paths longer than 2 m can still be reconstructed with sub-millimeter precision.

Readout planes are based on Multi-wire Proportional Chambers (MWPC); the electrons are amplified by avalanching in a strong field and the resulting signal is measured in readout pads. There are a twelve sectors on each side of the TPC, one of which is shown in Figure 36. The sectors are subdivided into an inner sub-sector consisting of 1750 small pads with wider spacing between rows, and an outer sub-sector with 3942 densely packed larger pads.

A track thus gets recorded as a series of discrete points in the x–y plane perpendicular to the beam axis. Electrons drift at a well-defined velocity in the controlled electric field, and

by dividing data points into discrete time units, so-called time-buckets, the z-dimension can be reconstructed as well. The solenoidal magnetic field bends tracks and allows momentum determination with high precision between $p_T = 0.2 - 10$ GeV/c at full field strength 0.5 T from helix fits to the measured points, called "hits".

Momentum measurement alone is not sufficient to determine the particle species (i.e. its rest mass); this requires an additional dynamic variable such as the relativistic speed β. One of the main advantages a TPC has over silicon trackers is that ionization energy loss ($\mathrm{d}E/\mathrm{d}x$) from collisions with the TPC gas is a function of β, not momentum, over a broad p_T range. Over the length of the TPC, this energy loss is small compared to the total energy of the particle, on the order of a few hundred MeV for a 1 GeV particle, so the helix shape is essentially unaffected. However, the energy loss is measurable as the amount deposited in the readout pad [157, 158, 159]. The dynamic range of the ADC's was chosen to reliably measure energy loss of $p > 200$ MeV particles. The $\mathrm{d}E/\mathrm{d}x$ distribution as a function of momentum is shown in Figure 37. Starting around 1 GeV/c, significant overlap between the bands is visible, but the relativistic rise of $\mathrm{d}E/\mathrm{d}x$ leads to enough separation to make statistical particle identification and separation of pions from non-pions possible in the region considered in this work ($p > 4$ GeV/$c, \log_{10} p > 0.6$). For more details on PID with the TPC, refer to Section 4.3.

3.2.2 Other Detectors

While the present analysis is conducted using only TPC measurements, many more detector subsystems are part of STAR and will be mentioned below briefly:

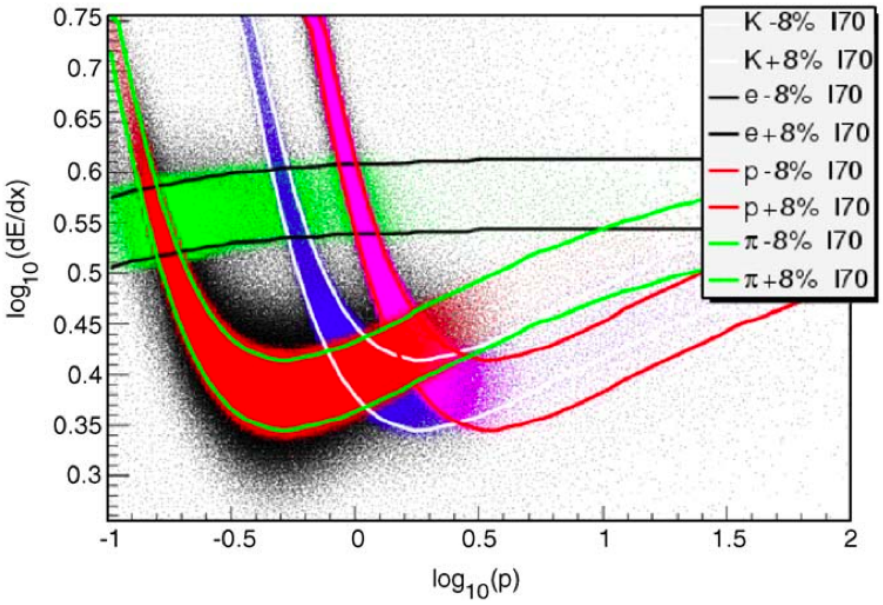

Figure 37. $\mathrm{d}E/\mathrm{d}x$ distribution as a function of momentum [23]. The color bands denote $\pm 1\sigma$ of the $\mathrm{d}E/\mathrm{d}x$ resolution.

3.2.2.1 Forward Time Projection Chambers

For many runs, including 2010, Forward TPCs with similar characteristics as the main TPC extended the tracking range to $2.5 < |\eta| < 4$ [160]. Their measurements were not used for the presented mid-rapidity results.

3.2.2.2 Time of Flight and VPD

To improve and complement particle identification and specifically separation of protons from kaons and pions above $\approx 0.7 - 1$ GeV/c, a large Time Of Flight detector (TOF) was installed starting in 2002 and was fully operational in 2010 [161, 162]. It consists of Multigap Resistive Plate Chambers (MRPCs) and covers $[2\pi \times \pm 0.9]$ in azimuth and pseudorapidity, respectively, with a time resolution of better than 100 ps. Specifically, the TOF is the "stop" detector. The TOF also replaced the Central Trigger Barrel both physically and as the main fast trigger detector for central events, see Section 4.1.1.

Flight time measurement is started by two identical VPDs (Vertex Position Detector) [163] down the beam line on both sides of the TPC 5.6 m away from the center. Each VPD consists of nineteen detector assemblies housing a 0.25 in Pb converter, and a 1 cm thick scintillator. The VPDs also play an important role in triggering and collision vertex position measurement. The main design goal is excellent resolution of the time difference $DeltaT$ between a collision signal in the two VPDs, or equivalently resolution of the vertex position $V_z = c\frac{\Delta T}{2}$. Resolution of a single detector channel is about 100 ps in 200 GeV Au+Au. "Start" time is resolved to 20-30 ps in Au+Au, negligible compared to the TOF

resolution. Vertex resolution, determined as the standard deviation of the difference between VPD and TPC vertex position measurement $V_z^{\mathrm{VPD}} - V_z^{\mathrm{TPC}}$ was found to be about 2.4 cm in Au+Au and 1 cm in pp.

The VPD-TOF combination in its primary PID role cannot be used for the hight-p_T analysis in this work, as its reach is only up to about 3.1 GeV/c.

3.2.2.3 Electromagnetic Calorimeters

Electromagnetic calorimetry is available through the barrel calorimeter (BEMC) [164] in $2\pi \times \pm 1.0$, and on one side extending the forward direction out to $\eta = 2$ with the endcap calorimeter (EEMC) [165]. Their primary use is the detection of electrons, photons, neutral mesons such as π^0 and η, as well as jet reconstruction. The presented di-hadron correlation analysis is an alternative method to study jets and does not rely on calorimetry.

3.2.2.4 More Detectors

Other detectors in STAR that were not present or not used in this analysis include pixel trackers (the decommissioned Silicon Vertex Tracker, SVT [166], the Heavy Flavor Tracker, HFT, currently taking data for the first time [167]), and the Muon Telescope Detector (MTD) [168].

3.2.3 Trigger Systems

After two upgrades, STAR can currently record events at a rate of about 500 Hz. At the same time, collisions occur at a rate of 40 kHz or more, making it vital to quickly select those events deemed "interesting" for saving. This is done using fast detectors and

trigger conditions to quickly estimate properties of an event. Detectors used for triggering are [169, 24]:

Zero-Degree Calorimeter (ZDC): Two identical ZDC's ("East" and "West") are installed at the first bending magnets in the collider line around the interaction point, about 16-18 meters to either side and covering 4 mr in azimuth. They consist of alternating tungsten absorbers and scintillating fibers that route Cherenkov radiation to a PMT [170]. Spatial information in this region is of limited value and the ZDC's are not segmented. Instead they are designed to minimize loss in energy resolution and to withstand high radiation dosage. Charged fragments are mostly taken away by the magnetic fields, neutral collision products and secondaries are negligible in this very forward region. The coincidence of spectator neutrons are used as a minimum bias trigger, as a luminosity and beam monitor tool, as a V_z detector from the timing difference between the two detectors, and as a centrality measure (very central collisions will have few spectator neutrons and vice versa). The energy resolution of test beams at 100 GeV was found to be around 18-22%, the time resolution was estimated to 150 ps and certainly below the design goal of 200 ps.

Beam-Beam Counter (BBC): Two Beam-Beam Counters, located at $z = \pm 3.7$ m from the interaction point and consisting of two layers of tightly packed hexagonal scintillators, play a similar role to the ZDC for pp collisions, where no spectator neutrons

are present. In addition to minimum bias triggering, luminosity control, and vertex position measurement, they are also used as polarimeters in polarized *pp* runs [171].

Vertex Position Detector (VPD): The VPD is the primary minimum bias trigger detector in A+A and d+Au collisions and covered in more detail in Section 3.2.2.2.

TOF and Central Trigger Barrel (CTB): The CTB was a fast detector consisting of 240 scintillator slats covering the region $|\eta| < 1$, used to trigger on high-multiplicity central events with high production of large transverse momentum particles. It has been superseded in this role by the TOF, see Section 3.2.2.2.

Electromagnetic Calorimeters (EEMC and BEMC): The calorimeters, see Section 3.2.2.3, are fast detectors used to select events with large electromagnetic deposition in a small area, such as from jets or direct photons.

Forward Pion Detector (FPD) and Forward Meson Spectrometer (FMS): The FMS is a fast electromagnetic calorimeter in the forward region at $2.5 < \eta < 4$ with full azimuthal acceptance [172, 173]. On the other side of the interaction point, it is complemented by the FPD [174], originally a prototype for the FMS with limited acceptance in ϕ, focused on neutral pion detection. Both provide trigger capabilities.

Triggers can be as simple as "a collision occurred" or as sophisticated as "the event has a high likelihood of having produced an Antihelium-4" nucleus. Many trigger conditions are active at the same time during data acquisition, to select events for recording and sort

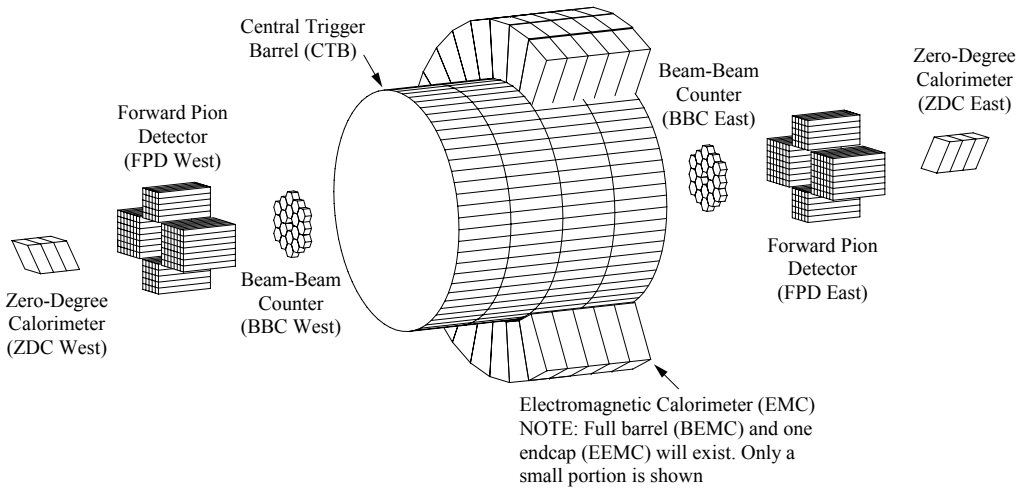

Figure 38. Schematic view of the trigger detectors, in 2004 [24]. EEMC and BEMC have since been completed.

or tag them into data streams. To favor certain triggers over others, so-called prescalers are used to reject for example 49 out of every 50 Minimum Bias events.

Note that the word "trigger" in this context is not to be confused with the usage of the same word throughout most parts of this document. A trigger or trigger condition at the data acquisition level tags an event for further analysis. In the data analysis which is the main focus of this work, the word is used instead to label the leading hadron in a specific event.

CHAPTER 4

ANALYSIS DETAILS

4.1 Data Selection

The analysis is based on Central and Minimum Bias (MB or MinBias) Au+Au data collected by the STAR detector during the 2010 RHIC run period at 200 GeV, and Minimum Bias d+Au data collected in 2008. Additional corrections were made using data from 2004 (Au+Au) and 2003 (d+Au). All selection cuts are summarized in Tables Table I and Table II.

4.1.1 Trigger Conditions

The Minimum Bias trigger attempts to select events solely on the condition "A collision has occurred (close to the TPC center)." In 2003 and 2004, the primary MinBias trigger detector was the ZDC. For Au+Au this meant a coincidence of at least one neutron in both ZDC's and a vertex position within $|z| < 30$ cm of the TPC center. For d+Au, no vertex position cut was imposed, and only a neutron in the Au-going ZDC was required. In 2008 and 2010, the primary MinBias trigger detector is the VPD. For d+Au, still one Au-going neutron ZDC signal is required, and additionally a VPD vertex position within $|z| < 30$. For MB Au+Au, only the condition of a VPD vertex position within $|z| < 30$ is imposed.

	2010 Au+Au	**2008 d+Au**
$\sqrt{s_{\mathrm{NN}}}$	200 GeV	200 GeV
Triggers	MB: VPD $V_z < 30$ cm Central: MB && small ZDC multiplicity && large TOF multiplicity	MB: VPD $V_z < 30$ cm && Au-going ZDC signal
B-Field	Reversed Full Field (-0.5 T)	Reversed Full Field (-0.5 T)
Centrality	0-10%	Minimum Bias
$\lvert V_z \rvert$	< 25 cm	< 25 cm
#Events	154M Central before cuts 3.5M after QA, with all cuts, with a high-p_T particle	46 MB before cuts 106k after QA, with all cuts, with a high-p_T particle

TABLE I

Data set specifics for 200 GeV Au+Au in 2010 and d+Au in 2008

Pseudorapidity	$\|\eta\| < 1$
Distance to primary vertex	`DCA` < 1 cm
Minimum TPC fit points	`NFit` ≥ 20 `NFit` ≥ 30 for identified particles
Used/available fit points ratio	> 0.51

TABLE II

Track quality cuts

The Au+Au Central trigger is designed and optimized to capture the 0-12% most central events. To that end, one selects events with a large number of particles with significant transverse momentum, i.e. within $|\eta| < 1$, and a small number of spectator neutrons in the ZDC. In 2004, the mid-rapidity multiplicity was measured by the CTB, a dedicated trigger detector. In 2010, it was supplanted by the TOF which plays a similar role for triggering. Figure 39 illustrates the MinBias and Central trigger logic in Au+Au. Binary numbers indicate logical conditions that fire above or below a certain threshold. In this example, the MB trigger (top) only requires a minimum count in the ZDC, whereas the Central trigger (bottom) requires additionally a minimum count in the CTB and a

maximum count in the ZDC. The CTB cut is much more restrictive than the upper ZDC limit; in this illustration the effect of the latter is not visible.

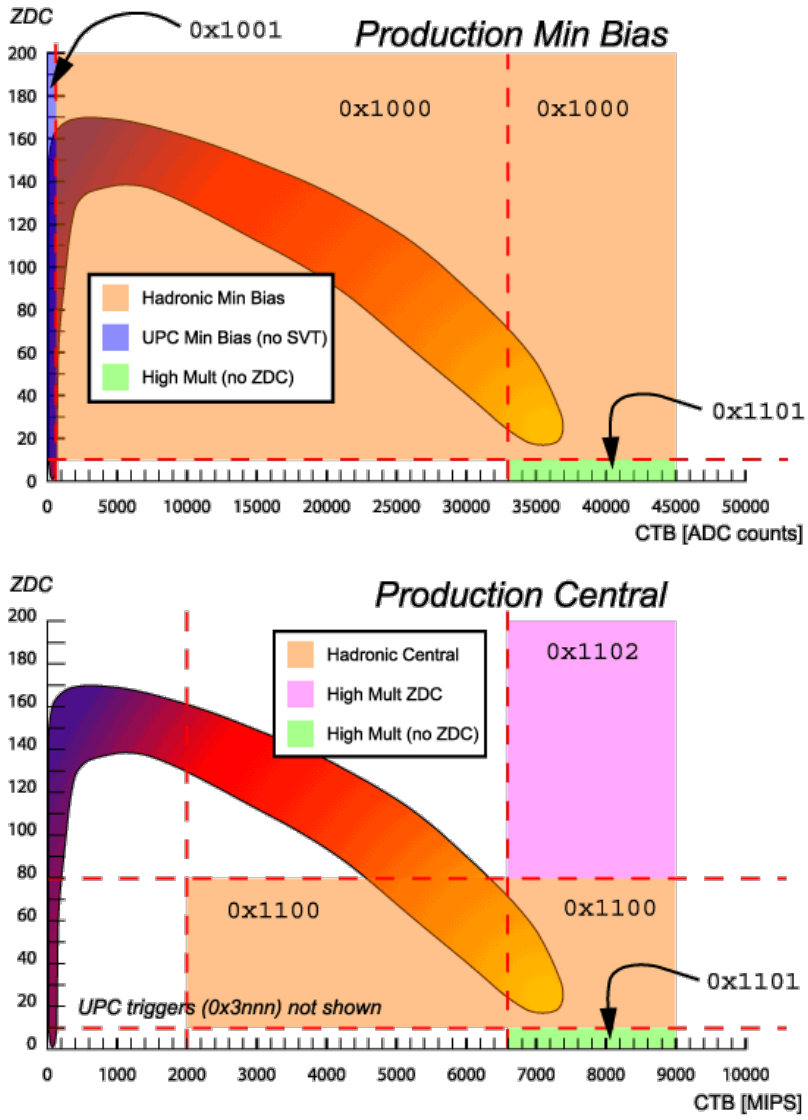

Figure 39. Sketch of event distribution as a function of CTB and ZDC counts [24], given as raw ADC counts or normalized per minimum ionizing particle (MIP). The heat map color scheme indicates event centrality; desired events for the central trigger are found in the bottom right.

4.1.2 Event Reconstruction

The term event properly describes the data recorded when a trigger condition is met. At lower beam energies, events do not always coincide with collisions, but at $\sqrt{s_{\mathrm{NN}}} = 200$ GeV, "event" is often used interchangeably with "collision".

A central collision will create thousands of charged particles, each leaving up to 45 space points in the TPC (or more, in the case of "loopers", low momentum particles that do not reach the edge of the TPC). Other detectors add more data to the event. Event reconstruction is the process of translating raw detector data into an ensemble of collision vertices, charged-particle trajectories ("tracks"), particle energy, energy loss, velocity, momentum, etc.

In the TPC, track reconstruction is in essence a large-scale optimization problem, accomplished with Kalman filter techniques [175]. Starting with short track seeds at the outer edge of the TPC where track density is lowest, the tracks are iteratively extrapolated inwards. In a first pass, so-called *global tracks* are reconstructed without consideration of their presumed origin vertex. Then, a collection of vertices is computed and ranked according to quality parameters such as the number of tracks pointing to it. Vertices can be the main interaction point, a secondary decay vertex, a pile-up vertex, a spurious interaction vertex, or a scattering center. The highest-ranked vertex is assumed to be the primary collision vertex, and tracks that project to within 3 cm (distance of closest approach, `DCA`),

are named *primary tracks*, and refitted in a second pass, now assuming their origin is the primary vertex. Momentum and energy loss are then determined from the fitted helix.

4.1.3 Track Quality

For the analysis, only primary tracks were used. Additional restrictions on reconstructed tracks were imposed:

- In order to reduce the number of secondary decay products, and to increase the accuracy of dynamic variables (p_T, ϕ, η), which are calculated with respect to the primary vertex position, the track `DCA` was capped at 1 cm.
- Including the vertex position, up to 46 measured space points are available to determine a track's helix, but this number of possible points can be reduced due to blind spots in the TPC, or for high-rapidity tracks toward the TPC edges. The actual number of used fit points is lower due to measurement uncertainty, decay, overlap with other tracks, etc. To ensure that tracks are not double-counted, only tracks reconstructed with more than 50% of the available fit points were used. Unidentified tracks also were required to use a minimum of 20 fit points (`NFit`) to improve precision.
- The above are standard quality cuts within STAR in this momentum range. Particle identification is more sensitive to track length in the TPC, and the `NFit` requirement was raised to 30 fit points for identified leading hadrons.

Figure 40 illustrates these cuts.

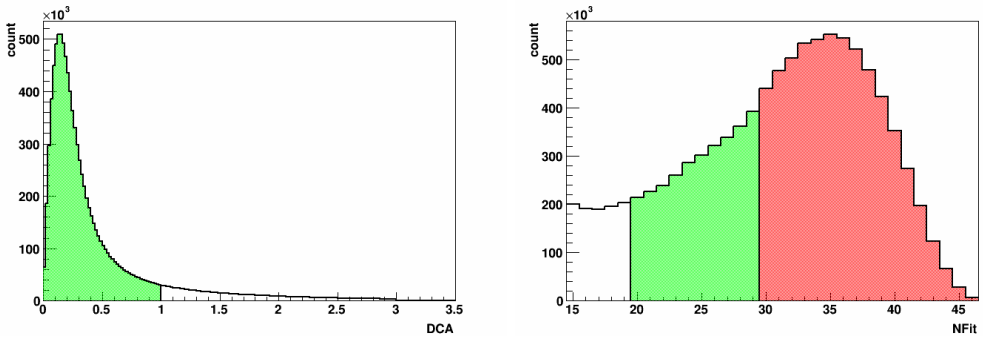

Figure 40. Left: Sample `DCA` distribution in central Au+Au events. Tracks outside the green region were discarded. Right: Sample `NFit` distribution in central Au+Au events. Only tracks in the red region qualify for identification. Tracks outside the green region and red regions were discarded.

4.1.4 Centrality Determination

The impact parameter of a collision is not directly measurable. As an approximation, one uses variables that strongly correlate with it. In STAR, the variable used is Reference Multiplicity (`Refmult`), charged particle multiplicity at mid-rapidity, $|\eta| < 0.5$. `Refmult` counts the number of tracks in this region with standardized quality cuts. Centrality bins are then defined by `Refmult` ranges covering a certain percentage of the total integral. Note that "0-10%" corresponds to the most central events. Figure 41 shows the `Refmult` distribution and centrality cuts for MB and Central Au+Au data in 2010. At low `Refmult` values, the distribution is suppressed by trigger inefficiencies. The centrality cuts are therefore determined by fitting MC Glauber (see Section 2.1.2.3) simulations to this distribution. The cuts shown in Figure 41 are approximate, both `Refmult` and the appropriate cuts are corrected for luminosity-dependent noise-level in the TPC. Simulation, calibration, and cut determination is done centrally in STAR and was not part of this work.

In the Reversed Full Magnetic Field setting, 172M MinBias events and 154M Central events were collected in 2010. The Central selection corresponds to approximately 0-12% centrality. This analysis concentrates on 0-10% most central Au+Au events. The Central dataset increases statistical power by about a factor of eight compared to the central bins in MB. In order to properly represent 0-10% centrality in Au+Au, we use `RefmultCorr`-dependent weights for all events with `RefmultCorr` < 480. `RefmultCorr` ≥ 446 corresponds to 0-5%, the higher value was chosen to best match the tail. The weights were calculated

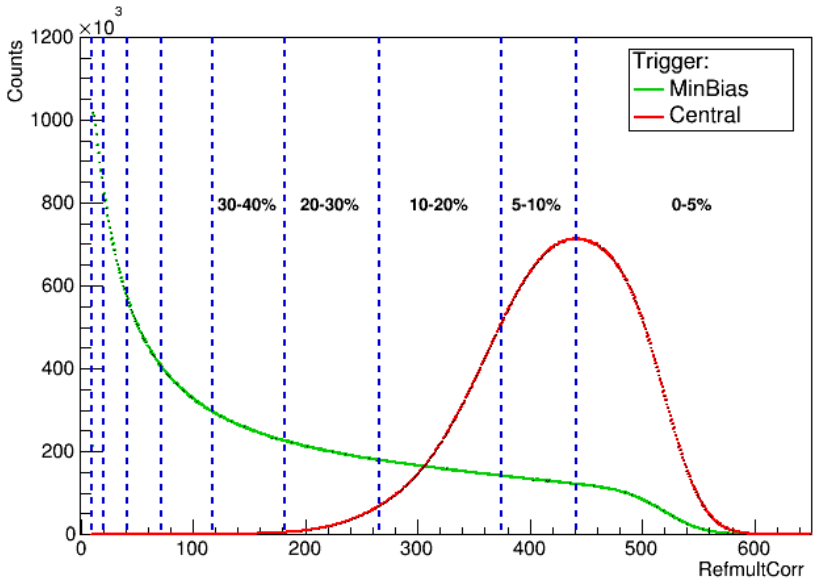

Figure 41. Luminosity-corrected reference multiplicity distribution in 200 GeV Au+Au data in 2010 for MinBias- and Central-Triggered events. The left plot shows approximate cut positions for centrality class determination.

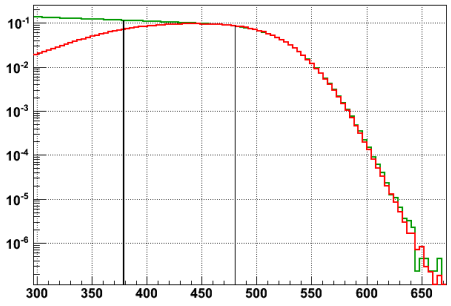

Figure 42. Reference multiplicity distribution for MinBias (green) and Central triggered data (red). The vertical lines indicate the 0-10% cutoff and the chosen matching point.

using the ratio between the MinBias and the Central triggered 2010 data. Figure 42 demonstrates this correction. No centrality cut was placed on the reference d+Au data, and consequently no `RefmultCorr` correction was necessary. (Note that mixed-event binning was not done in terms of reference multiplicity to avoid the inherent bias due to a tighter η cut. Instead, charged particle multiplicity in the fiducial range was used, see Section 4.2.2.)

4.1.5 Dataset QA and Pileup Reduction

For 2008 d+Au, the same data set was used as in a previous paper [113]. In 2010 Au+Au, runs were not used if no EMC data was present (since the vertex finding algorithm in STAR required this data to work properly), if they were rejected by the `Refmult` correction class, or for a few other reasons found during the QA process; 11042049 for example had a magnet crash and corrupted data.

Pileup occurs when during a collision remnants from an earlier collision are still in the detector. In 2010, the high multiplicity led to a high number of pileup events and falsely identified primary vertices. For better primary vertex determination, we chose the highest-ranked vertex whose reconstructed V_z was within 3 cm of the vertex position as determined by the VPD. To further reduce pileup in Au+Au, events were rejected that had an abnormally large number of global tracks compared to the number of primary tracks in the TPC, see Figure 43.

Another issue appears under close inspection of the fit point and `DCA` distribution as a function of ϕ, η, and run day, see Figure 44. This behavior is changing over the course of the run period, see Figure 45.

Effect: For our analysis, `NFit` and `DCA` cuts for associated particles are not significantly impacted. For triggers, the impact is bigger, but the number of affected triggers is still small. To avoid possible problems, especially with n_σ^π, events were nevertheless rejected when potential trigger tracks were found in the problematic region before runday 1043.

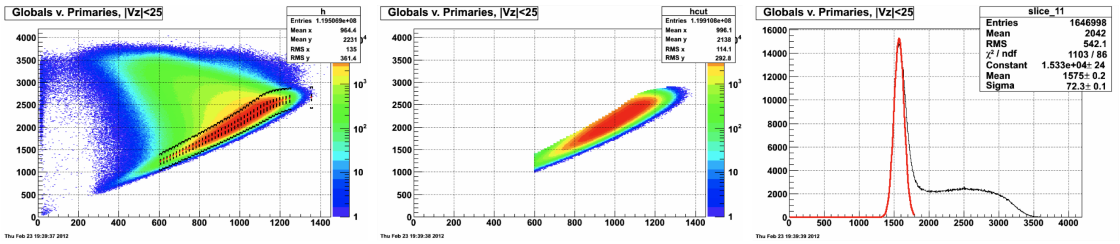

Figure 43. Left: Number of global tracks vs. number of primary tracks in 2010 central Au+Au. $\mu \pm 3\sigma$ of gaussian fits are also shown. Events above $\mu + 3\sigma$ are considered too contaminated by pileup and discarded. Middle: Same plot after the cut. Note that only events with at least 600 primary tracks were kept, which doesn't affect 0-10%. Right: Example fit in a narrow slice. The non-gaussian part exhibits the multiplicity distribution shape expected from pileup.

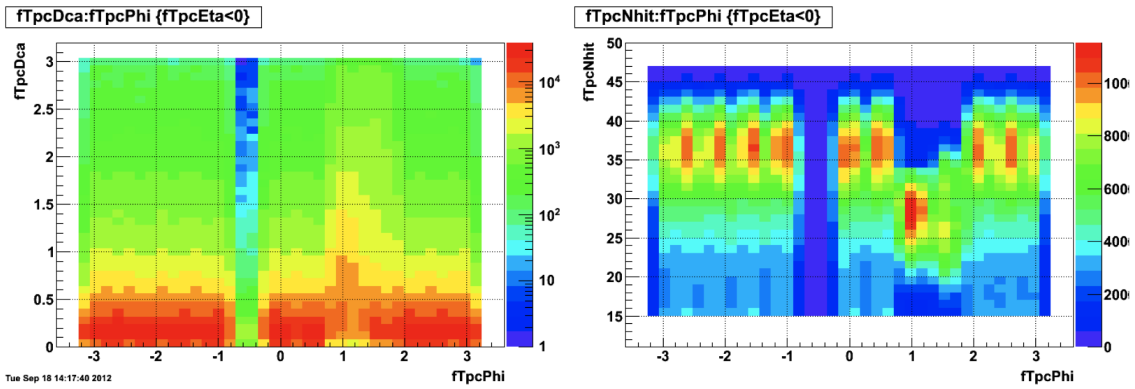

Figure 44. Left: For run day 1035, $\eta < 0$, $p_T > 1.5\text{GeV}/c$: `DCA` as a function of ϕ. The effect of the (known) dead sector is visible around $\phi \approx -0.7$. More worrisome is the severe distortion around $\phi \approx 1.1$. Right: The likely cause, a shortened distribution of `NFit` in the same area. The sector in question has diminished efficiency.

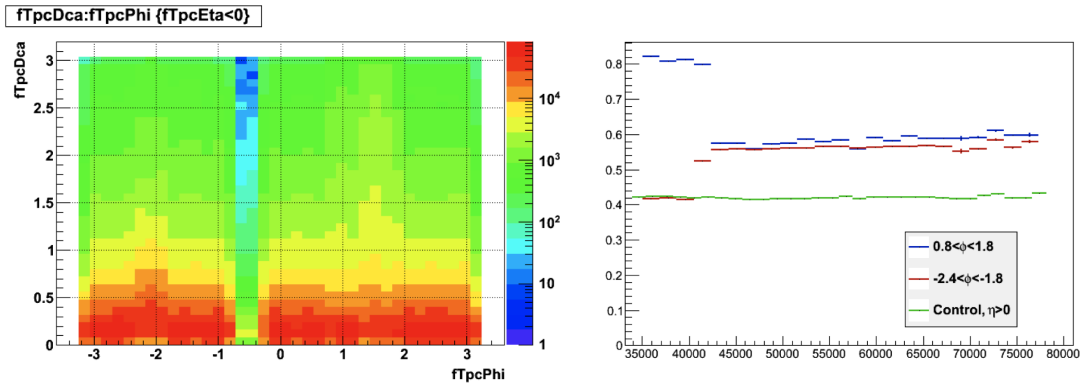

Figure 45. Left: For run day 1050, $\eta < 0$, $p_T > 1.5\text{GeV}/c$: The `DCA` at $\phi \approx 1.1$ is slightly improved, and its position has slightly shifted. However, a second problematic region has appeared at $\phi \approx -2$. Right: Comparison of average `DCA` in the two ϕ regions and $\eta < 0$ as a function of run number, compared to positive η. The problem at negative ϕ appears at the same time at which the one at positive ϕ is alleviated slightly. The change appears after runday 1043, which has no data and was likely an access day.

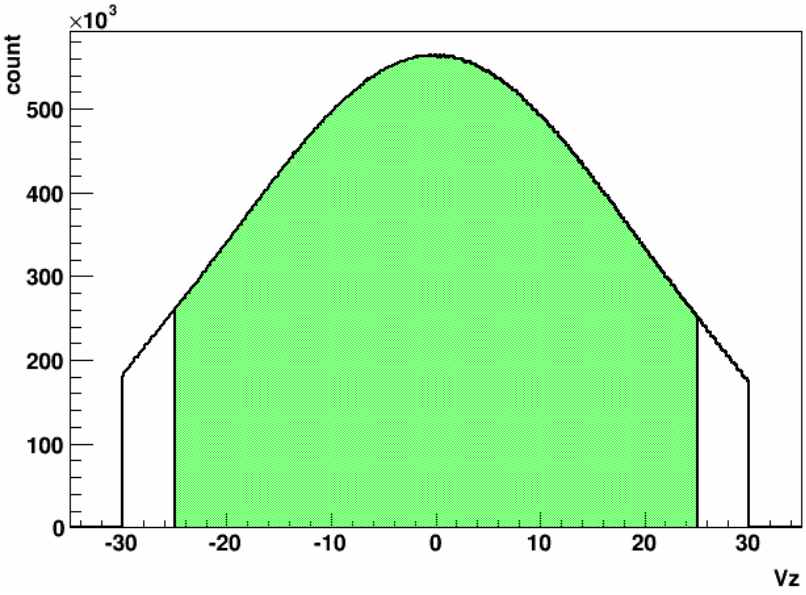

Figure 46. V_z distribution of central Au+Au events. Events outside the green region were discarded.

4.1.6 Primary Vertex Position

In addition to the requirement that the z component of reconstructed primary vertices V_z be within 3 cm of the position determined by the VPD detector, events were also constrained to be within 25 cm of the TPC center (instead of 30 as per the Central and MB trigger), where tracking performance is best. Figure 46 illustrates the cut.

4.2 Dihadron Correlation

Correlation functions in this work describe the number of charged associated particles within $1.5 < p_T^{\mathrm{assc}} < 4$ GeV/c as a function of relative azimuth ($\Delta\phi = \phi^{\mathrm{assc}} - \phi^{\mathrm{trig}}$) and relative pseudorapidity ($\Delta\eta = \eta^{\mathrm{assc}} - \eta^{\mathrm{trig}}$) with respect to a $4 < p_T^{\mathrm{assc}} < 5$ GeV/c trigger. Trigger particles are required to be the leading particle of the event; events with particles above 5 GeV/c are discarded, and if multiple particles fulfill the p_T^{trig} cut, only the highest one is used.

The correlation function can be written as

$$\frac{1}{N_{\mathrm{trig}}}\frac{\mathrm{d}^2N}{\mathrm{d}\Delta\phi\mathrm{d}\Delta\eta} = \frac{1}{w_{\mathrm{Refmult}}}\frac{1}{\epsilon(\phi,\eta,\Delta\phi,\Delta\eta,p_T,\mathrm{Refmult})}\frac{\mathrm{d}^2N^{\mathrm{raw}}}{N_{\mathrm{trig}}\mathrm{d}\Delta\phi\mathrm{d}\Delta\eta}. \tag{4.1}$$

Where N^{raw} labels the yield (charged particle count) found in the TPC, and N the fully corrected yield. It is normalized per trigger, every track is weighted for correct `Refmult` distribution (w_{Refmult}, see Section 4.1.4), and corrected for single particle efficiency and pair acceptance ($\epsilon(\dots)$, see Sections 4.2.1, 4.2.2). Note that w_{Refmult} is always equal to unity for d+Au and high multiplicity Au+Au above a `Refmult` of 480. Correlation functions are subdivided by the trigger's energy loss value, see Section 4.3.

4.2.1 Tracking Efficiency

The TPC cannot reconstruct every charged particle with 100% efficiency. The probability of successfully reconstructing a track is dependent on the geometrical setup, multiplicity, support structures and other material inside the gas volume, electronics performance, mo-

mentum of the track, quality cuts, etc. To account for this inefficiency, a small number (usually around 5% of total multiplicity) of simulated, i.e. "known", tracks are embedded into real events and the new event is reconstructed using the same tracking software as for real events. Monte Carlo tracks are created, and their interaction with the detector and detector response is simulated with GEANT-3 [176, 177]. Efficiency can then be calculated as the ratio of reconstructed to injected tracks, using quality cuts and dynamic variables as desired.

This work utilizes an η–p_T–centrality-dependent parameterization [12] for data from 2003 and 2004, shown in Figure 47.

To account for geometry and track reconstruction differences between 2003/2004 and 2008/2010, respectively, a data-driven approach was used. For all centrality classes, $\phi - \eta$-dependent "translation" maps (shown in Figure 48) between central triggered 2004/2010 Au+Au and minimum bias 2003/2008 d+Au data are constructed using the quality cuts for associated tracks. By weighting every associated track according to these maps, the geometry and acceptance differences between the two run periods are corrected. In d+Au, the MinBias trigger definition changed significantly between 2003 and 2008. Therefore, a 3 GeV/c particle was required to be present in every event used for the translation maps, thus equalizing the resulting `Refmult` distributions.

Single particle efficiency correction is applied by using inverse efficiency of the associated particle as a weight while filling correlation histograms with a $\Delta\phi$–$\Delta\eta$ pair. Overall normalization is per trigger particle, so efficiency correction only concerns associated tracks.

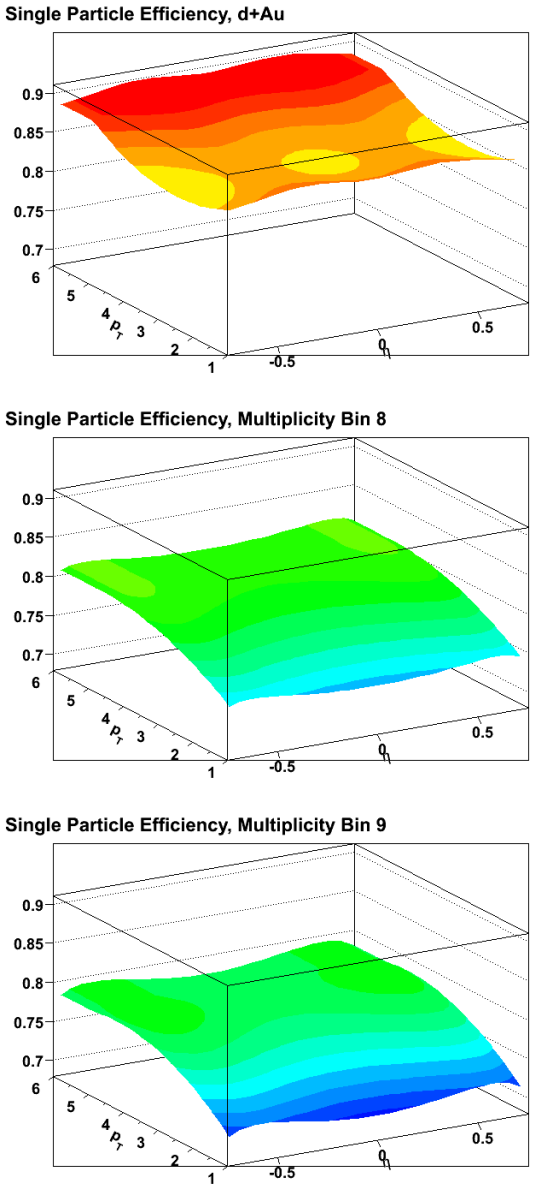

Figure 47. Parameterized efficiency from fits to embedding data in 2003 (d+Au, top), and 2004 (Au+Au, middle and bottom) from Mark Horner [12]. The middle panel corresponds to 5-10% most central data, the bottom one to 0-5%. Applied after geometry translation.

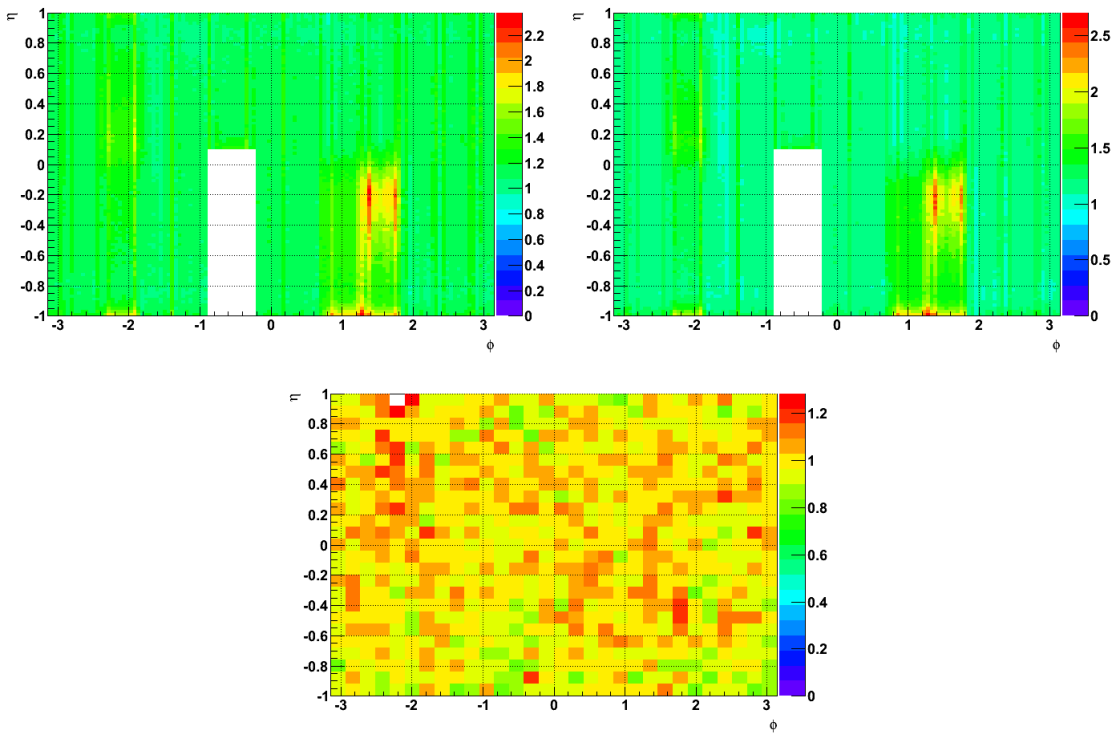

Figure 48. Ratio of all tracks satisfying cuts for associated tracks in 2004 over 2010 (top left: 5-10% most central, top right: 0-5% most central), and in 2003 over 2008 (bottom). Regions of extreme change have been excluded (a masked dead sector in 2010; one small region in 2008). The lower statistics in d+Au require more coarse binning. One can estimate with the naked eye that overall efficiency dropped by about 20% between Run 04 and Run 10, whereas d+Au efficiency stayed mostly unchanged.

This efficiency correction is averaged in ϕ, and smoothed in η, so substructures remain. Detector effects on the trigger distribution are also not corrected yet. Both of these issues are addressed using the mixed-event technique in Section 4.2.2.

4.2.2 Pair Acceptance

An immediate need for additional corrections arises from the $|\eta| < 1$ cut applied to both trigger and associated tracks. As Figure 49 demonstrates, the difference between two flat random variables with this cut leads to a triangle shape due to the geometric constraint. In this idealized case, the correction would be a simple division by a triangle function normalized to 1 at $\Delta\eta = 0$, where pair acceptance is not affected by cuts. In practice, this is complicated by the aforementioned remaining substructures in ϕ, η, and the non-correction of the trigger distribution. Single particle efficiency correction is constrained by the computationally expensive Monte Carlo simulation, but even with unlimited resources, dead regions in the TPC exist where efficiency is zero and thus not correctable. Using a triangle also assumes that the η distribution of particles is perfectly flat (which is however approximately true for $|\eta| < 1$ and $p_T > 1.5$ GeV/c).

A more elegant way to correct for geometric and remaining detector effects is the data-driven *event mixing* technique [178]. A background correlation is created using the exact same method as the original signal, only using triggers from a different, but geometrically similar, event than associated particles. Thus any truly physical correlation is destroyed and only geometrical and acceptance effects remain. Every real trigger is mixed with exactly 100 distinct events, avoiding the original event in the process. To mimic the

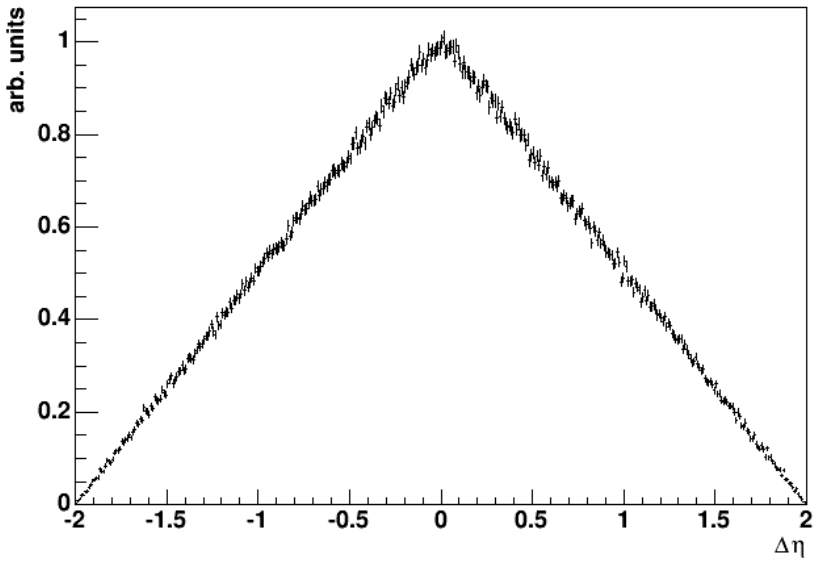

Figure 49. Distribution of $\Delta\eta = \eta_1 - \eta_2$ for randomly generated $\eta_{1,2} \in [-1, 1]$, normalized to 1 at $\Delta\eta = 0$.

geometric situation in an event as closely as possible, the mixing event was selected to come from the same 2.5 mm wide V_z bin as the original event. Geometrical acceptance is also sensitive to occupancy, the percentage of pads in the TPC detecting a signal. `Refmult` is not a good measure of occupancy since the different η cut introduces an artificial bias. Au+Au events were therefore subdivided into five multiplicity bins, where instead of `Refmult` the actual number of tracks satisfying quality cuts was used. These bins are not of equal size but rather balanced to ensure similar bin fill. Mixed events are also coming from a continuous subset of the run period, further minimizing differences between events. Where applicable, individual backgrounds were created for the various trigger-associate charge combinations needed for split track correction (cf. Section 4.2.3).

Normalization: Background distributions from the individual multiplicity and V_z bins are combined with appropriate weights before the signal is corrected. The signal is divided by the normalized background. Normalization should be such that the background is equal to unity at the point of maximal pair acceptance. Without single particle efficiency correction, this would be the maximum of the histogram. The ϕ-averaged efficiency correction however requires that unity be attained for the $\Delta\phi$-averaged maximum. The normalization constant is therefore obtained as the value at or around $\Delta\eta = 0$ in a $\Delta\eta$ projection of the background. As a positive side effect of this average, the associated systematic uncertainty is better than 1% in d+Au and negligible in Au+Au.

Correct choice of the normalization constant is especially important in 2010 where the dead sector and other TPC asymmetries lead to significant substructures such as a "bump"

at small $\Delta\phi$–$\Delta\eta$, as evidenced in Figure 50 and Figure 52. The distinctive "ripples" in $\Delta\phi$ in Figure 50 are an effect of the twelve sector boundaries of the TPC. The bump can be understood by imagining a simplified TPC with 11 perfect sectors and one that is dead. Drawing random ϕ pairs from this distribution and calculating their difference $\Delta\phi$ simulates creation of a di-hadron correlation only influenced by acceptance. For most $\Delta\phi$ values, this will result in an overall average yield reduction of 1/12. However, since a "trigger" was found, the acceptance close to it, corresponding to $\Delta\phi \approx 0$, is at worst reduced by half, if the trigger is right on the edge of the dead sector. A simulation of this situation with a simple toy Monte Carlo is shown below in Figure 53. The bump is clearly visible, in this ideal scenario a triangle twice as wide as the dead sector.

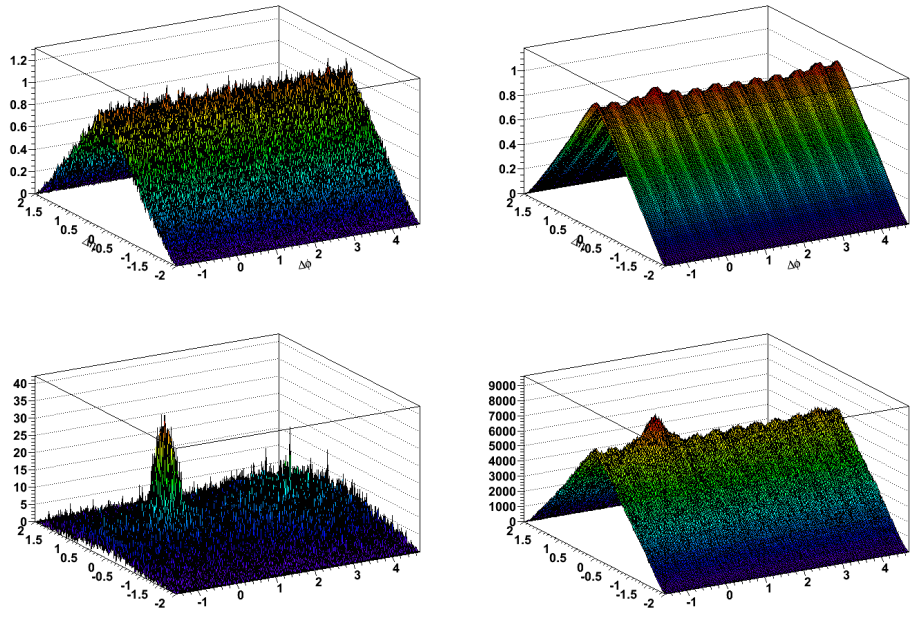

Figure 50. Top row: Unrebinned mixed background for unidentified triggers. Bottom row: Unrebinned correlation histogram for comparison. Left d+Au, right Au+Au.

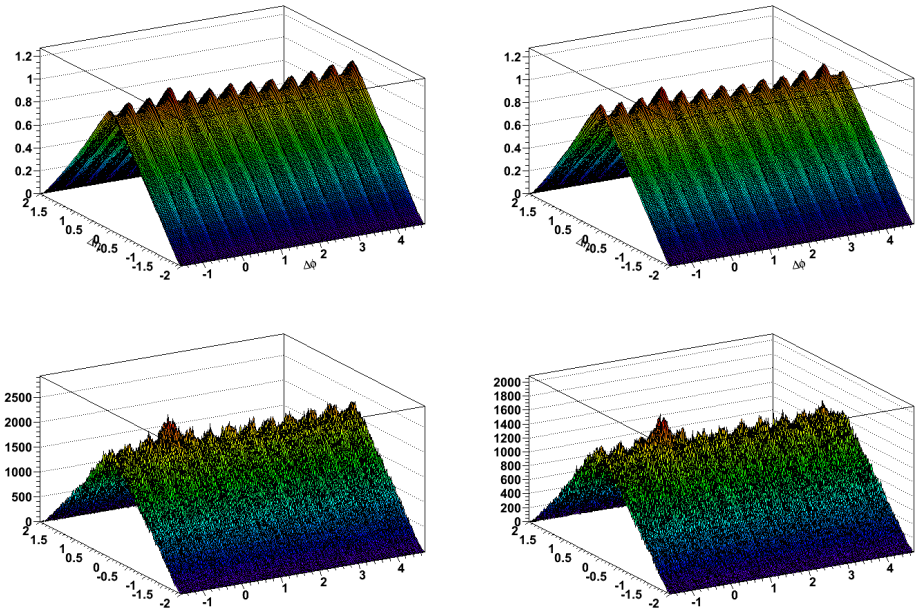

Figure 51. Top row: Unrebinned mixed background for unidentified triggers. Bottom row: Unrebinned correlation histogram for comparison. Au+Au; charge combination: left "++" , right "−−"

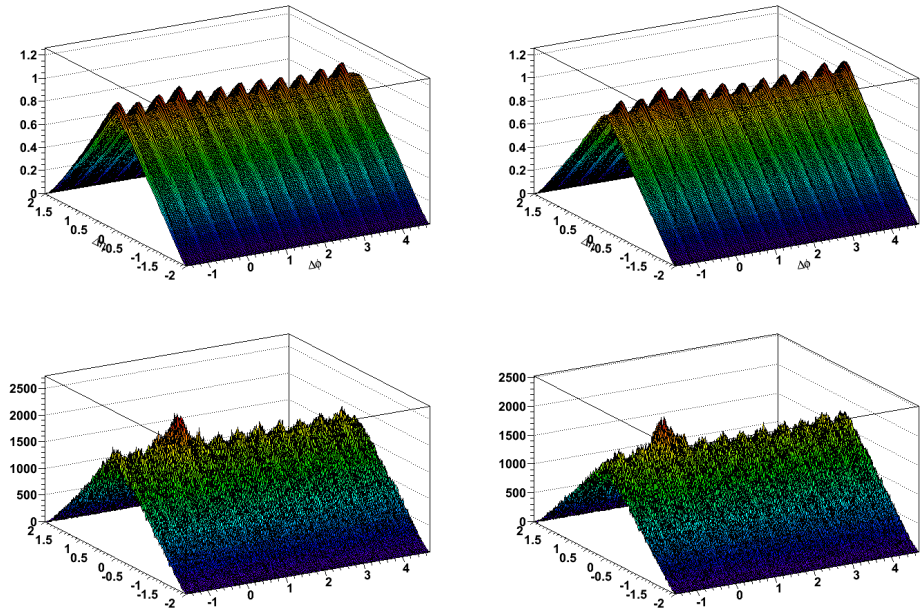

Figure 52. Top row: Unrebinned mixed background for unidentified triggers. Bottom row: Unrebinned correlation histogram for comparison. Au+Au; charge combination: left "+−"' , right "−+"

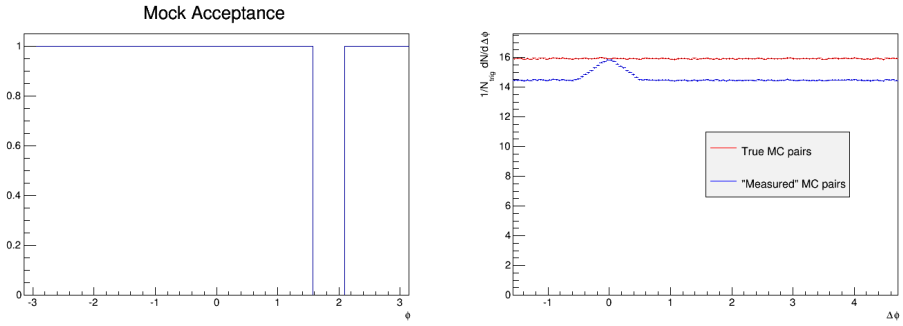

Figure 53. Simple simulation result to illustrate the source of the bump in the mixed background. Left: Acceptance of an idealized one-dimensional detector with one dead sector. Right: Drawing pairs from this distribution leads to an overall decrease compared to "real" data, except close to 0. If the first trigger were in the dead sector, the "event" would have been rejected.

4.2.3 Track Splitting

Two effects related to reconstruction can artificially deplete the correlation at small relative angles:

Track *merging* occurs when the trigger particle and a nearby associated track have the same helicity and similar p_T, ϕ, and η. If they share a significant amount of hits, they can be reconstructed as only one track. Track *splitting* occurs when an intersected track is reconstructed as two shorter tracks, both of which are then often discarded because they no longer satisfy quality cuts.

In general, both effects are handled by the tracking efficiency correction. However, a trigger splitting a track or merging with a track can of course not be captured in mixed events, leading to narrow "holes" of severely depleted yield at small relative angles. Since the trigger p_T range used in this analysis is well above most associated tracks, the effect of track merging is negligible. Track splitting is corrected using the symmetry of the correlation:

The helicity of the involved tracks makes for four different cases where the depletion is slightly offset from the origin. The correlation signal and background are therefore constructed individually for positive/negative triggers and positive/negative associates, with individual mixed background corrections. Figure 55 shows the four combinations before correction for unidentified triggers.

For qualitative comparison, the corresponding "before" plots from [25] with identical associate range and $p_T^{\text{trig}} = 3 - 6\text{GeV}/c$ are shown in Figure 54. As seen in panels a) and d), track merging was more of an issue due to the lower trigger p_T.

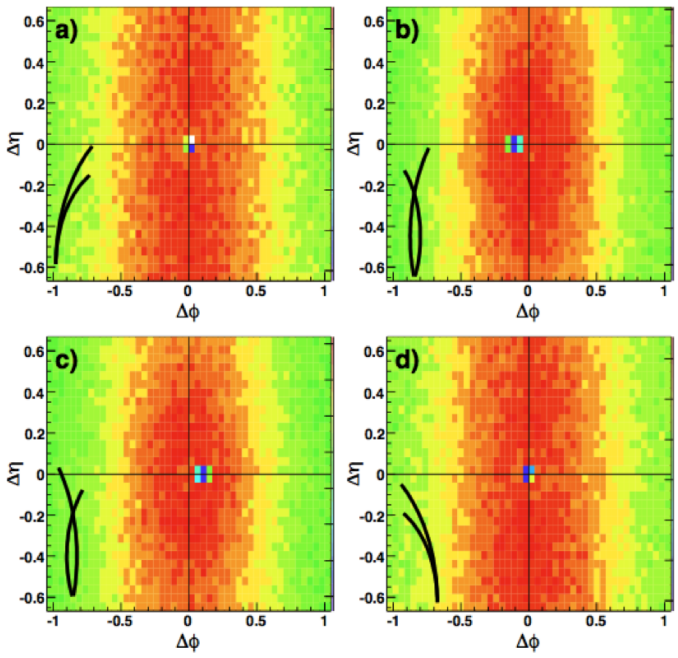

Figure 54. Track merging/splitting illustration from [25].

4.2.3.1 Correction

Since the correlation signal is expected to be symmetrical around $\Delta\phi$=0, the ratio due to the dip in one case is reflected and can be used to correct the other, thus preserving the

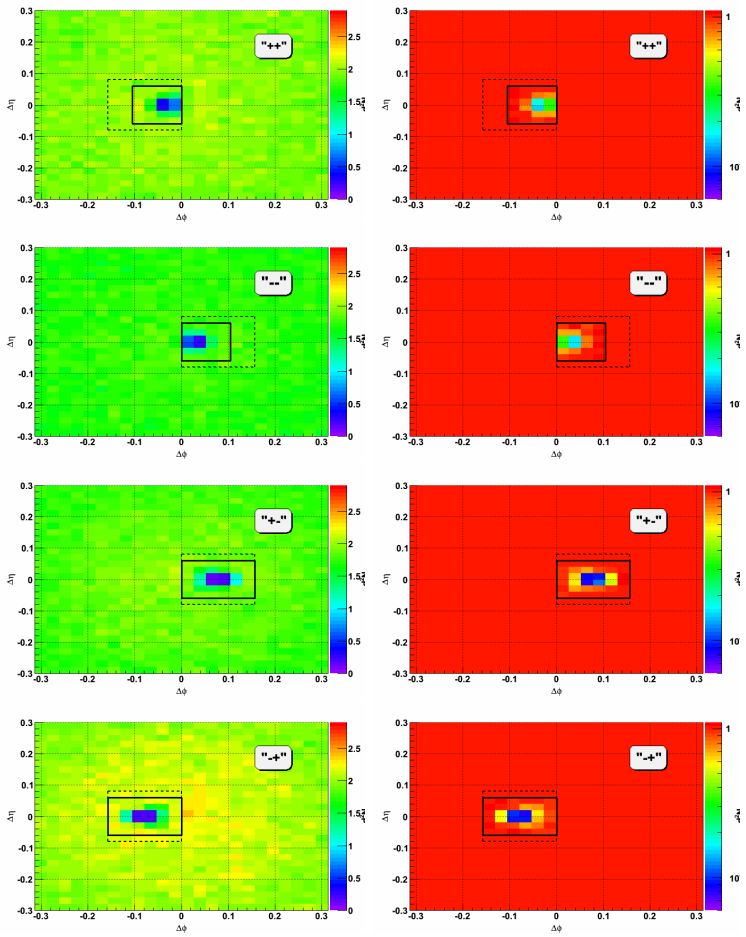

Figure 55. Left: For unidentified triggers, effect of track splitting before correction. Right: Ratio of the correction region with its mirrored counterpart. The log scale serves to better differentiate between small and large depletion. The solid black line indicates the region where correction will be applied; the dashed line represents a single bin in the rebinned final histograms to give a sense of proportion. Shown are correlations with unidentified triggers.

statistics; i.e., the like-sign combination "−−" is used to correct "++", and vice versa, the unlike-sign case is handled the same way. Where the ratio is too small, the bin content is instead replaced by its mirror partner. In that case, the bin error needs to be set to $\sqrt{3}$ times the mirror partner's error (when integrating over the histo, this results in the correct $\sigma_{\Sigma}^2 = 3\sigma^2 + \sigma^2$). That gives a natural cutoff point: If the bin would need to be scaled up by more than $\sqrt{3}$, it is replaced instead. The result is shown in Figure 56. For the final histograms, the charge combinations are recombined in appropriate proportions.

To evaluate systematic uncertainty, the split region size was varied as shown in Figure 57.

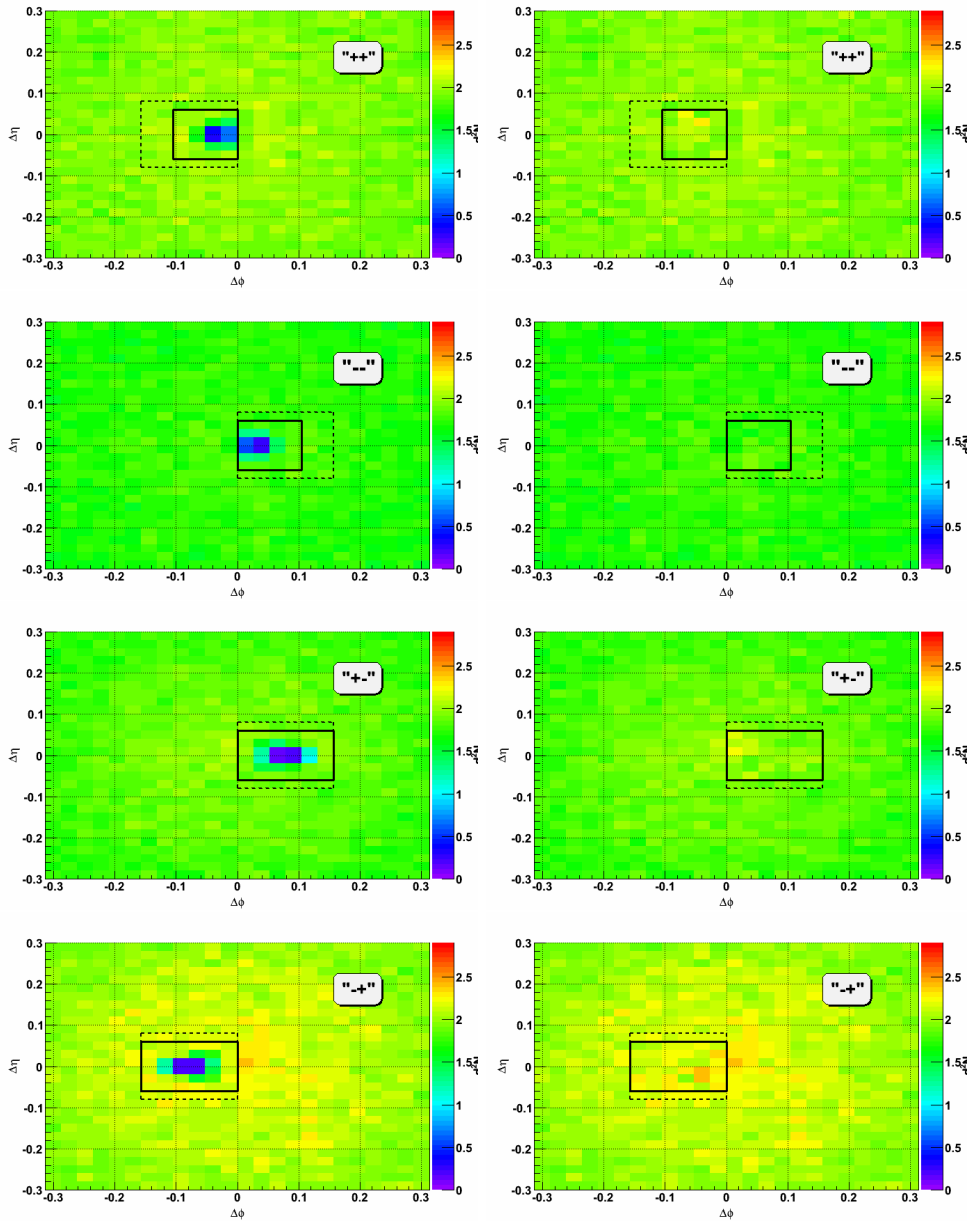

Figure 56. Left: Same as in Figure 55. Right: Result of split track correction.

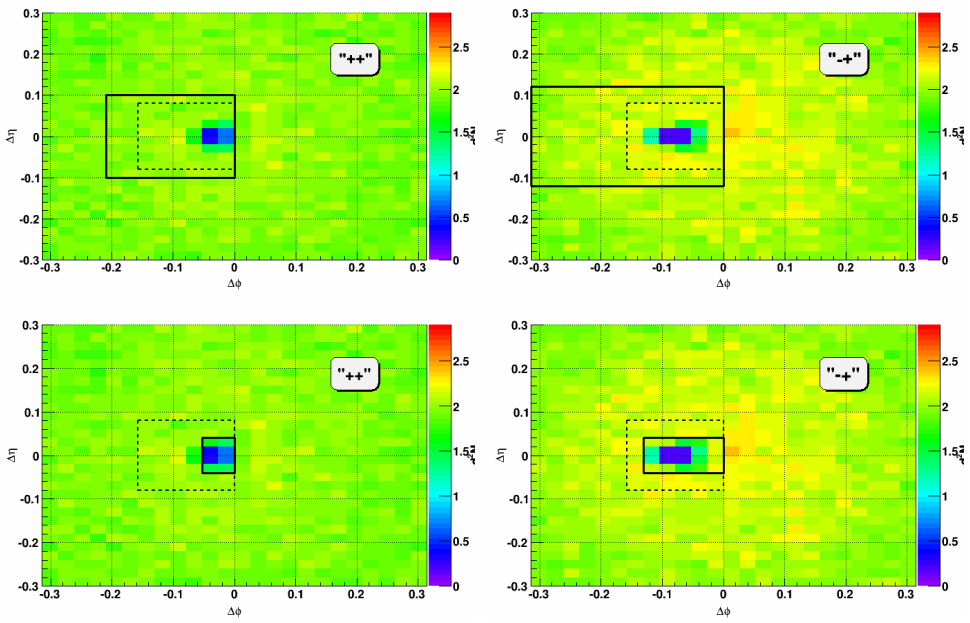

Figure 57. Different sizes of the correction region for systematics for two charge combinations. The other two combinations use identical regions mirrored at $\Delta\phi = 0$.

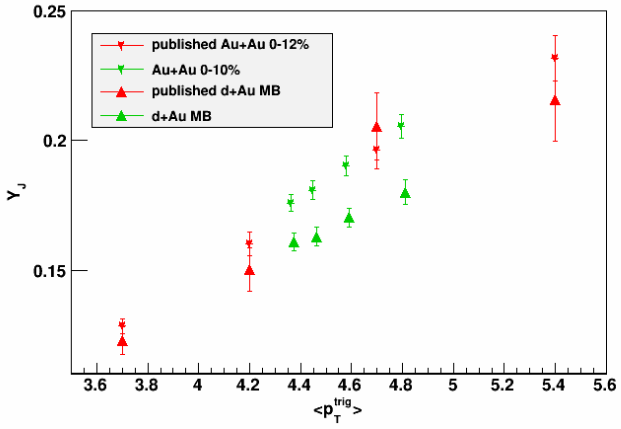

Figure 58. Jet-like yield measured in [25] in red compared to values found in this study (statistical errors only). The left-most green data points at $\left\langle p_T^{\text{trig}} \right\rangle \approx 4.35$ correspond to the cut used in this work; the other values were added to explore trigger-p_T dependence.

4.2.4 Cross-check–Yield Comparison to Published Values

Before trigger identification, the analysis method used here should be consistent with values that were found in [25] with a different, lower statistics, data set. Figure 58 shows the jet-like yield comparison for unidentified ("inclusive") triggers. Details about jet-like yield extraction are described in Section 5.1; it follows the procedure in the reference. Additional points were added to demonstrate the trigger-p_T dependence.

4.3 Trigger PID Separation

4.3.1 Particle Identification

Particle identification is done using the relativistic rise of energy loss ($\mathrm{d}E/\mathrm{d}x$), normalized in the n_σ^π variable [8, 67, 23],

$$n_\sigma^X = \ln\left(\frac{\mathrm{d}E/\mathrm{d}x}{B_X}\right)\frac{1}{\sigma_X}, \tag{4.2}$$

where B_X is the theoretical expectation for $\mathrm{d}E/\mathrm{d}x$ for particle species X, and σ_X is the $\mathrm{d}E/\mathrm{d}x$ resolution of the TPC. This reparameterization serves multiple purposes:

- Use of the logarithm reshapes the individual particle distributions close to Gaussian;
- shift to the expectation value B_X reduces p_T dependence, especially for species X, which will lead to Gaussian shapes at or close to $n_\sigma^X = 0$;
- normalization by the resolution leads to the width of this Gaussian to be close to 1.

The expected value of n_σ^X for protons and kaons depends on detector details and is determined using MC simulations and initial calibration on Minimum Bias data. For our purposes, these expectations were determined by finding the maximum of $n_\sigma^\pi - n_\sigma^P$ and $n_\sigma^\pi - n_\sigma^K$ respectively. As shown in Figure 59, this expectation value shows some η dependence, but is symmetric around 0.

Since initial calibration in STAR is done for minimum bias data without a p_T cut and with different quality cuts, additional calibration is necessary: n_σ^π is fitted with three

gaussians in two transverse momentum and five $|\eta|$ bins. The widths are fixed to be the same (but not to a specific value), they reflect the $\mathrm{d}E/\mathrm{d}x$ resolution, and therefore (in the relativistic rise regime) there is no reason to expect different resolution for pions, kaons, and protons. By construction, in case of ideal calibration, the expected width is 1. Initial calibration was carried out for the minimum bias sample. Resolution deteriorates slightly with high occupancy, i.e. in central events, however the higher quality cuts used here may improve resolution; the width can therefore no longer be assumed to be 1 and is left free.

The pion and proton centroid positions are free, and the kaon position is at the theory-predicted relative distance between the two (the variations of the relative kaon position is a significant source of uncertainty for the protons, but affects very minimally pions that are about 2σ away).

Constraints summary:

- The width is locked to be identical for all three gaussians.
- The relative kaon separation from pions and protons scales with expectations from the Bethe-Bloch curves.
- Fits are done between $n_\sigma^\pi = -5$ and 2.2 to minimize the influence of electrons and low n_σ^π noise.
- Kaon yield is a dependent variable such that the fit function integrates to unity.

Following the technique of fixing the relative kaon yield by K_0^S measurements, we replicated the originally published P/π result and switched to directly fixing P/π using

Dataset	p_T [GeV/c]	**published P/π**	**Correction**	**"raw" P/π**
Au+Au	$4.0 - 4.5$	0.644	$1.04 * 0.964/1.018 = 0.985$	0.634
Au+Au	$4.5 - 5.0$	0.558	$1.04 * 0.943/1.015 = 0.967$	0.539
d+Au	$4.0 - 4.5$	0.450	$1.04 * 0.989/1.018 = 1.010$	0.454
d+Au	$4.5 - 5.0$	0.382	$1.04 * 0.976/1.015 = 1.000$	0.382

TABLE III

Published P and π yields, P/π ratio and correction factors.

values from [179, 98] instead for computational ease, because that quantity is used later for the derived "pure proton" values.

The published fully corrected P/π ratio were converted into raw P/π equivalent by removing about 4% pion feed-down correction applied in [179, 98] for pion yield, and adjusting for differences in feed-down contributions due to different `DCA` cuts between the analyses (about a 1-6% effect). The difference between published dN/dy ratios and the dN/dη ratios used here led to another 1.5-1.8% correction factor. The effects are partially off-setting, as seen in Table III

Details of the particle identification fits are summarized in Table IV, Table V, Table VI, Table VII, and Figure 61, Figure 62. Note that to better illustrate pion from non-pion separation, the sum of proton and kaon gaussian is shown in the figures, not the actual

individual gaussians used for fitting. C_π designates the average pion position, C_P the proton centroid, i.e. the distance to C_π. C_K/C_P is the fixed relative kaon centroid. Figure 63 and Figure 64 show the centroids, relative yields and σ for both p_T bins.

Properly reassembled over η and p_T, the fitting procedure leads to the π/non-π compositions illustrated in Figure 60. Besides the "nominal" version of the fit, with four free parameters, variations included freeing all yields (three additional parameters, seven total), varying the pion centroid position within fitting uncertainty, and varying the P/π ratio within published uncertainty; and the results are included in systematic error evaluation, see Section 4.3.2. Specifically, freeing all yields leads to less variation than forcing the full systematic range of P/π; the fit results in Figure 60 are compared with free fits where all three yields were independent parameters.

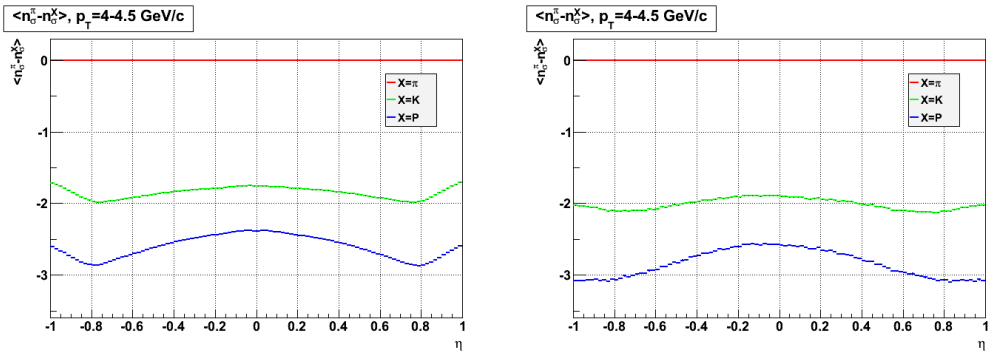

Figure 59. Profile of theoretical expectation for proton and Kaon separation from pions, as a function of pseudorapidity and $p_T = 4 - 4.5\text{GeV}/c$ in Au+Au (left) and d+Au (right).

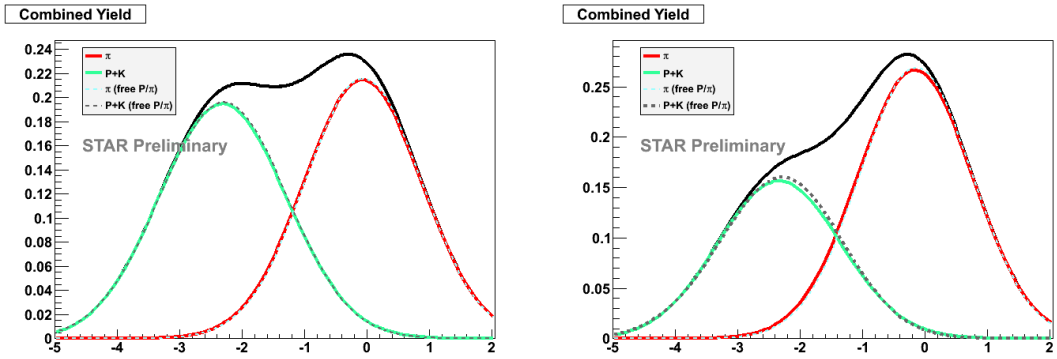

Figure 60. Reassembled PID distribution in 0-10% Au+Au (left) and MinBias d+Au (right). The dashed lines show the result of fits with free proton and kaon yields. The non-pion curve is the sum of proton and kaon gaussians.

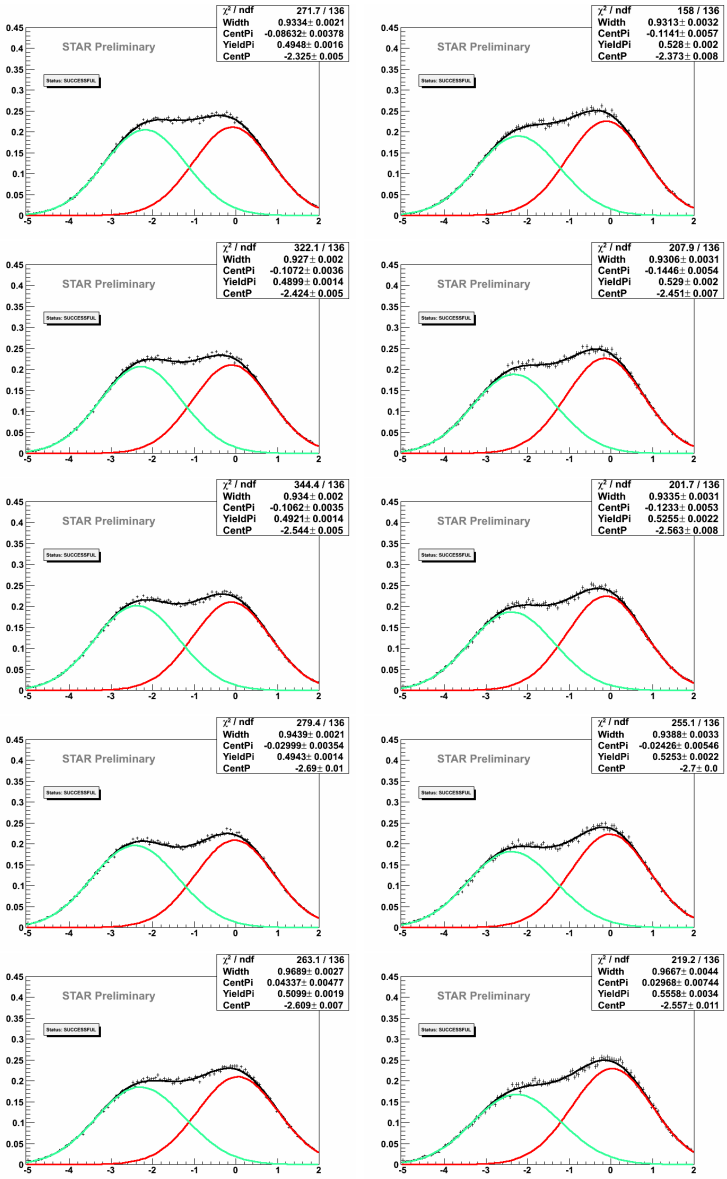

Figure 61. PID plots for Au+Au. Left: $p_T = 4 - 4.5$ GeV/c, right : $p_T = 4.5 - 5$ GeV/c. Top to bottom: $|\eta| = 0 - 0.2, \ldots, |\eta| = 0.8 - 1.0$. The non-pion curve is the sum of proton and kaon gaussians.

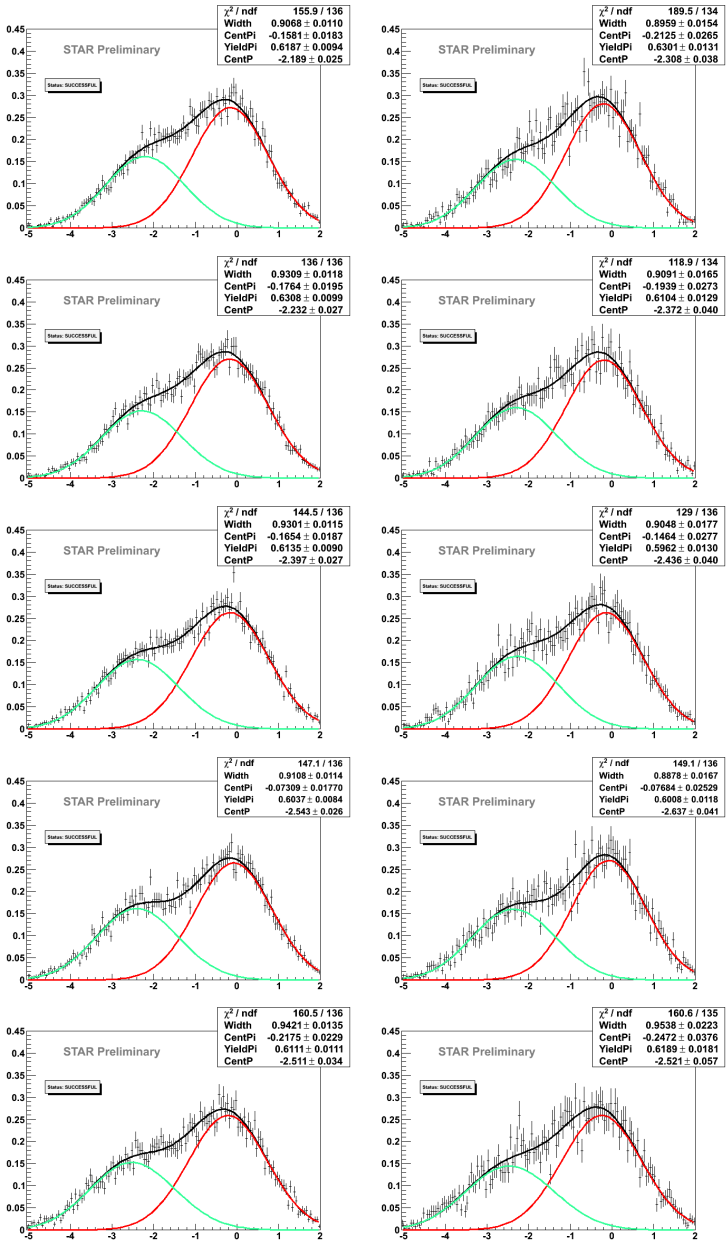

Figure 62. PID plots for d+Au. Left: $p_T = 4 - 4.5$ GeV/c, right : $p_T = 4.5 - 5$ GeV/c. Top to bottom: $|\eta| = 0 - 0.2, \ldots, |\eta| = 0.8 - 1.0$. The non-pion curve is the sum of proton and kaon gaussians.

Au+Au, $p_T = 4 - 4.5$ GeV/c					
$\|\eta\|$	0.0-0.2	0.2-0.4	0.4-0.6	0.6-0.8	0.8-1.0
χ^2/ndf	272 / 136	322 / 136	344 / 136	279 / 136	263 / 136
σ	0.93 ± 0.002	0.93 ± 0.002	0.93 ± 0.002	0.94 ± 0.002	0.97 ± 0.003
C_π	-0.09 ± 0.004	-0.11 ± 0.004	-0.11 ± 0.003	-0.03 ± 0.004	0.04 ± 0.005
C_P	-2.33 ± 0.005	-2.42 ± 0.005	-2.54 ± 0.005	-2.69 ± 0.005	-2.61 ± 0.007
$(C_K)/(C_P)$	0.74	0.73	0.72	0.70	0.67
Yield π	0.49 ± 0.002	0.49 ± 0.001	0.49 ± 0.001	0.49 ± 0.001	0.51 ± 0.002
Yield P	0.31 ± 0.001	0.31 ± 0.001	0.31 ± 0.001	0.31 ± 0.001	0.32 ± 0.001
Yield K	0.19	0.20	0.20	0.19	0.17

TABLE IV

PID results for Au+Au, $p_T = 4 - 4.5$ GeV/c.

Au+Au, p_T=4.5-5 GeV/c					
$\|\eta\|$	0.0-0.2	0.2-0.4	0.4-0.6	0.6-0.8	0.8-1.0
χ^2/ndf	158 / 136	208 / 136	202 / 136	255 / 136	219 / 136
σ	0.93 ± 0.003	0.93 ± 0.003	0.93 ± 0.003	0.94 ± 0.003	0.97 ± 0.004
C_π	-0.11 ± 0.006	-0.14 ± 0.005	-0.12 ± 0.005	-0.02 ± 0.005	0.03 ± 0.007
C_P	-2.37 ± 0.008	-2.45 ± 0.007	-2.56 ± 0.008	-2.70 ± 0.008	-2.56 ± 0.01
$(C_K)/(C_P)$	0.72	0.71	0.70	0.67	0.65
Yield π	0.53 ± 0.002	0.53 ± 0.002	0.53 ± 0.002	0.53 ± 0.002	0.56 ± 0.003
Yield P	0.28 ± 0.001	0.29 ± 0.001	0.28 ± 0.001	0.28 ± 0.001	0.30 ± 0.002
Yield K	0.19	0.19	0.19	0.19	0.14

TABLE V

PID results for Au+Au, p_T=4.5-5 GeV/c

d+Au, p_T=4-4.5 GeV/c					
$\|\eta\|$	0.0-0.2	0.2-0.4	0.4-0.6	0.6-0.8	0.8-1.0
χ^2/ndf	156 / 136	136 / 136	144 / 136	147 / 136	161 / 136
σ	0.91 ± 0.01	0.93 ± 0.01	0.93 ± 0.01	0.91 ± 0.01	0.94 ± 0.01
C_π	-0.16 ± 0.02	-0.18 ± 0.02	-0.17 ± 0.02	-0.07 ± 0.02	-0.22 ± 0.02
CP	-2.19 ± 0.03	-2.23 ± 0.03	-2.40 ± 0.03	-2.54 ± 0.03	-2.51 ± 0.03
$(C_K)/(C_P)$	0.74	0.73	0.72	0.70	0.67
Yield π	0.62 ± 0.009	0.63 ± 0.01	0.61 ± 0.009	0.60 ± 0.008	0.61 ± 0.01
Yield P	0.28 ± 0.004	0.29 ± 0.005	0.28 ± 0.004	0.27 ± 0.004	0.28 ± 0.005
Yield K	0.10	0.08	0.11	0.12	0.11

TABLE VI

PID results for d+Au, p_T=4-4.5 GeV/c

d+Au, p_T=4.5-5 GeV/c					
$\|\eta\|$	0.0-0.2	0.2-0.4	0.4-0.6	0.6-0.8	0.8-1.0
χ^2/ndf	190 / 134	119 / 134	129 / 136	149 / 136	161 / 135
σ	0.90 ± 0.02	0.91 ± 0.02	0.90 ± 0.02	0.89 ± 0.02	0.95 ± 0.02
C_π	-0.21 ± 0.03	-0.19 ± 0.03	-0.15 ± 0.03	-0.08 ± 0.03	-0.25 ± 0.04
C_P	-2.31 ± 0.04	-2.37 ± 0.04	-2.44 ± 0.04	-2.64 ± 0.04	-2.52 ± 0.06
$(C_K)/(C_P)$	0.72	0.71	0.70	0.67	0.65
Yield π	0.63 ± 0.01	0.61 ± 0.01	0.60 ± 0.01	0.60 ± 0.01	0.62 ± 0.02
Yield P	0.19 ± 0.005	0.19 ± 0.005	0.18 ± 0.005	0.18 ± 0.005	0.19 ± 0.007
Yield K	0.13	0.16	0.18	0.17	0.14

TABLE VII

PID results for d+Au, p_T=4.5-5 GeV/c

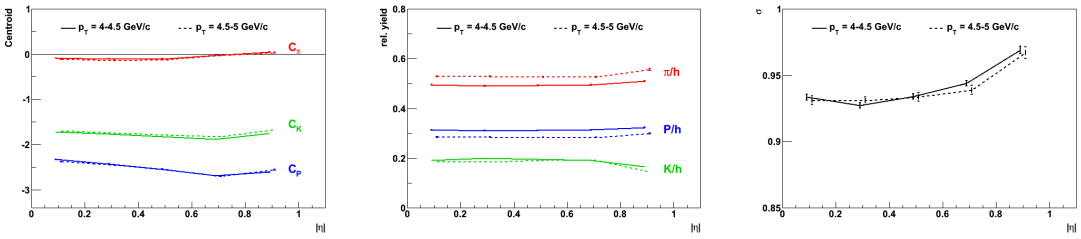

Figure 63. For Au+Au. Left: $|\eta|$-dependence of centroid positions in both p_T bins. Middle: $|\eta|$-dependence of relative yields in both p_T bins. Right: $|\eta|$-dependence of the gaussian σ in both p_T bins. Note that kaon position, and kaon and proton yield, are not free parameters. Symbols are offset for visibility.

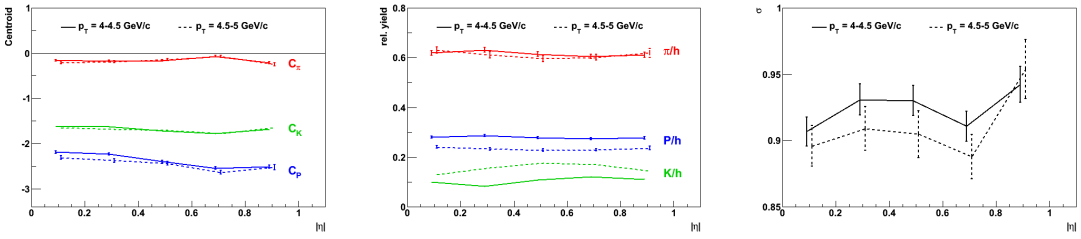

Figure 64. For d+Au. Left: $|\eta|$-dependence of centroid positions in both p_T bins. Middle: $|\eta|$-dependence of relative yields in both p_T bins. Right: $|\eta|$-dependence of the gaussian σ in both p_T bins. Note that kaon position, and kaon and proton yield, are not free parameters. Symbols are offset for visibility.

4.3.2 Separation and Non-Pion Purification

As is obvious from Figure 60, it is impossible to identify a particle type on a track-by-track basis. However, a separation between pion-triggers and a pion-depleted trigger set can be done with an n_σ^π cut at exactly 0, slightly to the right of the calibrated pion peak position. The pion contamination in the non-pion sample is then determined by integrals over the combined fit results presented in Figure 60. The composition of the trigger sets as well as the composition of "inclusive" triggers without n_σ^π cut is shown in Table VIII. Purity of the "pure pion" cut is 97.7% for Au+Au and 98.7% for d+Au. The table also shows the individual P and K values. These are only used for the "pure proton" extrapolation in Figure 73, right panel.

Note that in this analysis, total yields are less important than pion-contamination of the pion-depleted trigger set. Although uncertainties on the statistical separation of protons from kaons are too big for a meaningful correlation analysis, separation of pion from non-pion (i.e., P+K) triggers is very stable; any change in proton yield is soaked up by the kaon yield, and the pion yield is essentially unaffected. All fitting variations result in a pion contamination range in the depleted sample of 35.4-35.7%. Only the derived "pure proton" quantities have larger uncertainties since they are more directly affected by the P/π input.

Then, two correlations are constructed—one with "pure-pions", and the other one "pion-depleted". The pion-depleted one has the other about 50% of the pions, i.e. identical

Au+Au				
Cut	π	non-π	P	K
All Triggers	0.506	0.494	0.306	0.188
Pure Pions	0.977	0.023	0.004	0.019
Pion-Depleted	0.354	0.646	0.403	0.243
d+Au				
Cut	π	non-π	P	K
All Triggers	0.614	0.386	0.265	0.121
Pure Pions	0.987	0.013	0.003	0.010
Pion-Depleted	0.478	0.522	0.361	0.161

TABLE VIII

Trigger PID composition

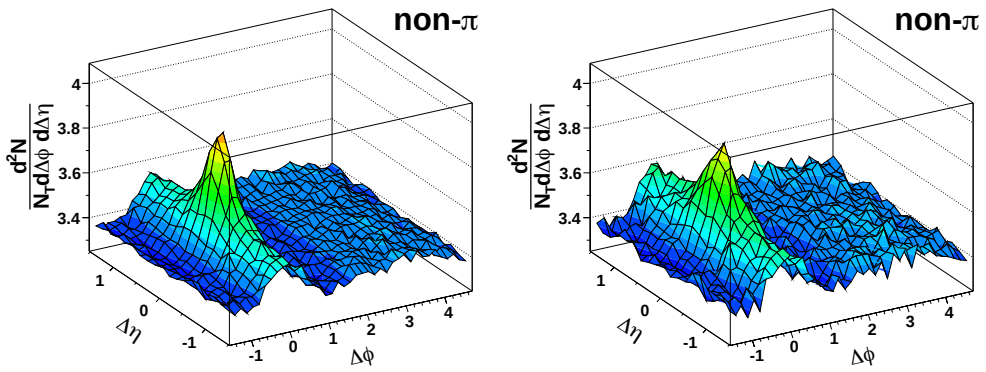

Figure 65. Comparison of correlation functions for pion-depleted triggers (left) and purified non-pion-triggers from 0-10% most-central Au+Au at 200 GeV. All trigger and associated charged hadrons are selected in the respective p_T ranges $4 < p_T^{\mathrm{trig}} < 5$ GeV/c and $1.5 < p_T^{\mathrm{assoc}} < 4$ GeV/c.

contribution to the pure-pion triggers. This pure-pion correlation is subtracted (bin-wise in 2D), weighted to exactly match the pion contamination, and the remainder thus has only contribution from proton and kaon triggers, see Figure 65. All correlations are normalized per-trigger, thus there is no need to correct for trigger reconstruction efficiency.

The systematic uncertainty on compositions from repeating the particle identification procedure within the uncertainty range of published P/π [179, 98] leads to Table IX and Table X. The result from free fits is contained within this range.

Au+Au; Low P/π=0.603 (4-4.5 GeV), 0.512 (4.5-5 GeV)				
Cut	π	non-π	P	K
All Triggers	0.504	0.496	0.290	0.206
Pure Pions	0.977	0.023	0.003	0.020
Pion-Depleted	0.352	0.648	0.382	0.266
Au+Au; High P/π=0.665 (4-4.5 GeV), 0.566 (4.5-5 GeV)				
Cut	π	non-π	P	K
All Triggers	0.508	0.492	0.323	0.169
Pure Pions	0.977	0.023	0.005	0.018
Pion-Depleted	0.357	0.643	0.425	0.218

TABLE IX

Au+Au trigger PID composition uncertainties.

d+Au; Low P/π=0.413 (4-4.5 GeV), 0.347 (4.5-5 GeV)				
Cut	π	non-π	P	K
All Triggers	0.610	0.390	0.239	0.151
Pure Pions	0.987	0.013	0.002	0.011
Pion-Depleted	0.472	0.528	0.326	0.202
Au+Au; High P/π=0.496 (4-4.5 GeV), 0.418 (4.5-5 GeV)				
Cut	π	non-π	P	K
All Triggers	0.620	0.380	0.293	0.087
Pure Pions	0.988	0.012	0.004	0.008
Pion-Depleted	0.486	0.514	0.398	0.116

TABLE X

d+Au trigger PID composition uncertainties.

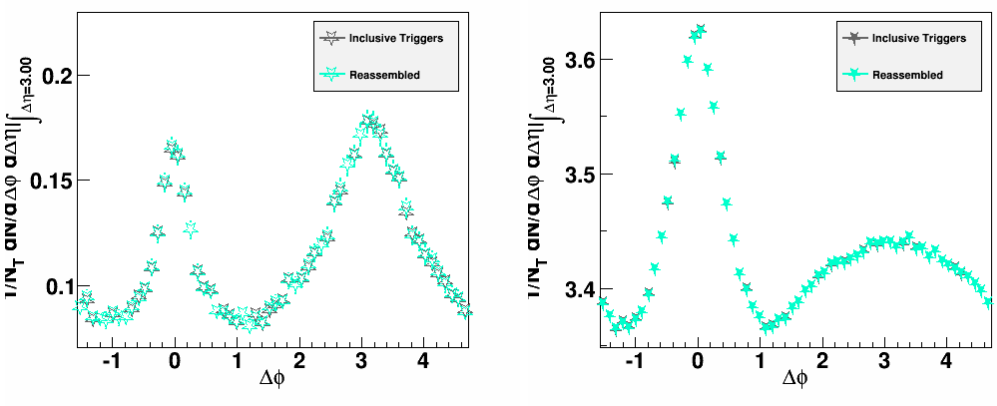

Figure 66. Projection over $|\Delta\eta| < 1.5$ for d+Au (left) and Au+Au (right). Gray symbols correspond to inclusive triggers (without PID cut), teal symbols come from the weighted sum of π and (P+K) triggers.

4.3.2.1 Cross-check–Reassembly

It is an essential sanity requirement that, properly weighted, the sum of π- and (P+K)-triggered correlation functions recovers the inclusive one. Figure 66 demonstrates that this is indeed the case.

CHAPTER 5

RESULTS

The two-dimensional correlations, fully corrected for efficiency and acceptance effects, are shown in Figure 67 for charged hadrons, pions, and non-pions in Au+Au and d+Au. Details about the statistical separation of pion triggers from non-pions are presented in Section 4.3.

In Au+Au data, stark differences between pion and non-pion triggers are immediately visible before background subtraction in the two distinct regions. At large $\Delta\eta$, a long-range plateau on the near-side, the ridge, is much higher for proton+kaon triggers than for pions. In the near-side jet-like cone region (at small relative angles), pion triggers elicit a higher correlation strength compared to the other trigger types. In the same Figure, jet-cone differences can be seen in d+Au data as well. Separation of kinematic from medium effects require further quantitative analysis. Jet-cone region and large-$\Delta\eta$ differences are considered individually in the next two sections.

Details about systematic uncertainties are found in Appendix A and B. An estimate of the effect of secondary particles from feed-down processes on the trigger sample is provided in Appendix C.

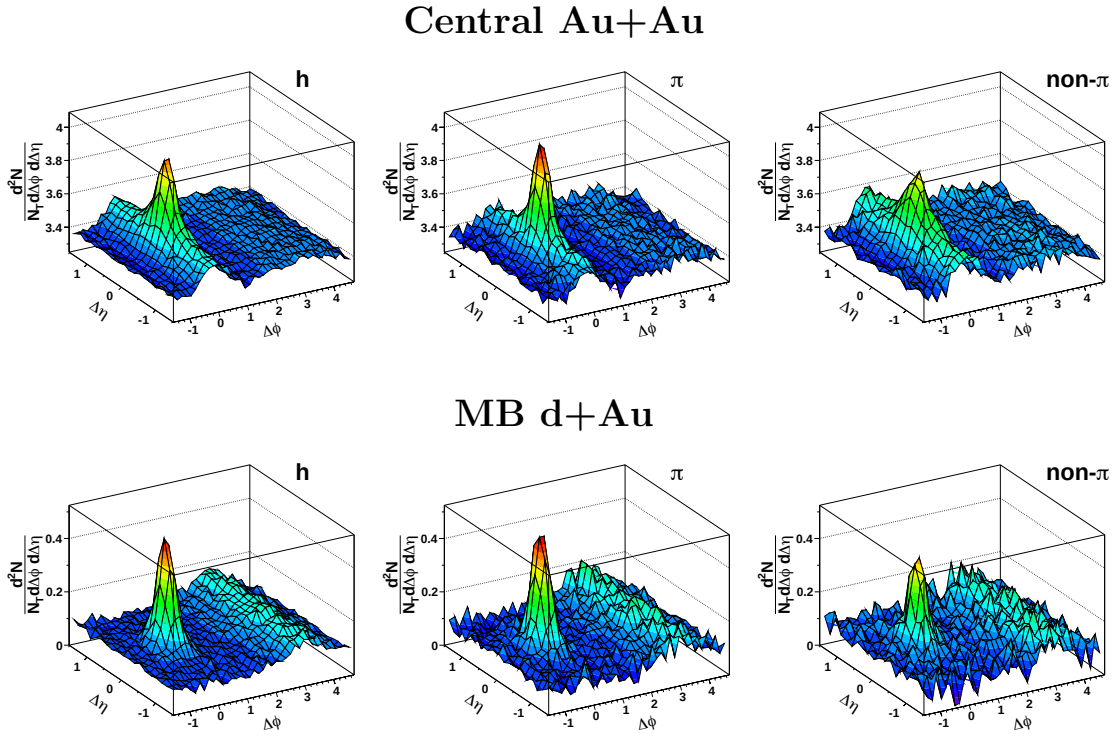

Figure 67. Two-dimensional $\Delta\phi$ vs. $\Delta\eta$ correlation functions for charged hadron (left), pion (middle), and non-pion (right) triggers from 0-10% most-central Au+Au (top row) and Minimum Bias d+Au (bottom) data at 200 GeV. All trigger and associated charged hadrons are selected in the respective p_T ranges $4 < p_T^{\rm trig} < 5$ GeV/c and $1.5 < p_T^{\rm assoc} < 4$ GeV/c.

5.1 Small $\Delta\eta$, $\Delta\phi$ – Jet-like Yield

The small-angle jet-like correlated signals can be isolated by subtracting all $\Delta\eta$-independent contributions (such as random pairs, ridge, and elliptic flow) averaged over large relative pseudorapidity angles $|\Delta\eta| = 0.9$–1.5 from the full two-dimensional correlations. This procedure is justified based on the results of two-dimensional fits to the data described in Section 5.2, and it does not invoke any assumptions beyond $\Delta\eta$-independence of those contributions. To separate medium effects from initial-state nuclear effects, the result is directly compared to the correlation function constructed in an identical way for d+Au data. The resulting "pure-cone" distributions are shown in Figure 68, and projections on relative azimuth and pseudorapidity in Figure 69. The fiducial jet-like yield is then calculated for each correlation as histogram integrals over $|\Delta\eta| < 0.78$, $|\Delta\phi| < \pi/4$ as in [25].

For quantitative comparisons, the integrated yields are presented in Table XI. The cut at $|\Delta\eta| = 0.9$ ensures capturing $\approx 98\%$ of the jet cone width; additionally, Table XI also shows extrapolated values outside the fiducial range, obtained using jet-shape modeling parameters obtained in Section 5.2.

In the transverse momentum range studied (1.5-4 GeV/c), the jet-like yield associated with pion triggers in central Au+Au collisions is found enhanced by 24 ± 6(stat.)±11(sys.)% with respect to the reference measurement in d+Au. At the same time, the associated yields for non-pion triggers are found to be similar between the two systems. The jet-like yield for

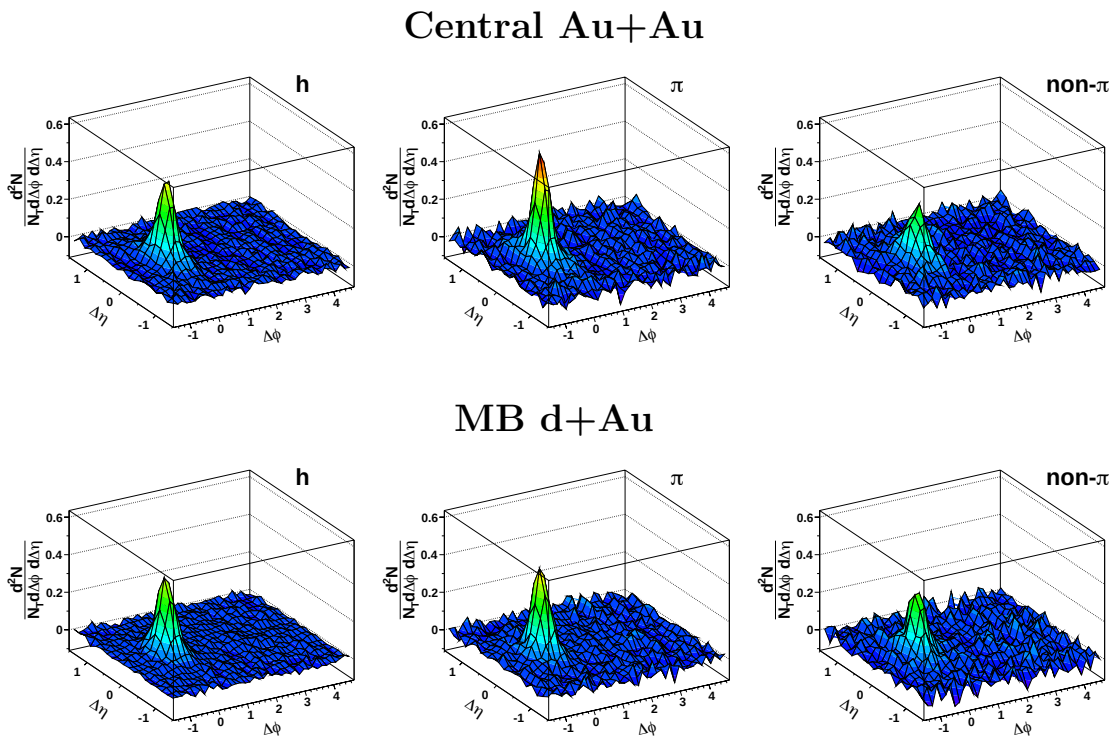

Figure 68. Two-dimensional "Pure Cone" distributions without trigger PID cuts (left), with leading pions (middle), and leading non-pions (right). Top row: 0-10% Au+Au, bottom row: Minimum Bias d+Au.

unidentified charged hadron triggers is also enhanced, consistent with the sum of the identified trigger results. Two previous works studied "near-side" yield for identified charged meson and baryon triggers, albeit in different p_T regions. In ref. [180], triggers between 2.5 and 4 GeV/c were separated between mesons (kaons and pions) and baryons (protons). The near-side associated yield between 1.7 and 2.5 GeV/c are identical within errors. In central

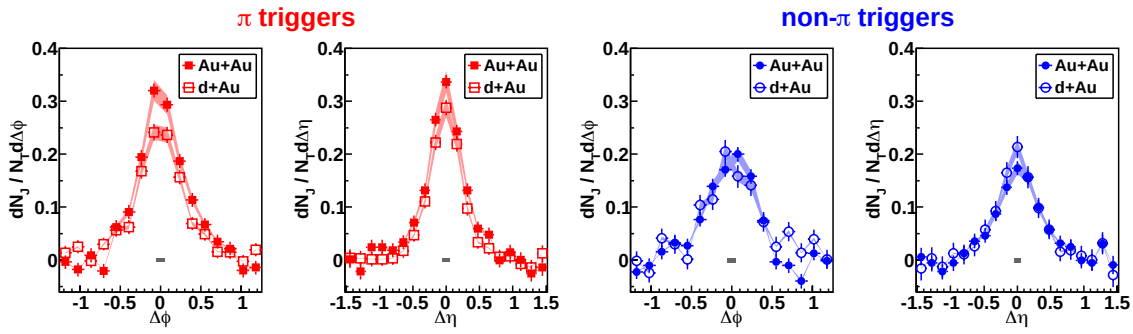

Figure 69. The $\Delta\phi$ and $\Delta\eta$ projections of the pure-cone correlations for $|\Delta\eta| < 0.78$ and $|\Delta\phi| < \pi/4$, respectively, for pion triggers (left two panels) and non-pion triggers (right two panels). Filled symbols show data from the 0-10% most-central Au+Au collisions at 200 GeV; open symbols show data from minimum-bias d+Au data at the same energy. Shaded boxes show the uncertainty in background level determination; colored bands show the remaining systematic uncertainties.

Au+Au collisions, the data in this reference indicate (with large uncertainties) enhanced near-side yield per meson trigger while the yield associated with baryon triggers is unchanged or slightly decreased, in qualitative agreement with the findings here. Preliminary results in ref. [181], show identical associated near-side yield between 0.15 and 3 GeV/c for identified pion triggers and for a set of proton-rich triggers with $p_T^{\rm trig} = 3 - 3.5$ GeV/c in central Au+Au. In addition to differences in the kinematic selection, it is important to note that both these analyses were carried out in relative azimuth only, thus conflating

Trigger	**Au+Au 0-10%**				**d+Au MinBias**			
	Fid.	Ext.	Stat.	Sys.	Fid.	Ext.	Stat.	Sys.
π	0.211	0.214	3%	7%	0.171	0.171	4%	6%
non-π	0.136	0.142	5%	6%	0.142	0.148	7%	8%
All	0.176	0.180	2%	5%	0.161	0.168	2%	5%

TABLE XI

Fiducial (($|\Delta\eta| < 0.78$) $\times$ ($|\Delta\phi| < \pi/4$)) and extrapolated (see text) pure cone yields for pion, non-pion and charged hadron (unidentified) triggers.

	Au+Au 0-10%	**d+Au MinBias**
Fiducial $\frac{\mathrm{Y(non\text{-}\pi)}}{\mathrm{Y}(\pi)}$	0.643 $\pm$ 0.038 (stat.) $\pm$ 0.034 (sys.)	0.835 $\pm$ 0.066 (stat.) $\pm$ 0.068 (sys.)
Extrapolated $\frac{\mathrm{Y(non\text{-}\pi)}}{\mathrm{Y}(\pi)}$	0.662 $\pm$ 0.039 (stat.) $\pm$ 0.035 (sys.)	0.866 $\pm$ 0.068 (stat.) $\pm$ 0.071 (sys.)

TABLE XII

Yield ratios.

jet-like peak and ridge contributions; the lack of pair acceptance correction in $\Delta\eta$ furthermore distorted the ridge shape. The better agreement with the PHENIX [180] result could therefore be a consequence of the smaller η acceptance of 0.35, which reduces the influence of the ridge compared to STAR.

The observed enhancement for soft associated hadrons in the jet-like cone can be attributed to the jet-quenching effect and/or medium-induced modification of fragmentation functions, as previously found at RHIC and the LHC via direct jet measurements [114, 182, 183, 184]. Energy lost to the hot medium would lead to final state trigger hadrons to be biased toward more energetic energy initial jets, and to a softened associated hadron spectrum. At the same time, this shifted energy would still be primarily aligned with the jet axis, be it via small-angle gluon bremsstrahlung in a radiative energy loss scenario, or momentum transfer in collisonal energy loss, thus leading to larger yields for soft hadrons near the trigger.

The lack of enhancement for non-pion triggers is difficult to reconcile with fragmentation mechanisms alone. One possible source of trigger type dependence is a relatively higher gluon jet admixture for proton triggers predicted by NLO calculations in [11]. Since medium-induced radiation is stronger for gluons by a factor of 9/4, this would however lead to *higher* yields associated with non-pion triggers. The data here does not preclude a difference between quark and gluon jets from potentially playing a role, but there should be an off-setting mechanism driving the difference between pion- and non-pion-led jet-like yield. Such an off-setting effect, leading to the relative yield reduction for non-pion vs.

pion triggers in central Au+Au collisions, is qualitatively consistent with trigger pool dilution via hadrons produced by recombination/coalescence mechanisms, where a relatively larger fraction of trigger baryons are produced through recombination of thermal quarks, i.e. without associated jet-like yields.

To quantify the relative suppression of associated yields between non-pion and pion leading hadrons, the ratios of such yields for each of the colliding systems are shown in Table XI. In these ratios, dominant contributions to systematic uncertainties from the tracking efficiency estimate cancel out. The double-ratio constructed from these two results, i.e. the relative decrease in associated extrapolated yields for non-pion triggers with respect to leading pion results, in Au+Au with respect to d+Au,

$$R^{\mathrm{J}} \equiv \left(\frac{\text{Yield of non-}\pi\text{ triggers}}{\text{Yield of }\pi\text{ triggers}} \text{in Au+Au} \right) / \left(\frac{\text{Yield of non-}\pi\text{ triggers}}{\text{Yield of }\pi\text{ triggers}} \text{in d+Au} \right), \quad (5.1)$$

is found to be

$$R^{\mathrm{J}}_{\mathrm{fid}} = 0.771 \pm 0.076\ (\text{stat.}) \ \pm 0.067\ (\text{sys.})\ (\text{fiducial}) \quad (5.2)$$

$$R^{\mathrm{J}}_{\mathrm{ext}} = 0.764 \pm 0.075\ (\text{stat.}) \ \pm 0.066\ (\text{sys.})\ (\text{extrapolated})\ . \quad (5.3)$$

This double-ratio can be used to quantify the trigger dilution effects in central Au+Au collisions, although no quantitative predictions from recombination/coalescence models are yet available for direct comparison.

5.2 Large $\Delta\eta$ – Ridge Region

Outside of the small-angle jet-cone region, the correlated yields show no appreciable dependence on $\Delta\eta$ in the considered fiducial range. To characterize the long-range part of the measured correlation, and the ridge specifically, two-dimensional fits to the full 2D correlations are performed with two different models. Both models have a two-dimensional generalized Gauss peak at small angles to capture the features of the short-range correlations, but they have different physics mechanisms in mind for the long-range components. One attributes the cause of the ridge only to modified fragmentation of the produced mini-jets [185], and the other explains it in terms of higher-order anisotropies due to hydrodynamic flow [75].

Mathematically, the near-side jet-like peak is modeled in both models as follows:

$$\text{“Jet”} \propto e^{-(|\Delta\phi|/\alpha_\phi)^{\beta_\phi}} \, e^{-(|\Delta\eta|/\alpha_\eta)^{\beta_\eta}}, \tag{5.4}$$

where $\alpha_{\phi,\eta}$ describes the width in $\Delta\phi$ and $\Delta\eta$, respectively, and $\beta_{\phi,\eta}$ the shape ($\beta = 2$ corresponds to a conventional Gaussian, $\beta = 1$ to a falling exponential).

In the flow-based approach, all rapidity-independent parts of correlations are described via Fourier expansion:

$$\text{“Rest”} = A(1 + \sum_{n=1}^{N} 2V_n \cos n\Delta\phi), \tag{5.5}$$

with the first five terms (N=1–5) exhausting all features of the correlation to the level of statistical uncertainties. The parameter A describes the magnitude of uncorrelated background level. In this approach, the fragmentation contributions to the away-side correlations are expected to be strongly suppressed relative to flow effects, and they are therefore neglected.

In the mini-jet model in this analysis, the two first terms of the Fourier expansion are kept, with V_1 explained to capture the major part of away-side jet and/or momentum conservation effects, and V_2 describing elliptic flow.

$$\text{“Rest”} = A(1 + 2V_1 \cos\Delta\phi + 2V_2 \cos 2\Delta\phi) + B\, e^{-\Delta\phi^2/2\sigma^2}, \tag{5.6}$$

where B is the amplitude, and σ the width parameter. Here, the near-side ridge is modeled by a one-dimensional Gaussian These near-side model elements differ from those in [185], as the addition of the 1D Gaussian was necessary to reproduce the data.

Fit results and (flat, featureless) residuals using the “V_n” model are shown in Figure 70 and results in Table XIII. “Mini-jet” model fit residuals are shown in Figure 71 and results in Table XIV. For illustrative purposes, the rebinned version is shown instead of the finer binning that was actually used for fitting (80 bins in the $\Delta\phi$ dimension, and 150 bins for $|\Delta\eta| < 1.5$). Both models describe measured correlations for all three trigger types equally well, with identical χ^2 values and uniformly distributed residuals, and with identical jet cone descriptions, see Figure 72.

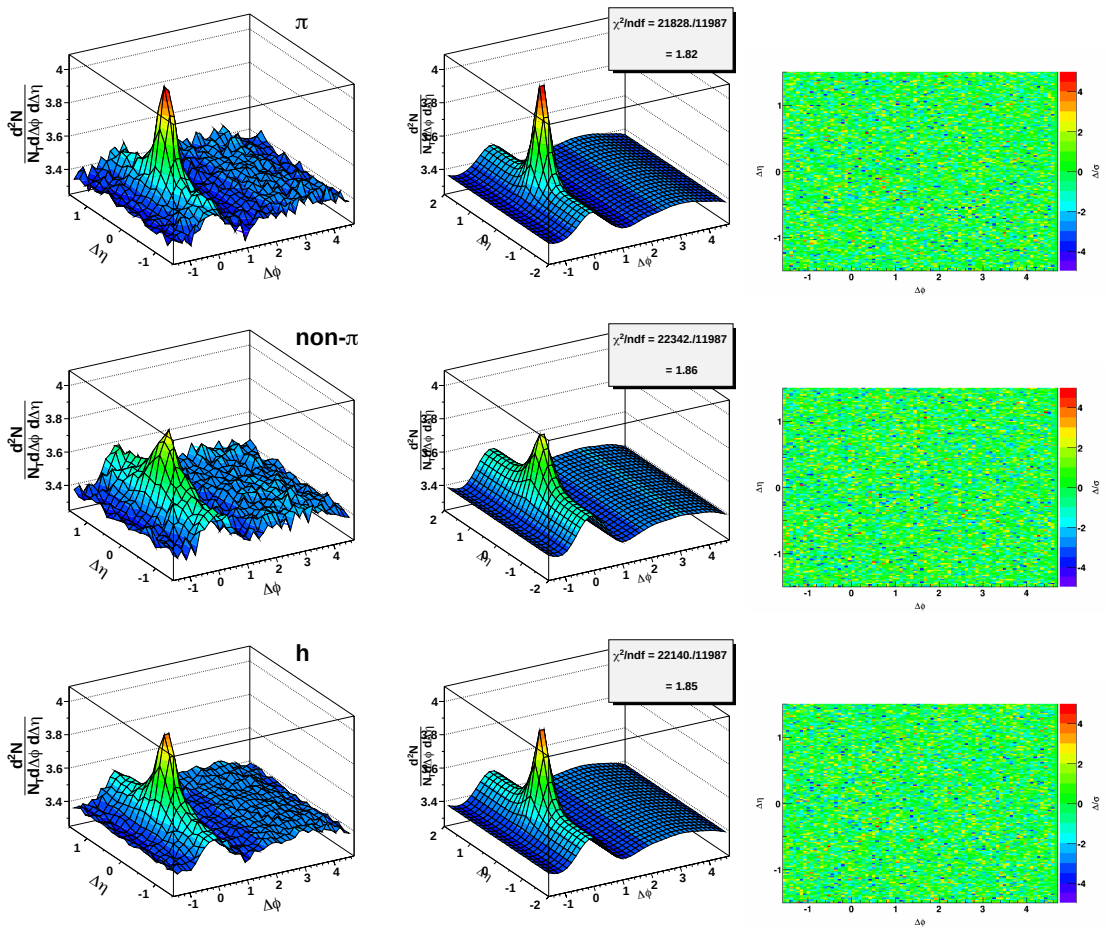

Figure 70. Top to bottom: "V_n"-type fit results for pions, non-pions, and unidentified triggers. Left to right: Data, fit, residuals. Residuals have been normalized by bin error; they represent number of standard deviations.

Trigger	π	P+K	All
χ^2 / ndf	1.82	1.86	1.85
$100\,V_1$	0.089 ± 0.016	0.278 ± 0.020	0.184 ± 0.008
$100\,V_2$	0.633 ± 0.015	0.830 ± 0.018	0.729 ± 0.008
$100\,V_3$	0.345 ± 0.014	0.565 ± 0.017	0.451 ± 0.007
$100\,V_4$	0.155 ± 0.014	0.224 ± 0.015	0.186 ± 0.007
$100\,V_5$	0.025 ± 0.013	0.034 ± 0.015	0.028 ± 0.007
SS Amp	0.664 ± 0.019	0.296 ± 0.015	0.486 ± 0.009
$\alpha_{\Delta\phi}$	0.302 ± 0.006	0.364 ± 0.010	0.324 ± 0.004
$\alpha_{\Delta\eta}$	0.295 ± 0.007	0.396 ± 0.018	0.322 ± 0.005
$\beta_{\Delta\phi}$	1.56 ± 0.07	2.19 ± 0.15	1.77 ± 0.05
$\beta_{\Delta\eta}$	1.42 ± 0.07	1.41 ± 0.12	1.34 ± 0.04

TABLE XIII

Fourier coefficients and fitting parameters with statistical errors using the "V_n" model for Au+Au data. Note the V_n scaling by 100.

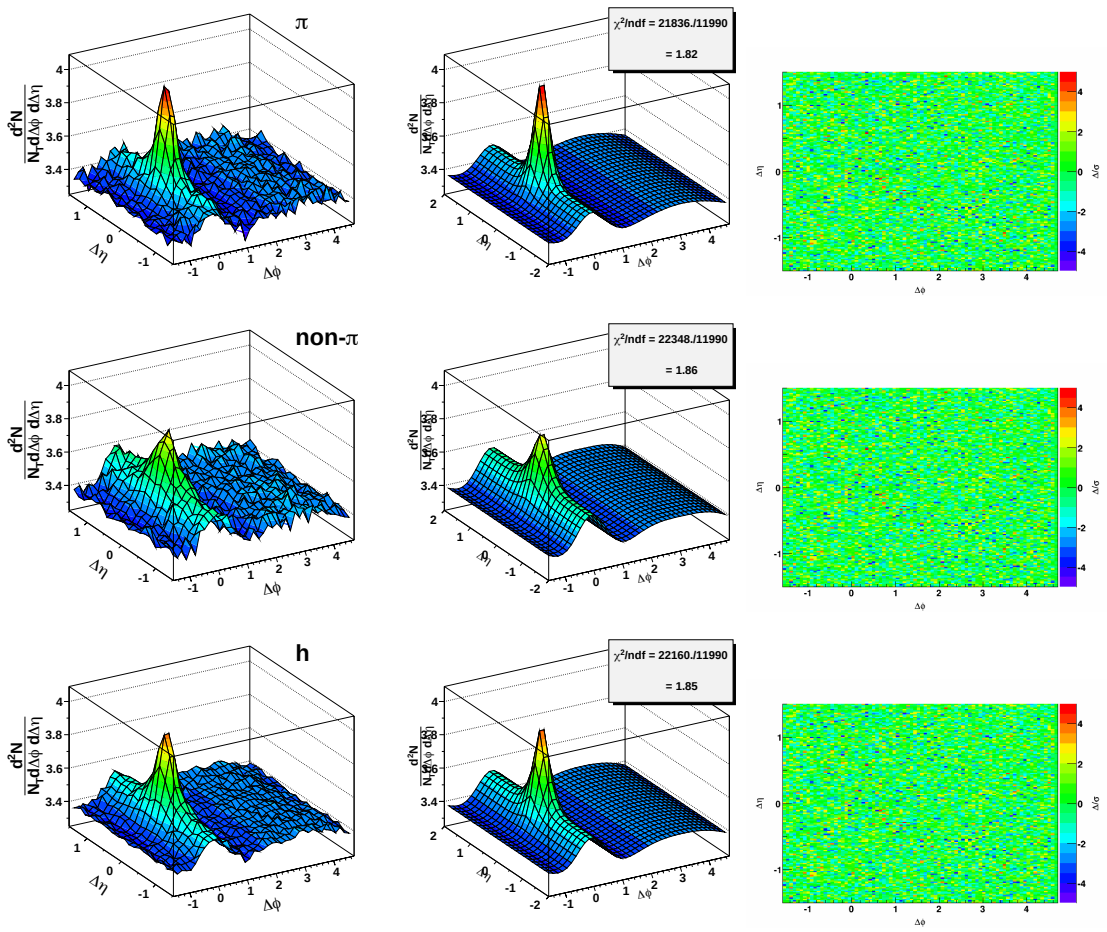

Figure 71. Top to bottom: "mini-jet"-type fit results for pions, non-pions, and unidentified triggers. Left to right: Data, fit, residuals. Residuals have been normalized by bin error; they represent number of standard deviations.

Trigger	π	P+K	All
χ^2 / ndf	1.82	1.86	1.85
$100\,V_1$	-0.86 ± 0.09	-1.53 ± 0.13	-1.19 ± 0.05
$100\,V_2$	-0.017 ± 0.045	-0.343 ± 0.059	-0.173 ± 0.025
Ridge Amp	0.23 ± 0.02	0.44 ± 0.03	0.33 ± 0.01
Ridge σ	0.50 ± 0.02	0.53 ± 0.01	0.52 ± 0.01
SS Amp	0.667 ± 0.019	0.288 ± 0.013	0.483 ± 0.008
$\alpha_{\Delta\phi}$	0.300 ± 0.006	0.372 ± 0.010	0.325 ± 0.004
$\alpha_{\Delta\eta}$	0.295 ± 0.007	0.392 ± 0.017	0.321 ± 0.005
$\beta_{\Delta\phi}$	1.56 ± 0.07	2.18 ± 0.15	1.76 ± 0.04
$\beta_{\Delta\eta}$	1.42 ± 0.07	1.46 ± 0.12	1.36 ± 0.04

TABLE XIV

Model coefficients and fitting parameters with statistical errors using the "mini-jet" model for Au+Au data. Note the V_n scaling by 100.

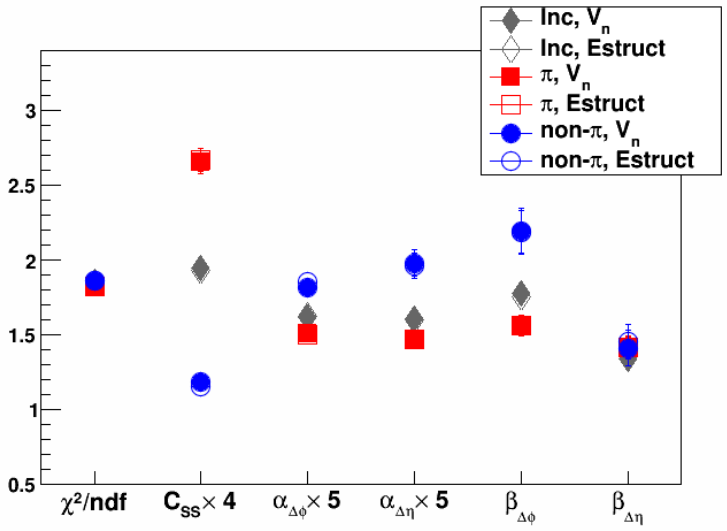

Figure 72. Reduced χ^2 and generalized Gaussian parameters for both fit models and all three trigger types in Au+Au.

The $\Delta\phi$ projections of pseudorapidity-independent parts of the 2D correlations (after subtracting the jet-like peak), are shown in Figure 73 (a), together with the fit functions. The azimuthal harmonic amplitudes are shown in Figure 73 (b); their physical implications are discussed below.

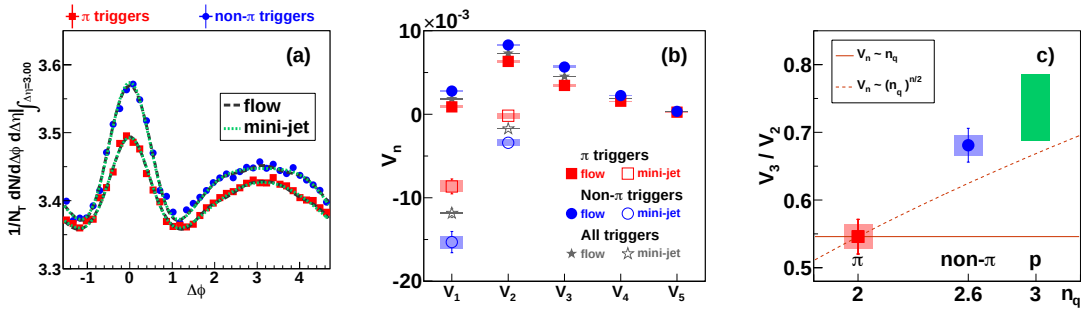

Figure 73. a) $\Delta\phi$ projections over $|\Delta\eta| < 1.5$ after subtracting the jet-like fit components. Solid and dashed lines illustrate the results of the 2D fits for the flow- and mini-jet based models, respectively (stat. errors only). b) Solid symbols show extracted Fourier coefficients for pion, non-pion, and charged hadron triggers for the flow-based model; open symbols for the mini-jet approach. c) V_3/V_2 ratio for pion and non-pion triggers, and the extrapolated value for "pure protons", as described in the text. Also shown are scaling curves anchored at the pion value assuming perfect $n_{\rm q}$ scaling and the $V_n \sim n_{\rm q}^{n/2}$ scaling proposed in [96], corresponding to $V_3/V_2 \sim n_{\rm q}^{1/2}$. All panels show 0-10% Au+Au data at 200 GeV, with statistical errors shown as lines (smaller than symbol size for some points) and systematic uncertainties as colored boxes.

The Fourier expansion in the flow-based model shows that the second, elliptic harmonic (V_2) is dominant in all long-range correlations for the central data, followed by the triangular (V_3) term. Higher-order harmonic amplitudes rapidly decrease, and in this analysis are consistent with zero within errors for $n > 5$. All harmonic amplitudes for non-pion triggers are found to be larger than those for pions, which is qualitatively consistent with expectations from thermal quark recombination, as observed previously for identified particle measurements of elliptic flow [86, 87]. Note that in the considered $p_T^{\rm trig}$ range, previous measurements suggest that the anisotropies are largely independent of p_T [186].

To test the scaling behavior further, the ratios of the two dominant terms for different types of triggers were examined. In this test, the measured Fourier coefficients are assumed to factorize into $V_n = \langle v_n^{\rm trig}\rangle\langle v_n^{\rm assc}\rangle$, where $v_n^{\rm trig}$ and $v_n^{\rm assc}$ measure azimuthal anisotropies of trigger and associated hadrons, respectively [75] (see also the derivation in Section 2.2.1.1.2). Since the selection of associated particles is identical for all correlations in this analysis, the anisotropy contributions from associated hadrons should therefore cancel in the ratios of V_n coefficients.

Figure 73 (c) shows the ratio V_3/V_2 extracted from long-range correlations versus the number of constituent quarks ($n_{\rm q}$) for pion and non-pion triggers. The ratio of triangular and elliptic flow is found to be $0.546\pm0.025({\rm stat.})\pm0.018({\rm sys.})$ for pion triggers and $0.681\pm 0.025({\rm stat.})\pm0.015({\rm sys.})$ for non-pions. If the measured final-state azimuthal anisotropies are indeed of collective partonic origin, transformed into final-state hadronic observables through coalescence/recombination of constituent (thermal) quarks, the same dependence

of all v_n^{trig} on constituent quark number should be expected. By contrast, even though the non-pion measurement has a significant meson contribution (about 40% kaons), the ratios give a strong indication of a breaking of the n_{q} scaling behavior between the second and third Fourier harmonics. Assuming that kaons, as mesons, follow the pion scaling trend, an estimate for "pure protons" can then be computed: The kaon and proton fractions, f_K, f_P with $f_K + f_P = 1$, in the non-pion set can be determined using the known P/π ratio reported in [187, 179]. Then:

$$V_n(\text{meson}) \equiv V_n(\text{K}) = V_n(\pi) \tag{5.7}$$

$$V_n(\text{baryon}) \equiv V_n(\text{P}) = \frac{1}{f_P}\left(V_n(\text{non-}\pi) - f_K V_n(\pi)\right). \tag{5.8}$$

This estimated V_3/V_2 ratio for pure protons is shown as well in Figure 73 (c), to better illustrate variation from the n_{q} scaling behavior. The systematic uncertainty in the estimated pure-proton V_3/V_2 value of $0.736 \pm 0.038(\text{stat.}) \pm 0.032(\text{sys.})$ includes an additional 1% uncertainty from PID. At the moment, only recombination/coalescence models are able to provide a physical description of the constituent quark scaling behavior observed in elliptic flow of multiple identified hadron species. The V_3 scaling behavior shown in Figure 73 c) is therefore unexpected within the context of just hydrodynamics and recombination, and suggests the need for other physics contributions to explain the data. The phenomenological $V_n \sim n_{\text{q}}^{n/2}$ scaling proposed in [96], also shown in Figure 73, describes the measured V_3/V_2 ratios better, but still under-predicts the enhancement for non-pion triggers.

The deviation from n_{q} scaling is demonstrated in a different visualization in Figure 74: $V_n(\mathrm{baryon})/V_n(\mathrm{meson})$ should be equal to 3/2 if the n_{q}-scaling assumption holds true. For the elliptic flow, this assumption is fulfilled very well, but triangular flow shows significant deviation. Again, $V_n \sim n_{\mathrm{q}}^{n/2}$ describes the data better, yet still under-predicts it. To quantify the scaling deviation, V_3/V_2 is nevertheless the preferable quantity since it can be considered without pure proton calculations, and because some systematic uncertainties cancel out.

Within the mini-jet approach, the away-side structure is for the most part described by the V_1 term. Consequently, the V_1 amplitude is significantly larger for leading non-pions than for pions. If V_1 is to be associated with back-to-back jets, its increase would require both the jet-like peak and the ridge to be part of the leading jet, because the jet-like peak alone decreases for non-pion trigger particles. An understanding of the behavior of the V_2 term in the mini-jet model fits is challenging: the V_2 amplitude, while consistent with zero for pions similar to what was previously seen in charged hadron measurements [188], is significantly negative for non-pions. This negative value for V_2, which is conventionally associated with elliptic flow, is not expected from any known source and calls into question the applicability of the assumed parameterization for the centrality and p_T range studied here, the validity of the mini-jet + V_2 physics scenario, or both.

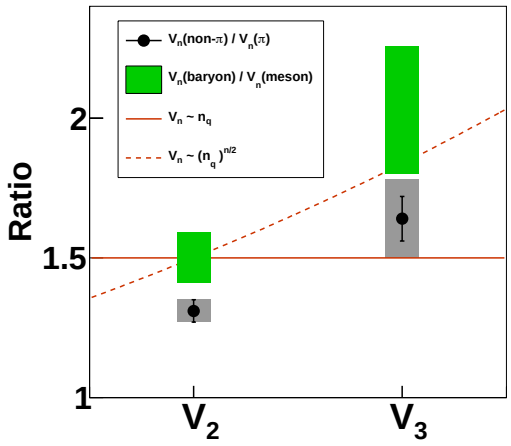

Figure 74. Data points show $V_n(\text{non-}\pi)/V_n(\pi)$ for V_2 and V_3. Statistical errors shown as lines and systematic uncertainties as gray boxes. Green boxes show calculated $V_n(\text{baryon})/V_n(\text{meson})$ (see text) with uncertainties added in quadrature. Also shown are scaling curves anchored at the V_2 value assuming perfect n_q scaling and the $V_n \sim n_\text{q}^{n/2}$ scaling proposed in [96], corresponding to $V_3/V_2 \sim n_\text{q}^{1/2}$.

5.3 Summary

A statistical separation of pion and non-pion (proton plus kaon) triggers was performed to study the systematic behavior of di-hadron correlations from central Au+Au and minimum-bias d+Au collisions at 200 GeV with the STAR experiment. The measured correlations are decomposed into short-range (jet-like), and long-range (ridge and away-side) parts and studied separately for trigger type dependencies.

At small relative angles, the jet-like associated charged hadron yields in the momentum range of 1.5–4 GeV/c is enhanced compared to a reference d+Au measurement before trigger identification. Such a near-side enhancement (without trigger identification) is consistent with the jet-quenching effect and/or medium-induced change of the fragmentation function. The relative reductions of yields for non-pion vs. pion triggers in central Au+Au collisions, contrary to pQCD-based expectations, suggests that trigger pool dilution from recombination/coalescence mechanisms plays a significant role; the new measurements provided here are well suited for future quantitative model comparisons.

The pseudorapidity-independent parts of the correlations show a significantly larger ridge-like yield and away-side correlation strength for non-pion triggers than for pions. Further analysis was carried out using two fit models which are mathematically similar and lead to statistically equivalent descriptions of the data, but which represent quite different physical models. Both describe the correlations within uncertainties and with

featureless residuals. However, in both cases, some of the fitting parameters attain values which are problematic for the assumed physical scenarios.

In a higher-flow-harmonics description, the different V_3/V_2 ratios observed for the two trigger types imply that the explanation of the ridge and away-side modifications as resulting only from hydrodynamic flow of a partonic medium with constituent quark degrees of freedom at hadronization is incomplete. On the other hand, the negative V_2 result for the mini-jet based model for leading non-pions indicates that for the data reported here either the assumed scenario or the mathematical parameterization for jets and dijets is inadequate, or both.

APPENDICES

Appendix A

SOURCES OF SYSTEMATIC UNCERTAINTY IN THE PURE CONE

The following sources of systematic uncertainty were considered for Figure 69 and the calculated yields:

Tracking Efficiency A standard value of 5% overall yield uncertainty was applied to account for uncertainty in the single particle efficiency correction. This affects yield comparison between Au+Au and d+Au, but it is not relevant for correlation comparison of different trigger types within the same data set.

Pair Acceptance Uncertainty due to pair acceptance would stem from the normalization uncertainty. It was estimated by varying the bin used to determine the maximum of the $\Delta\eta$-projected mixing background and found to be less than 1%.

Track Splitting By varying the size of the correction cell, the uncertainty was estimated to 1.3% in the jet-like cone yield.

p_T Resolution As shown in Figure 75, the p_T resolution above 4 GeV/c is better than 2%, and even better in the associate p_T range. The effect of trigger p_T uncertainty was tested by smearing the trigger p_T with an appropriate p_T-dependent gaussian. The effect on the jet-like yield is 3.2% (Au+Au) and 2.5% (d+Au), respectively.

PID In addition to repeating the analysis with values from Table IX and Table X, a PID-related uncertainty was obtained by varying the n_σ^π cut position between -0.2 and

Appendix A (Continued)

0.5, then using the standard deviation of measured quantities. The effect on cone yield is 1-3%, the effect on the double ratio is 4%.

Ridge Region The "pure ridge" region to be subtracted was defined as $0.9 < |\Delta\eta| < 1.5$. This region was varied in ten steps from $0.8 < |\Delta\eta| < 1.4$ to $1.0 < |\Delta\eta| < 1.6$. The standard deviation of these values was used as the associated uncertainty for the pure cone yield. Effect on the yield is 1-2% except for non-pion-triggered d+Au where statistical fluctuations led to a larger uncertainty of 5%. The effect on non-π/π ratios is 2.4% in Au+Au, 6.8% in d+Au, and 7.2% in the double ratio.

Jet-like Yield Extrapolation The scale factor is so close to unity that second order effects from jet cone shape uncertainty are insignificant.

Numerical values of systematic uncertainty are the quadrature sum of the above components. In Figure 69, the uncertainty in the background level determination is shown separately.

Appendix A (Continued)

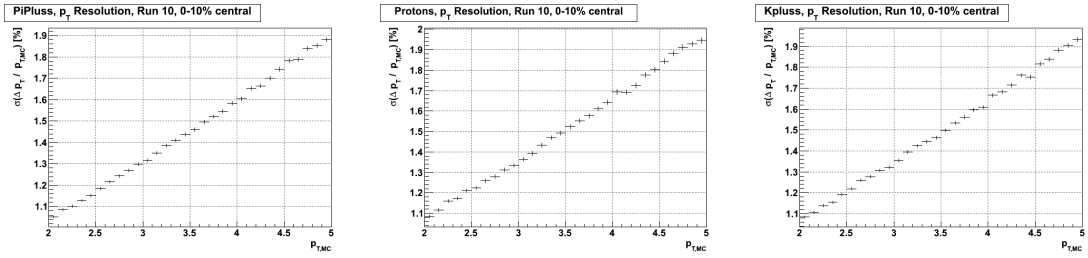

Figure 75. Left to right: p_T resolution $\sigma\left(\frac{p_T - p_{T,MC}}{p_{T,MC}}\right)$ from embedding data as a function of p_T for pions, protons, and kaons with trigger cuts, from embedding.

Appendix B

SOURCES OF SYSTEMATIC UNCERTAINTY IN THE FIT COEFFICIENTS

Many of the systematic uncertainties in yields do not affect V_n values. The following sources of systematic uncertainty were considered for Figure 73, Figure 74, and calculated ratios:

PID Using the same variations as for the yield, PID-related uncertainty on the V_n and ratios is similar to or smaller than statistical errors. Pure proton calculations have an additional 1% uncertainty, as noted.

V_n **Fit Range** To properly distinguish jet cone from $\Delta\eta$-independent terms, the fitter needs a good amount of cone and ridge, and the uncertainty was therefore determined by the standard deviation when varying the fit range from $|\Delta\eta| < 1.3$ to $|\Delta\eta| < 1.7$. Figure 76 demonstrates the dependence of V_2, V_3, and V_3/V_2. Figure 77 shows the same for V_1, V_4, and V_5. The relative uncertainty in V_1—V_5, and V_3/V_2 is shown in Table XV. In some V_n, there seems to be a slight downward trend for pion triggers, but it affects V_2 and V_3 in the same way and all but cancels out in V_3/V_2. For V_2 and V_3 the source was nevertheless investigated as a sanity check, and found to be due to the fitter being better able to separate jet-like cone from $\Delta\eta$-independent terms with larger fitting ranges. Figure 78 shows overlaid dashed lines where the jet cone

Appendix B (Continued)

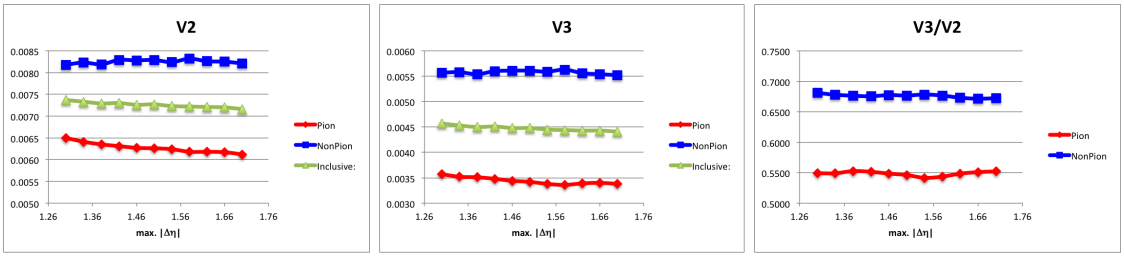

Figure 76. Left to right: $\Delta\eta$ range dependence of V_2, V_3, and V_3/V_2 from "Vn" fit.

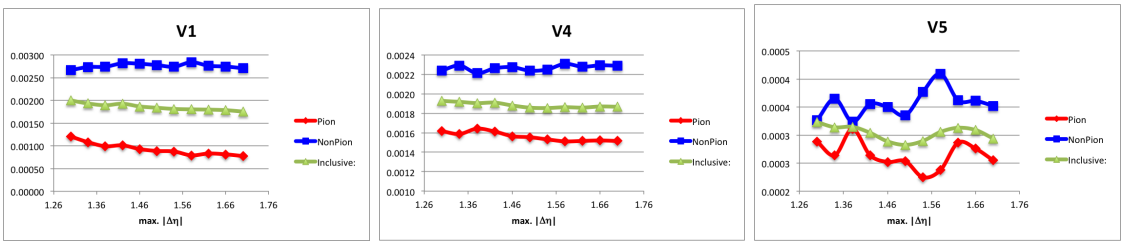

Figure 77. Left to right: $\Delta\eta$ range dependence of V_1, V_4, and V_5 from "Vn" fit.

generalized gaussian parameters were fixed to the values from the standard fitting range. As a result, the fitting range dependency all but vanishes. With the trend understood, the full standard deviation without fixing jet cone parameters for the systematic uncertainty was used. The same assessment for the "mini-jet" fit model is shown in Table Table XVI and Figure Figure 79.

Appendix B (Continued)

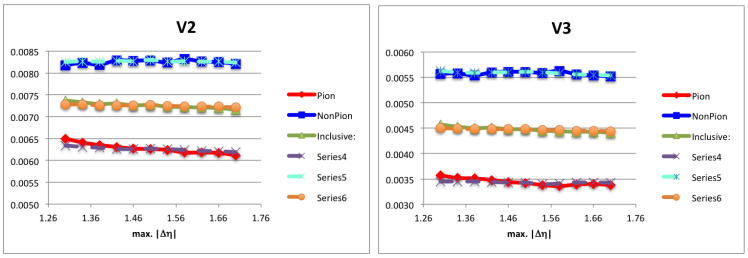

Figure 78. $\Delta\eta$ range dependence of V_2 and V_3 from "Vn" fit. Dashed curves indicate fixed jet cone gaussian values.

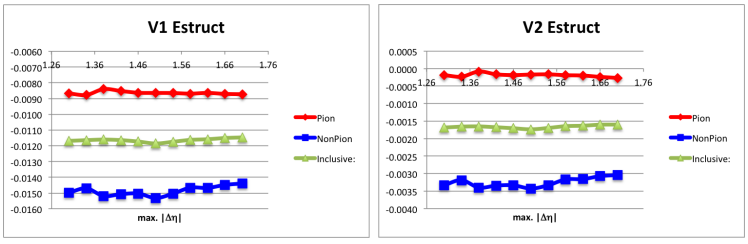

Figure 79. $\Delta\eta$ range dependence of V_1 and V_2 from "mini-jet" fit.

Appendix B (Continued)

Trigger	$\sigma(V_1)/\langle V_1\rangle$	$\sigma(V_2)/\langle V_2\rangle$	$\sigma(V_3)/\langle V_3\rangle$	$\sigma(V_4)/\langle V_4\rangle$	$\sigma(V_5)/\langle V_5\rangle$	$\langle V_3/V_2\rangle$	$\sigma(V_3/V_2)/\langle V_3/V_2\rangle$
π	15%	1.8%	2.1%	3.0%	9.6%	0.548	0.7%
P+K	1.8%	0.5%	0.7%	1.3%	7.2%	0.680	0.4%
All	4.1%	0.9%	1.1%	1.4%	4.6%	0.621	0.2%

TABLE XV

Uncertainty on Fourier coefficients and V_3/V_2 from "V_n" fits due to variation of the $\Delta\eta$ fit range.

Trigger	$\sigma(V_1)/\langle V_1\rangle$	$\sigma(V_2)/\langle V_2\rangle$
π	1.2%	28%
P+K	1.9%	3.9%
All	0.9%	2.4%

TABLE XVI

Uncertainty on V_1 and V_2 from "mini-jet" fits due to variation of the $\Delta\eta$ fit range. The large relative uncertainty on V_2 for π triggers is a consequence of the almost vanishing value.

Appendix C

FEED-DOWN ESTIMATE

Trigger contamination from neutral decays cannot be subtracted. However, the effect can be estimated. Due to decay kinematics, only protons from $\Lambda \to p\pi$ can have a potential effect, K_0^S decays to pions in the trigger range would require a much higher K_0^S p_T which is strongly suppressed by the steeply falling spectrum.

Using a two-body decay simulation, the proton is found to carry on average about 90% of the Λ momentum and closely preserves the original direction, see Figure 80. This simulation was primed with published $\Lambda + \bar{\Lambda}$ and $p + \bar{p}$ spectra [8, 189], taking care to scale protons to the same reference multiplicity, and reducing the Λ spectra by 35% to account for the branching ratio to neutral products. In the trigger p_T range, about 9.5% of protons come from Λ decays; this is reduced further by about 10% due to the tight `DCA` cut, and by the presence of kaons in the non-pion sample. Ultimately, we estimate about 5% contamination of decay protons in the non-pion triggers.

Effect

Jet-like yield Λ-h correlations show, within large uncertainties, that jet-like yield correlated with Λ is comparable to h-h [190]. The decay protons correspond to a "true" average leading particle p_T of 4.9 GeV/c instead of 4.36 GeV/c found for inclusive triggers. As shown below in Figure 58, one would expect about 20% yield increase

Appendix C (Continued)

due to this shift. Combined with the low contamination, the effect on jet-like yield is estimated to be less than 1%.

Ridge While the expected effect is model-dependent, the almost non-existent axis shift and the expected p_T-independence of v_n in the trigger range make any measurable effect on the $\Delta\eta$-independent terms unlikely. Furthermore, no difference between protons and Λ would be expected within the n_{q} scaling assumption.

Appendix C (Continued)

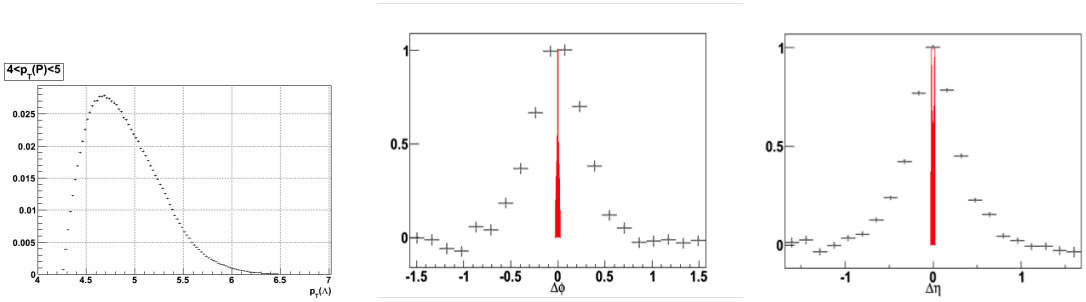

Figure 80. From two-body decay simulation. Left: p_T distribution of Λ decaying to protons in the trigger range 4-5 GeV/c. Middle and right: Difference between Λ and proton axis in ϕ and η. Scaled pure cone is shown for comparison.

CITED LITERATURE

1. Snellings, R.: Elliptic flow: a brief review. New J. Phys., 13(5):055008, May 2011.

2. Collaboration, T. U.: UrQMD Animations. arXiv:0805.4411 [nucl-ex]. Website.

3. Jacak, B. V. and Müller, B.: The exploration of hot nuclear matter. Science, 337(6092):310–4, July 2012.

4. Alver, B., Back, B., Baker, M., et al.: Importance of correlations and fluctuations on the initial source eccentricity in high-energy nucleus-nucleus collisions. Phys. Rev. C, 77(1):014906, January 2008.

5. Alver, B. and Roland, G.: Collision-geometry fluctuations and triangular flow in heavy-ion collisions. Phys. Rev. C, 81(5):054905, May 2010.

6. Schenke, B., Tribedy, P., and Venugopalan, R.: Fluctuating Glasma Initial Conditions and Flow in Heavy Ion Collisions. Phys. Rev. Lett., 108(25):252301, June 2012.

7. Gale, C., Jeon, S., Schenke, B., Tribedy, P., and Venugopalan, R.: Event-by-Event Anisotropic Flow in Heavy-ion Collisions from Combined Yang-Mills and Viscous Fluid Dynamics. Phys. Rev. Lett., 110(1):012302, January 2013.

8. Abelev, B. I. et al.: Identified baryon and meson distributions at large transverse momenta from Au + Au collisions at $\sqrt{s_{NN}} = 200$ GeV. Phys. Rev. Lett., 97:152301, Oct 2006.

9. eds. S. Sarkar, H. Satz, and B. Sinha The Physics of the Quark-Gluon Plasma, volume 785 of Lecture Notes in Physics. Berlin, Heidelberg, Springer Berlin Heidelberg, 2010.

10. Albino, S., Kniehl, B., and Kramer, G.: Fragmentation functions for light charged hadrons with complete quark flavor separation. Nucl. Phys. B, 725:181–206, 2005.

11. Mohanty, B.: Search for color charge dependence of energy loss at rhic. In Proceedings of the 23rd Winter Workshop on Nuclear Dynamics, May 2007.

12. Horner, M.: Systematic Studies of Low- and Intermediate-pT Correlated Angular Distributions in Au+Au Collisions at $\sqrt{s_{NN}} = 200GeV$ from the STAR Experiment. Doctoral dissertation, University of Cape Town, 2007. Implementation at /star/u/mvl/mark_dihadr/StRoot/StMJNHEffOracle.

13. Back, B., Baker, M., Barton, D., et al.: The phobos detector at rhic. Nucl. Instrum. Meth. A, 499(2-3):603–623, March 2003.

14. PHOBOS Event Display. http://www.c-ad.bnl.gov/esfd/RMEM/Run7224_Event5261_3.gif.

15. PHOBOS and BRAHMS detectors. http://www.bnl.gov/rhic/PHOBOS_BRAHMS.asp.

16. Adamczyk, M. et al.: The BRAHMS experiment at RHIC. Nucl.Instrum.Meth., A499:437–468, 2003.

17. Adamczyk, L., Agakishiev, G., Aggarwal, M., et al.: Single spin asymmetry in polarized proton–proton elastic scattering at. Phys. Lett. B, 719(1-3):62–69, February 2013.

18. Nogach, L.: A feasibility experiment at RHIC to measure the analyzing power for Drell-Yan production (A_NDY). In Proceedings of DSPIN-2011, 2011.

19. Mechanical Specifications For PHENIX Central Magnet Region Detector Upgrades. http://www.phenix.bnl.gov/WWW/INTEGRTN/ME&Integration/mechanical_specifications.htm.

20. Mitchell, J.: PHENIX Event Display. http://www.phenix.bnl.gov/~mitchell/physics/index.html.

21. Sakuma, T.: Sketchup star. https://drupal.star.bnl.gov/STAR/SketchUpSTAR, 2012.

22. Collaboration, S.: Star tpc photographs and drawings. http://www.star.bnl.gov/public/tpc/photos/tpc_photos.html, 2012.

23. Shao, M., Barannikova, O., Dong, X., et al.: Extensive particle identification with TPC and TOF at the STAR experiment. Nucl. Instruments Methods Phys. Res. Sect. A Accel. Spectrometers, Detect. Assoc. Equip., 558(2):419–429, March 2006.

24. Judd, E.: STAR Trigger Introduction. http://www.star.bnl.gov/public/trg/trouble/operating-trigger/introduction/.

25. Agakishiev, G. et al.: System size and energy dependence of near-side dihadron correlations. Phys. Rev. C, 85:014903, Jan 2012.

26. RHIC Scientists Serve Up "Perfect" Liquid. http://www.bnl.gov/rhic/news2/news.asp?a=303&t=pr. Announcement.

27. New State of Matter created at CERN. http://press.web.cern.ch/press-releases/2000/02/new-state-matter-created-cern. Press Release.

28. Heinz, U. and Jacob, M.: Evidence for a New State of Matter: An Assessment of the Results from the CERN Lead Beam Programme. arXiv:nucl-th/0002042, February 2000. e-Print.

29. Arsene, I., Bearden, I., Beavis, D., et al.: Evolution of the Nuclear Modification Factors with Rapidity and Centrality in d+Au Collisions at $\sqrt{s_{NN}} = 200$ GeV. Phys. Rev. Lett., 93(24):242303, December 2004.

30. Back, B., Baker, M., Ballintijn, M., et al.: The PHOBOS perspective on discoveries at RHIC. Nucl. Phys. A, 757(1-2):28–101, August 2005.

31. Adams, J., Aggarwal, M., Ahammed, Z., et al.: Experimental and theoretical challenges in the search for the quark–gluon plasma: The STAR Collaboration's critical assessment of the evidence from RHIC collisions. Nucl. Phys. A, 757(1-2):102–183, August 2005.

32. Adcox, K., Adler, S., Afanasiev, S., et al.: Formation of dense partonic matter in relativistic nucleus–nucleus collisions at RHIC: Experimental evaluation by the PHENIX Collaboration. Nucl. Phys. A, 757(1):184–283, 2005.

33. Gyulassy, M.: The QGP Discovered at RHIC. In Proceedings, NATO Adv. Study Inst. Struct. Dyn. Elem. Matter, pages 159–182, March 2004.

34. Collins, J. C. and Perry, M. J.: Superdense Matter: Neutrons or Asymptotically Free Quarks? Phys. Rev. Lett., 34(21):1353–1356, May 1975.

35. Chapline, G. and Nauenberg, M.: Asymptotic freedom and the baryon-quark phase transition. Phys. Rev. D, 16(2):450–456, July 1977.

36. Freedman, B. and McLerran, L.: Fermions and gauge vector mesons at finite temperature and density. III. The ground-state energy of a relativistic quark gas. Phys. Rev. D, 16(4):1169–1185, August 1977.

37. Community, T. U. R. H.-I.: Hot and Dense QCD Matter Unraveling the Mysteries of the Strongly Interacting Quark-Gluon-Plasma, 2012. Response to the request for comments by the NSAC Subcommittee (Tribble Committee).

38. Venugopalan, R.: From many body wee parton dynamics to perfect fluid: a standard model for heavy ion collisions. arXiv:1012.4699 [hep-ph], December 2010. e-Print.

39. RHIC Collider-Accelerator Division: Configuration Manual. http://www.bnl.gov/cad/accelerator/docs/pdf/RHICConfManual.pdf, 2006.

40. Miller, M. L., Reygers, K., Sanders, S. J., and Steinberg, P.: Glauber Modeling in High-Energy Nuclear Collisions. Annu. Rev. Nucl. Part. Sci., 57(1):205–243, November 2007.

41. Ackermann, K., Adams, N., Adler, C., et al.: STAR detector overview. Nucl. Instruments Methods Phys. Res. Sect. A Accel. Spectrometers, Detect. Assoc. Equip., 499(2-3):624–632, March 2003.

42. Adcox, K., Adler, S., Aizama, M., et al.: PHENIX detector overview. Nucl. Instruments Methods Phys. Res. Sect. A Accel. Spectrometers, Detect. Assoc. Equip., 499(2-3):469–479, March 2003.

43. Lee, Y., Debbe, R., Lee, J., Ito, H., and Sanders, S.: Plastic scintillator centrality detector for BRAHMS. Nucl. Instruments Methods Phys. Res. Sect. A Accel. Spectrometers, Detect. Assoc. Equip., 516(2-3):281–287, January 2004.

44. Chatrchyan, S., Khachatryan, V., Sirunyan, A. M., et al.: Measurement of the Pseudorapidity and Centrality Dependence of the Transverse Energy Density in Pb-Pb Collisions at $\sqrt{s_{NN}} = 2.76$ TeV. Phys. Rev. Lett., 109(15):152303, October 2012.

45. Aad, G., Abbott, B., Abdallah, J., et al.: Observation of a Centrality-Dependent Dijet Asymmetry in Lead-Lead Collisions at $\sqrt{s_{NN}} =$ TeV with the ATLAS Detector at the LHC. Phys. Rev. Lett., 105(25):252303, December 2010.

46. Star Collaboration: Studying the Phase Diagram of QCD Matter at RHIC. Technical Report June, Star Collaboration, 2014.

47. Karsch, F., Laermann, E., and Peikert, A.: Quark mass and flavour dependence of the QCD phase transition. Nucl. Phys. B, 605(1-3):579–599, July 2001.

48. Braun-Munzinger, P. and Stachel, J.: The quest for the quark-gluon plasma. Nature, 448:302–309, 2007.

49. Karsch, F.: Lattice results on QCD thermodynamics. Nucl. Phys. A, 698(1-4):199–208, February 2002.

50. Petreczky, P.: Lattice QCD at non-zero temperature. J. Phys. G Nucl. Part. Phys., 39(9):093002, September 2012.

51. Borsányi, S., Fodor, Z., Hoelbling, C., et al.: Full result for the QCD equation of state with flavors. Phys. Lett. B, 730(1):99–104, March 2014.

52. Borsányi, S., Fodor, Z., Hoelbling, C., et al.: Is there still any T_c mystery in lattice QCD? Results with physical masses in the continuum limit III. arXiv:1005.3508 [hep-lat], May 2010. e-Print.

53. Bazavov, A., Bhattacharya, T., Cheng, M., et al.: Chiral and deconfinement aspects of the QCD transition. Phys. Rev. D, 85(5):054503, March 2012.

54. Heyde, K.: Basic Ideas and Concepts in Nuclear Physics: An Introductory Approach, Third Edition. CRC Press; 3 edition, 2004.

55. Bjorken, J. D.: Highly relativistic nucleus-nucleus collisions: The central rapidity region. Phys. Rev. D, 27(1):140–151, January 1983.

56. Arsene, I., Bearden, I., Beavis, D., et al.: Quark–gluon plasma and color glass condensate at RHIC? The perspective from the BRAHMS experiment. Nucl. Phys. A, 757(1):1–27, 2005.

57. Adare, A., Afanasiev, S., Aidala, C., et al.: Detailed measurement of the e^{+}e^{-} pair continuum in p+p and Au+Au collisions at $\sqrt{s_{NN}}$=200 GeV and implications for direct photon production. Phys. Rev. C, 81(3):034911, March 2010.

58. Glauber, R.: Cross Sections in Deuterium at High Energies. Phys. Rev., 100(1):242–248, October 1955.

59. Franco, V. and Glauber, R.: High-Energy Deuteron Cross Sections. Phys. Rev., 142(4):1195–1214, February 1966.

60. Białłas, A., Bleszyński, M., and Czyż, W.: Multiplicity distributions in nucleus-nucleus collisions at high energies. Nucl. Phys. B, 111(3):461–476, September 1976.

61. Glauber, R. J.: Quantum Optics and Heavy Ion Physics. Nucl. Phys. A, 774:3–13, August 2006.

62. Bzdak, A.: Heavy ion collisions in the used nucleon model. Phys. Lett. B, 647(5-6):358–360, April 2007.

63. Alver, B., Baker, M., Loizides, C., and Steinberg, P.: The PHOBOS Glauber Monte Carlo. arXiv:0805.4411 [nucl-ex], May 2008. e-Print.

64. Adler, S., Afanasiev, S., Aidala, C., et al.: Absence of Suppression in Particle Production at Large Transverse Momentum in $\sqrt{s_{NN}}$ = 200 GeV d+Au Collisions. Phys. Rev. Lett., 91(7):072303, August 2003.

65. Adams, J., Adler, C., Aggarwal, M. M., et al.: Transverse-Momentum and Collision-Energy Dependence of High-p_{T} Hadron Suppression in Au+Au Collisions at Ultrarelativistic Energies. Phys. Rev. Lett., 91(17):172302, October 2003.

66. Back, B., Baker, M., Ballintijn, M., et al.: Centrality Dependence of Charged-Hadron Transverse-Momentum Spectra in d+Au Collisions at sNN=200 GeV. Phys. Rev. Lett., 91(7):072302, August 2003.

67. Abelev, B. et al.: Systematic Measurements of Identified Particle Spectra in pp, d+Au and Au+Au Collisions from STAR. Phys. Rev. C, 79:034909, 2009.

68. Cartiglia, N.: Measurement of the proton-proton total, elastic, inelastic and diffractive cross sections at 2, 7, 8 and 57 TeV. arXiv:1305.6131 [hep-ex], May 2013.

69. De Vries, H., De Jager, C., and De Vries, C.: Nuclear charge-density-distribution parameters from elastic electron scattering. At. Data Nucl. Data Tables, 36(3):495–536, May 1987.

70. Hofmann, J., Stoecker, H., Scheid, W., Greiner, W., and Mountoin, B.: Possibility of nuclear shock waves in relativistic heavy ion collisions. In Rep. Work. BEV/NUCLEON COLLISIONS HEAVY IONS - HOW WHY, volume 50445, pages 39–48, 1974.

71. Gyulassy, M., Frankel, K., and Stöcker, H.: Do nuclei flow at high energies? Phys. Lett. B, 110(3-4):185–188, April 1982.

72. Ollitrault, J.-Y.: Anisotropy as a signature of transverse collective flow. Phys. Rev. D, 46(1):229–245, Jul 1992.

73. Voloshin, S. A., Poskanzer, A. M., and Snellings, R.: Collective phenomena in non-central nuclear collisions. arXiv:0809.2949 [nucl-ex], September 2008. e-Print.

74. Poskanzer, A. M. and Voloshin, S. A.: Methods for analyzing anisotropic flow in relativistic nuclear collisions. Phys. Rev. C, 58(3):1671–1678, September 1998.

75. Luzum, M.: Collective flow and long-range correlations in relativistic heavy ion collisions. Phys. Lett. B, 696(5):499–504, February 2011.

76. Wang, S., Jiang, Y., Liu, Y., et al.: Measurement of collective flow in heavy-ion collisions using particle-pair correlations. Phys. Rev. C, 44(3):1091–1095, September 1991.

77. Borghini, N., Dinh, P. M., and Ollitrault, J.-y.: Flow analysis from cumulants: a practical guide. arXiv:nucl-ex/0110016, October 2001. e-Print.

78. Bhalerao, R., Borghini, N., and Ollitrault, J.-Y.: Analysis of anisotropic flow with Lee–Yang zeroes. Nucl. Phys. A, 727(3-4):373–426, November 2003.

79. Lin, Z.-W., Ko, C. M., Li, B.-A., Zhang, B., and Pal, S.: Multiphase transport model for relativistic heavy ion collisions. Phys. Rev. C, 72(6):064901, December 2005.

80. Ackermann, K., Adams, N., Adler, C., et al.: Elliptic Flow in Au+Au Collisions at $\sqrt{s_{NN}} = 130$ GeV. Phys. Rev. Lett., 86(3):402–407, January 2001.

81. Poskanzer, A., Voloshin, S., Bächler, J., et al.: Centrality dependence of directed and elliptic flow at the SPS. Nucl. Phys. A, 661(1-4):341–344, December 1999.

82. Kolb, P. F. and Heinz, U.: Hydrodynamic description of ultrarelativistic heavy-ion collisions. arXiv:nucl-th/0305084, May 2003. e-Print.

83. Luzum, M. and Romatschke, P.: Conformal relativistic viscous hydrodynamics: Applications to RHIC results at $\sqrt{s_{NN}}$=200 GeV. Phys. Rev. C, 78(3):034915, September 2008.

84. Teaney, D. A.: Viscous Hydrodynamics and the Quark Gluon Plasma. arXiv:0905.2433 [nucl-th], May 2009. e-Print.

85. Kovtun, P., Son, D., and Starinets, A.: Viscosity in Strongly Interacting Quantum Field Theories from Black Hole Physics. Phys. Rev. Lett., 94(11):111601, March 2005.

86. Abelev, B. et al.: Mass, quark-number, and $\sqrt{s_{NN}}$ dependence of the second and fourth flow harmonics in ultra-relativistic nucleus-nucleus collisions. Phys. Rev. C, 75:054906, 2007.

87. Adare, A. et al.: Scaling properties of azimuthal anisotropy in Au + Au and Cu + Cu collisions at $\sqrt{s_{\rm NN}} = 200$ GeV. Phys. Rev. Lett., 98:162301, Apr 2007.

88. Csanád, M., Csörgő, T., Ster, A., et al.: Universal scaling of the elliptic flow data at RHIC. Eur. Phys. J. A, 38(3):363–368, November 2008.

89. Adamczyk, L. et al.: Third harmonic flow of charged particles in Au + Au collisions at $\sqrt{s_{NN}}$=200 GeV. Phys. Rev. C 88,, 014904, 2013.

90. Adare, A., Afanasiev, S., Aidala, C., et al.: Measurements of Higher Order Flow Harmonics in Au+Au Collisions at $\sqrt{s_{NN}}$=200 GeV. Phys. Rev. Lett., 107(25):252301, December 2011.

91. Abelev, B., Adam, J., Adamová, D., et al.: Anisotropic flow of charged hadrons, pions and (anti-)protons measured at high transverse momentum in Pb–Pb collisions at. Phys. Lett. B, 719(1-3):18–28, February 2013.

92. Aad, G., Abajyan, T., Abbott, B., et al.: Measurement of the distributions of event-by-event flow harmonics in lead-lead collisions at $\sqrt{s_{NN}} = 2.76$ TeV with the ATLAS detector at the LHC. J. High Energy Phys., 2013(11):183, November 2013.

93. Chatrchyan, S., Khachatryan, V., Sirunyan, a. M., et al.: Measurement of higher-order harmonic azimuthal anisotropy in PbPb collisions at sNN=2.76 TeV. Phys. Rev. C, 89(4):044906, April 2014.

94. Drescher, H.-J. and Nara, Y.: Effects of fluctuations on the initial eccentricity from the color glass condensate in heavy ion collisions. Phys. Rev. C, 75(3):034905, March 2007.

95. Jamal, J.-M. and Kovchegov, Y. V.: Saturation physics and deuteron–gold collisions at RHIC. Prog. Part. Nucl. Phys., 56(1):104–231, January 2006.

96. Lacey, R.: PHENIX measurements of higher order flow harmonics in Au+Au collisions at $\sqrt{s_{NN}} = 200$ GeV. J. Phys. G Nucl. Part. Phys., 38(12):124048, December 2011.

97. Adcox, K., Adler, S., Ajitanand, N., et al.: Centrality Dependence of π+/-, K+/-, p, and $\bar{p}$ Production from sNN=130 GeV Au + Au Collisions at RHIC. Phys. Rev. Lett., 88(24):242301, May 2002.

98. Abelev, B. et al.: Energy dependence of pi+-, p and anti-p transverse momentum spectra for Au+Au collisions at s(NN)**(1/2) = 62.4 and 200-GeV. Phys. Lett. B, 655:104–113, 2007.

99. Agakishiev, G., Aggarwal, M. M., Ahammed, Z., et al.: Strangeness Enhancement in Cu-Cu and Au-Au Collisions at $\sqrt{s_{NN}}$=200 GeV. Phys. Rev. Lett., 108(7):072301, February 2012.

100. Hwa, R. C. and Yang, C. B.: Recombination of shower partons at high p_T in heavy-ion collisions. Phys. Rev. C, 70:024905, Aug 2004.

101. Fries, R. J., Müller, B., Nonaka, C., and Bass, S. A.: Hadron production in heavy ion collisions: Fragmentation and recombination from a dense parton phase. Phys. Rev. C, 68:044902, Oct 2003.

102. Hwa, R. C.: Hadron Correlations in Jets and Ridges through Parton Recombination. e-Print, 2009.

103. Fries, R. J.: Hadron Correlations and Parton Recombination. Nucl. Phys. A, 783:125–132, 2007.

104. Andersson, B., Gustafson, G., Ingelman, G., and Sjöstrand, T.: Parton fragmentation and string dynamics. Phys. Rep., 97:31–145, 1983.

105. Sjöstrand, T., Mrenna, S., and Skands, P.: A brief introduction to PYTHIA 8.1. Comput. Phys. Commun., 178(11):852–867, June 2008.

106. Arsene, I., Bearden, I., Beavis, D., et al.: Transverse-Momentum Spectra in Au+Au and d+Au Collisions at sNN=200 GeV and the Pseudorapidity Dependence of High-pT Suppression. Phys. Rev. Lett., 91(7):072305, August 2003.

107. Gyulassy, M., Vitev, I., Wang, X.-n., and Zhang, B.-w.: Jet Quenching and Radiative Energy Loss in Dense Nuclear Matter. arXiv:nucl-th/0302077, February 2003. e-Print.

108. D'Enterria, D.: QCD hard scattering results from PHENIX at RHIC. arXiv:nucl-ex/0401001, January 2004. e-Print.

109. Adler, S., Afanasiev, S., Aidala, C., et al.: Common Suppression Pattern of η and $\pi 0$ Mesons at High Transverse Momentum in Au+Au Collisions at sNN=200 GeV. Phys. Rev. Lett., 96(20):202301, May 2006.

110. Adams, J., Adler, C., Aggarwal, M., et al.: Evidence from d+Au Measurements for Final-State Suppression of High-pT Hadrons in Au+Au Collisions at RHIC. Phys. Rev. Lett., 91(7):072304, August 2003.

111. Adams, J., Adler, C., Aggarwal, M. M., et al.: Distributions of Charged Hadrons Associated with High Transverse Momentum Particles in pp and Au+Au Collisions at $\sqrt{s_{NN}} = 200$ GeV. Phys. Rev. Lett., 95(15):152301, October 2005.

112. Agakishiev, H. et al.: Experimental studies of di-jet survival and surface emission bias in $\mathbf{Au + Au}$ collisions via angular correlations with respect to back-to-back leading hadrons. Phys. Rev. C, 83:061901, Jun 2011.

113. Adamczyk, L. et al.: Experimental studies of di-jets in au + au collisions using angular correlations with respect to back-to-back leading hadrons. Phys. Rev. C, 87:044903, Apr 2013.

114. Adamczyk, L. et al.: Jet-hadron correlations in $\sqrt{s_{NN}} = 200$ gev au+au and p+p collisions. Phys. Rev. Lett., 112:122301, 2014.

115. Renk, T.: Using hard dihadron correlations to constrain elastic energy loss. Phys. Rev. C, 84(6):067902, December 2011.

116. Horner, M. J.: Low- and Intermediate-$_T$ Di-hadron Distributions in Au+Au Collisions at $\sqrt{s_{NN}}$ GeV from STAR. J. Phys. G Nucl. Part. Phys., 34(8):4, January 2007.

117. Abelev, B. I., Aggarwal, M. M., Ahammed, Z., et al.: Long range rapidity correlations and jet production in high energy nuclear collisions. Phys. Rev. C, 80(6):064912, December 2009.

118. Wong, C.-Y.: Momentum kick model description of the near-side ridge and jet quenching. Phys. Rev. C, 78(6):064905, December 2008.

119. Pantuev, V. S.: "Jet-Ridge" effect in heavy ion collisions as a back splash from stopped parton. arXiv:0710.1882 [hep-ph], October 2007. e-Print.

120. Gavin, S., McLerran, L., and Moschelli, G.: Long range correlations and the soft ridge in relativistic nuclear collisions. Phys. Rev. C, 79(5):051902, May 2009.

121. Dumitru, A., Gelis, F., McLerran, L., and Venugopalan, R.: Glasma flux tubes and the near side ridge phenomenon at RHIC. Nucl. Phys. A, 810(1-4):91–108, September 2008.

122. Majumder, a., Müller, B., and Bass, S.: Longitudinal Broadening of Quenched Jets in Turbulent Color Fields. Phys. Rev. Lett., 99(4):042301, July 2007.

123. Pruneau, C. A., Gavin, S., and Voloshin, S. A.: Transverse radial flow effects on two- and three-particle angular correlations. Nucl. Phys. A, 802(1-4):107–121, April 2008.

124. Hwa, R. C.: Hadron Correlations in Jets and Ridges through Parton Recombination. arXiv:0904.2159 [nucl-th], April 2009. e=Print.

125. Chiu, C. B. and Hwa, R. C.: Pedestal and peak structure in jet correlation. Phys. Rev. C, 72(3):034903, September 2005.

126. Shuryak, E.: Origin of the "ridge" phenomenon induced by jets in heavy ion collisions. Phys. Rev. C, 76(4):047901, October 2007.

127. Nagle, J.: Ridge, Bulk, and Medium Response: How to Kill Models and Learn Something in the Process. Nucl. Phys. A, 830(1-4):147c–154c, November 2009.

128. Khachatryan, V. et al.: Observation of long-range, near-side angular correlations in proton-proton collisions at the lhc. Journal of High Energy Physics, 2010(9):1–38, 2010.

129. Chatrchyan, S. et al.: Observation of long-range near-side angular correlations in proton-lead collisions at the LHC. Phys. Lett. B, 718, 2013.

130. Aad, G. et al.: Measurement with the ATLAS detector of multi-particle azimuthal correlations in p+Pb collisions at $\sqrt{s_{NN}}$=5.02 TeV. Phys. Lett. B, 725:60–78, 2013.

131. Brown, K. A., Ahrens, L., Bai, M., et al.: RHIC PERFORMANCE FOR FY'10 200 GeV Au + Au HEAVY ION RUN. In Proceedings of IPAC'10, pages 507–509, 2010.

132. Gardner, C. J., Abreu, N. P., Ahrens, L., et al.: SETUP AND PERFORMANCE OF RHIC FOR THE 2008 RUN WITH DEUTERON-GOLD COLLISIONS. In Proceedings of EPAC08, pages 2548–2550, 2008.

133. Busza, W.: Wit Busza Interview - Special Topic of Hadron Colliders. http://archive.sciencewatch.com/ana/st/hadron/11aprSThadBNL/, 2010.

134. Wozniak, K. et al.: Vertex reconstruction algorithms in the PHOBOS experiment at RHIC. Nucl. Instrum. Meth., A566:185–189, 2006.

135. Wozniak, K.: Study of the quark-gluon matter by the PHOBOS experiment. arXiv:0809.2893 [nucl-ex], September 2008. Talk at the Hadron Structure and QCD 2008, Gatchina.

136. Back, B. et al.: Charged particle multiplicity near mid-rapidity in central Au + Au collisions at $S^{(1/2)}$ = 56-A/GeV and 130-A/GeV. Phys.Rev.Lett., 85:3100–3104, 2000.

137. Back, B., Baker, M., Barton, D., et al.: Charged-Particle Pseudorapidity Density Distributions from Au+Au Collisions at $\sqrt{s_{NN}} = 130$ GeV. Phys. Rev. Lett., 87(10):102303, August 2001.

138. Videbaek, F.: Flemming Videbaek Interview - Special Topic of Hadron Colliders. http://archive.sciencewatch.com/ana/st/hadron/11febSThadBNL/, 2010.

139. Bültmann, S., Chen, W., Chiang, I., et al.: The PP2PP experiment at RHIC: silicon detectors installed in Roman Pots for forward proton detection close to the beam. Nucl. Instruments Methods Phys. Res. Sect. A Accel. Spectrometers, Detect. Assoc. Equip., 535(1-2):415–420, December 2004.

140. Bland, L. C.: Measurement of Forward Jets at RHIC. In QCD Evolution Workshop (QCD2013), page 9, August 2013.

141. Jacak, B.: Barbara Jacak Interview - Special Topic of Hadron Colliders. http://archive.sciencewatch.com/ana/st/hadron/11marSThad_BNL/, 2010.

142. Adler, S. S. et al.: PHENIX on-line and off-line computing. Nucl.Instrum.Meth., A499:593–602, 2003.

143. Adler, S. S. et al.: PHENIX on-line systems. Nucl.Instrum.Meth., A499:560–592, 2003.

144. Allen, M. et al.: PHENIX inner detectors. Nucl.Instrum.Meth., A499:549–559, 2003.

145. Akikawa, H. et al.: PHENIX muon arms. Nucl.Instrum.Meth., A499:537–548, 2003.

146. Aphecetche, L. et al.: PHENIX calorimeter. Nucl.Instrum.Meth., A499:521–536, 2003.

147. Aizawa, M. et al.: PHENIX central arm particle ID detectors. Nucl.Instrum.Meth., A499:508–520, 2003.

148. Adcox, K. et al.: PHENIX central arm tracking detectors. Nucl.Instrum.Meth., A499:489–507, 2003.

149. Aronson, S. et al.: PHENIX magnet system. Nucl.Instrum.Meth., A499:480–488, 2003.

150. Adcox, K. et al.: PHENIX detector overview. Nucl.Instrum.Meth., A499:469–479, 2003.

151. Novitzky, N.: STUDY OF THE NEUTRAL PION AND DIRECT PHOTON PRODUCTION IN AU+AU COLLISIONS AT $\sqrt{s_{NN}} = 39 - 200$ GeV. Doctoral dissertation, University of Jyväskylä, 2013.

152. Vazquez, E.: Control study of two-particle correlations in heavy ion collisions at RHIC-PHENIX. Doctoral dissertation, Columbia University, 2013.

153. Ding, L.: Measurement of heavy flavor electron flow in Au + Au collisions at $\sqrt{s_{NN}} =$ 62.4 GeV. Doctoral dissertation, Iowa State University, 2013.

154. Adler, S., Afanasiev, S., Aidala, C., et al.: Suppressed $\pi 0$ Production at Large Transverse Momentum in Central Au+Au Collisions at $\sqrt{s_{NN}} = 200$ GeV. Phys. Rev. Lett., 91(7):072301, August 2003.

155. Bergsma, F., Blyth, C., Brown, R., et al.: The STAR detector magnet subsystem. Nucl. Instruments Methods Phys. Res. Sect. A Accel. Spectrometers, Detect. Assoc. Equip., 499(2-3):633–639, March 2003.

156. Anderson, M., Berkovitz, J., Betts, W., et al.: The STAR time projection chamber: a unique tool for studying high multiplicity events at

RHIC. Nucl. Instruments Methods Phys. Res. Sect. A Accel. Spectrometers, Detect. Assoc. Equip., 499(2-3):659–678, March 2003.

157. Bichsel, H.: A method to improve tracking and particle identification in TPCs and silicon detectors. Nucl. Instruments Methods Phys. Res. Sect. A Accel. Spectrometers, Detect. Assoc. Equip., 562(1):154–197, June 2006.

158. Anderson, M., Bieser, F., Bossingham, R., et al.: A readout system for the STAR time projection chamber. Nucl. Instruments Methods Phys. Res. Sect. A Accel. Spectrometers, Detect. Assoc. Equip., 499(2-3):679–691, March 2003.

159. Kotchenda, L., Kozlov, S., Kravtsov, P., et al.: STAR TPC gas system. Nucl. Instruments Methods Phys. Res. Sect. A Accel. Spectrometers, Detect. Assoc. Equip., 499(2-3):703–712, March 2003.

160. Ackermann, K., Bieser, F., Brady, F., et al.: The forward time projection chamber in STAR. Nucl. Instruments Methods Phys. Res. Sect. A Accel. Spectrometers, Detect. Assoc. Equip., 499(2-3):713–719, March 2003.

161. Llope, W. J., Geurts, F., Mitchell, J. W., et al.: The TOFp/pVPD time-of-flight system for STAR. Nucl. Instruments Methods Phys. Res. Sect. A Accel. Spectrometers, Detect. Assoc. Equip., 522(3):252–273, April 2004.

162. Llope, W.: Multigap RPCs in the STAR experiment at RHIC. Nucl. Instruments Methods Phys. Res. Sect. A Accel. Spectrometers, Detect. Assoc. Equip., 661:S110–S113, January 2012.

163. Llope, W. J., Zhou, J., Nussbaum, T., et al.: The STAR Vertex Position Detector. arXiv:1403.6855 [physics.ins-det], March 2014.

164. Beddo, M., Bielick, E., Fornek, T., et al.: The STAR Barrel Electromagnetic Calorimeter. Nucl. Instruments Methods Phys. Res. Sect. A Accel. Spectrometers, Detect. Assoc. Equip., 499(2-3):725–739, March 2003.

165. Allgower, C., Anderson, B., Baldwin, A., et al.: The STAR endcap electromagnetic calorimeter. Nucl. Instruments Methods Phys. Res. Sect. A Accel. Spectrometers, Detect. Assoc. Equip., 499(2-3):740–750, March 2003.

166. Bellwied, R., Beuttenmuller, R., Caines, H., et al.: The STAR Silicon Vertex Tracker: A large area Silicon Drift Detector. Nucl. Instruments Methods Phys. Res. Sect. A Accel. Spectrometers, Detect. Assoc. Equip., 499(2-3):640–651, March 2003.

167. Zhang, Y., Bouchet, J., Dong, X., Margetis, S., and Ritter, H. G.: Study of bottom production with the STAR Heavy Flavor Tracker. J. Phys. G Nucl. Part. Phys., 41(2):025103, February 2014.

168. Yang, C., Huang, X. J., Du, C. M., et al.: Calibration and performance of the STAR Muon Telescope Detector using cosmic rays. arXiv:1402.1078 [physics.ins-det], 2014.

169. Bieser, F., Crawford, H., Engelage, J., et al.: The STAR trigger. Nucl. Instruments Methods Phys. Res. Sect. A Accel. Spectrometers, Detect. Assoc. Equip., 499(2-3):766–777, March 2003.

170. Adler, C., Denisov, A., Garcia, E., et al.: The RHIC zero degree calorimeters. Nucl. Instruments Methods Phys. Res. Sect. A Accel. Spectrometers, Detect. Assoc. Equip., 470(3):488–499, September 2001.

171. Kiryluk, J.: Local polarimetry for proton beams with the STAR beam beam counters. In Spin physics. Polariz. electron sources polarimeters. Proceedings, 16th Int. Symp. SPIN 2004, Trieste, Italy, Oct. 10-16, 2004, Work. PESP 2004, Mainz, Ger. Oct. 7-9, 2004, pages 718–721, 2005.

172. Bland, L.: Star forward meson spectrometer. hena.lbl.gov/FMS/talks/LB_FMS_STAR_no_animation.ppt.

173. Braidot, E.: Suppression of Forward Pion Correlations in d+Au Interactions at STAR. In Proceedings, 45th Rencontres Moriond QCD High Energy Interact. La Thuile, Italy, March 13-20, 2010, 2010.

174. Nogach, L.: Measurements of Transverse Spin Effects with the Forward Pion Detector of STAR. In AIP Conf. Proc., volume 915, pages 543–546. AIP, December 2007.

175. Rose, A.: STAR integrated tracker. In Comput. High Energy Nucl. Phys. 2003 Conf. Proc., volume C0303241, page THLT004, 2003.

176. Jacobs, P., Irmscher, D., and Tas, C.: GSTAR : A Geant-based detector simulation chain for STAR STAR Note # 235 2 Event Input 3 Geometry Input Contents. https://drupal.star.bnl.gov/STAR/system/files/20091001_GSTAR_StarNote235.pdf, 1996. STAR Note.

177. GEANT – Detector Description and Simulation Tool. http://wwwasdoc.web.cern.ch/wwwasdoc/geant_html3/geantall.html. GEANT-3 Documentation.

178. Aggarwal, M. et al.: Azimuthal di-hadron correlations in d+Au and Au+Au collisions at $\sqrt{s_{NN}} = 200$ GeV from STAR. Phys. Rev. C, 82:024912, 2010.

179. Adams, J. et al.: Identified hadron spectra at large transverse momentum in p+p and d+Au collisions at s(NN)**(1/2) = 200-GeV. Phys. Lett. B, 637:161–169, 2006.

180. Adler, S. et al.: Jet structure of baryon excess in Au+Au collisions at $s_{NN} = 200$ GeV. Phys. Rev. C, 71(5):051902, May 2005.

181. Ulery, J. G.: Two- and three-particle jet correlations from STAR. Nucl. Phys. A, 774:581–584, 2006.

182. Aamodt, K. et al.: Particle-Yield Modification in Jetlike Azimuthal Dihadron Correlations in Pb-Pb Collisions at $\sqrt{s_{NN}} = 2.76$ TeV. Phys. Rev. Lett., 108(9):092301, March 2012.

183. Chatrchyan, S. et al.: Measurement of jet fragmentation into charged particles in pp and PbPb collisions at $\sqrt{s_{NN}} = 2.76$ TeV. JHEP, 10:87, October 2012.

184. ATLAS Collaboration: ATLAS-CONF-2012-115.

185. Agakishiev, G. et al.: Anomalous centrality evolution of two-particle angular correlations from Au-Au collisions at sqrt[s_{NN}]=62 and 200 GeV. Phys. Rev. C, 86(6):064902, December 2012.

186. Adams, J. et al.: Azimuthal anisotropy in Au+Au collisions at s(NN)**(1/2) = 200-GeV. Phys. Rev. C, 72:014904, 2005.

187. Adams, J. et al.: .

188. Trainor, T. A., Kettler, D. T., Prindle, D. J., and Ray, R.: Challenging claims of 'elliptic flow' by comparing azimuth quadrupole and jet-related angular correlations from Au-Au collisions at $\sqrt{s_{NN}} = 62$ and 200 GeV. 2013.

189. Agakishiev, G., Aggarwal, M. M., Ahammed, Z., et al.: Strangeness Enhancement in Cu+Cu and Au+Au Collisions at $\sqrt{s_N N} = 200$ GeV. Phys. Rev. Lett., 072301(February):1–6, February 2012.

190. Nattrass, C.: System, energy, and flavor dependence of jets through di-hadron correlations in heavy ion collisions. Dissertation, Yale University, 2009.

VITA

NAME: Kolja Kauder

EDUCATION: B. Sc., Mathematics and Applications, Heinrich Heine Universität Düsseldorf (HHU), Germany, 2007

M. S., High Energy Nuclear Physics, University of Illinois at Chicago (UIC), Chicago, IL, 2012

TEACHING: Undergraduate Mentor, HHU, 2000-2001

TA, Numerical Simulations with Special Applications in the Field of Optical Fibers and Non-linear Waves, HHU, 2002

TA, discussion and grading, Algebra-based Physics, UIC, 2008 and 2010

RESEARCH: Research Assistant, Institute for Theoretical Physics, HHU, 2001-2004

Research Assistant, High Energy Nuclear Physics, UIC, 2008-

COMMITTEES: Two appointments committees at HHU (Bioinformatics (2001) and Quantum Information (2004)).

Faculty Council Physics at HHU (ca. 2002)

Committee to develop and implement the Bachelor/Master system in Physics at HHU (ca. 2004)

RHIC User Executive Committee, RHIC, Brookhaven National Lab, Upton, NY, 2012-2013

MEMBERSHIPS: American Physical Society, STAR Collaboration.

CONTRIBUTED TALKS:

Jet Studies in STAR via Di-jet Triggered (2+1) Multi-hadron Correlations, Quark Matter, Knoxville, TN, 2009. (Nucl. Phys. A 830 (2009) 685C-688C)

Two-, Three-, and Jet-Hadron Correlations at STAR, Rencontres de Moriond, La Thuile, Italy, 2011. (moriond.in2p3.fr/QCD/2011/proceedings/kauder.pdf)

Leading Hadron PID Effects in Di-hadron Angular Correlations in STAR, Quark Matter, Annecy, France, 2011. (J.Phys. G 38 (2011) 124154)

What Can be Learned from Identifying Leading Hadrons of Jets in STAR?, Lake Louise Winter Institute, Lake Louise, Canada, 2013

TRAVEL AWARDS: Granted by Academia Sinica, Taipei, ROC, for Computing in High Energy and Nuclear Physics (CHEP) 2010

Granted by UIC Graduate Student Council for Rencontres de Moriond, La Thuile, Italy, 2011

SELECT PUBLICATIONS

Abdelwahab, N. M. et al.: Di-Hadron Correlations with Identified Leading Hadrons in 200 GeV Au+Au and d+Au Collisions at STAR, arXiv:1410.3524 [nucl-ex], submitted to PRL.

Adamczyk, L. et al.: Experimental studies of di-jets in Au+Au collisions using angular correlations with respect to back-to-back leading hadrons, in Phys. Rev. C 87, 044903, 2013.

Agakishiev, H. et al.: Experimental studies of di-jet survival and surface emission bias in Au+Au collisions via angular correlations with respect to back-to-back leading hadrons, in Phys. Rev. C 83, 061901, 2011.

(For a full list, see http://inspirehep.net/search?p=exactauthor%3AK.Kauder.1)